REFERENCE ONLY

2809444089

UNIVERSITY OF LONDON THESIS

Degree PhD Year 2007 Name of Author EFSTATHIOS STEFANIDES

COPYRIGHT

This is a thesis accepted for a Higher Degree of the University of London. It is an unpublished typescript and the copyright is held by the author. All persons consulting the thesis must read and abide by the Copyright Declaration below.

COPYRIGHT DECLARATION

I recognise that the copyright of the above-described thesis rests with the author and that no quotation from it or information derived from it may be published without the prior written consent of the author.

LOAN

Theses may not be lent to individuals, but the University Library may lend a copy to approved libraries within the United Kingdom, for consultation solely on the premises of those libraries. Application should be made to: The Theses Section, University of London Library, Senate House, Malet Street, London WC1E 7HU.

REPRODUCTION

University of London theses may not be reproduced without explicit written permission from the University of London Library. Enquiries should be addressed to the Theses Section of the Library. Regulations concerning reproduction vary according to the date of acceptance of the thesis and are listed below as guidelines.

A. Before 1962. Permission granted only upon the prior written consent of the author. (The University Library will provide addresses where possible).

B. 1962 - 1974. In many cases the author has agreed to permit copying upon completion of a Copyright Declaration.

C. 1975 - 1988. Most theses may be copied upon completion of a Copyright Declaration.

D. 1989 onwards. Most theses may be copied.

This thesis comes within category D.

☐ This copy has been deposited in the Library of UCL

☐ This copy has been deposited in the University of London Library, Senate House, Malet Street, London WC1E 7HU.

Bound By
Blissett Bookbin
020 8992 396
www.blissetts.c

Study of the WW scattering in the absence of light Higgs boson using the ATLAS Detector at LHC

Efstathios Stefanidis

University College London

Dissertation submitted to the Department of Physics and Astronomy
in accordance with the requirements of the University of London
for the degree of Doctor of Philosophy.

January, 2007

ProQuest LLC
789 East Eisenhower Parkway
P.O. Box 1346
Ann Arbor, MI 48106-1346

DECLARATION

I confirm that the work presented in this Thesis is my own. Where information has been derived from other sources, I confirm that this has been indicated in the document.

Efstathios Stefanidis

The places in the Universe I liked the most,

were the places I discovered myself.

To the memory of my dear and kind friend John Beacon, who left us very early and unexpectedly, taking with him the promise that we would return to the good, old times of fun when this project was completed.

Abstract

The Thesis investigates the possible case that the Electroweak Symmetry Breaking is not due to a light, weakly interacting Higgs boson, but instead the Symmetry is broken by strongly interacting heavy resonances. In that case, the formalism of the Electroweak Chiral Lagrangian can be used as a model-independent way to construct a low-energy effective theory for the electroweak interactions and using the Padé unitarisation protocol, certain resonances can be predicted. The scattering of longitudinally polarized W bosons, one of which decays leptonically and the other hadronically, is used as a channel to probe the mechanism of the Electroweak Symmetry Breaking in the mass range of 600 GeV up to 2.4 TeV and for different resonance scenarios, including the case that there is no resonance in the spectrum. The reconstruction of the vector bosons is described and it is demonstrated that, by exploiting key features of the hadronic environment, the contribution from the background processes can be reduced in such a way that the ATLAS detector will be able to see interesting WW scattering events within the above mass range with 30 fb^{-1} of data and it will be also possible to distinguish among the different resonance scenarios. A key study of the present research is the measurement of the WW scattering cross-section and it has been calculated that a significant measurement will be achieved, for the most pessimistic scenario, with 80 fb^{-1} of data.

Regarding the performance of the ATLAS detector, the Thesis focuses on the Level-2 Trigger for selecting interesting physics events. After a short introduction to the Trigger system of the detector, the concept of the Region of Interest is explained and a method for reducing its geometrical size is presented. The method is based on the information from the Electromagnetic Calorimeter and it will be demonstrated that the reduced size can improve the performance of the Level-2 Trigger in terms of execution time (58% faster) but also for track reconstruction (6% more efficient) in the Inner Detector, especially during the high luminosity phase of the LHC.

Acknowledgements

In most of the prefaces, the authors use to refer back to the way that they got inspired to study Physics. The normal story is that one of their parents or their relatives or themselves looking at the stars in the night or even a nice science fiction book triggered their imagination and their love for the science. Those people I know became very successful and wanted scientists.

That was not the case for me. And here is the first time to confess that until the age of eleven I couldn't make even a simple adding or subtraction. Not to mention multiplication or division. And it was that young teacher of my primary school at that tiny village who sat next to me and taught me maths and made me feel comfortable with the numerical problems. I can still remember him saying to me: "Rarely will you come across with problems that don't have a solution". Since then, I believed in his words and my interest in science began. Not by any other reason, but because Maths and Physics became my two most challenging friends, which in fact taught me myself and always extended my limits.

That child grew up and has finally managed to do his research degree in High Energy Physics. And I wouldn't be able to reach none of my goals, if I didn't have my parents and my family. They worked hard to finance my education, my studies, my dreams. And even during the harsh financial difficulties and when their tiredness started to draw their faces, their love and support were endless and most importantly, without waiting a paying-off. I don't know if I could ever be able to express my gratitude, but I feel the urge to write my thanks in the language they can read and understand:

Μητέρα μου ϰαι Πατέρα μου, σας ευχαριστώ που τόσα χρόνια με στηρίξατε ϰαι με βοηϑήσατε να εϰπληρώσω τα όνειρά μου.

I feel really lucky that I had the chance to carry out my research with the High Energy Physics Group at UCL, which welcame me, integrated me and gave me a nice environment to work.

Dr. N. Konstantinidis has been an excellent supervisor and teacher during the last three years, but also very understanding towards my concerns, worries and problems. And for that I thank him.

My work on the main physics subject couldn't have been more interesting, if it wasn't for Prof. J. Butterworth, who introduced me to it and successfully guided this part of my research. I got knowledge and research skills of high standards and I thank him for working with me.

I also need to thank Dr. S. Dean and Dr. P. Sherwood for the help they provided me to face the difficulties related to the complicated software environment and finally develop my analysis codes.

I appreciate the help I had from Dr. E.Ozcan for making my project even better. He gave me a different way of thinking, approaching and evaluating the problems. I will really miss the top quality physics discussions we had and the excellent work as a team.

I have to acknowledge the support I got from the Group's computing staff and the Department's administrative staff. Both did their best to solve technical and beaurocratic issues, giving me more time to invest on my project.

Finally, my research was more comfortable because of the financial support I had from the Group, the Department of Physics and Astronomy and the Central Laboratory of the Research Councils. The "Alexander S. Onassis" public benefit foundation honored me with a generous scholarship, which was a great relief for me and my family. I thank all.

Efstathios Stefanidis

Contents

I The Detector 6

Part I

The Detector

CHAPTER 1

The Large Hadron Collider and the ATLAS Detector

This chapter is an introduction to the Large Hadron Collider (LHC) machine. It starts with the physics motivation for building this machine and then describes the specific features of it, emphasizing the challenges, since LHC will provide the highest center of mass energy ever achieved. Next, the ATLAS detector will be described in detail. Due to the challenges arising from the harsh LHC environment, ATLAS has to employ fast, accurate and robust systems, the features of which will be discussed in details.

1.1 The LHC

1.1.1 Motivation for the Large Hadron Collider

The physics motivation provides the guidance for the construction specifications of the LHC machine together with the individual detectors themselves. At the new frontier of the High Energy Physics, the areas that we (primarily) aim to study with the Large Hadron Collider can be summarized as follows:

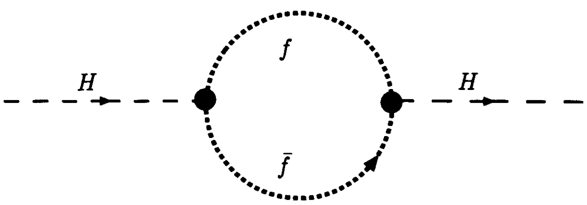

Figure 1.1: One-loop fermionic correction to the Higgs mass. The loop of the top quark is the one which contributes the most.

- **Explore the mechanism of the electroweak symmetry breaking:** Although the Standard Model (SM) of the electroweak interactions provides a successful description of particle physics phenomenology (its predictions have been verified at the level of 0.1% or better by the experiments (mainly) at LEP and Tevatron - see [1, 2, 3]), the mechanism of the electroweak symmetry breaking has not yet been tested. The SM and the electroweak symmetry breaking will be discussed in details in the second part of the thesis, but at the moment it is sufficient to mention that, within the SM, the electroweak symmetry breaking is explained by the Higgs mechanism, introducing a scalar particle, the Higgs boson. The mass of the particle is not predicted by the theory. Direct searches in the previous experiments (mainly at LEP2) set a low mass limit of 114.4 GeV at 95 % confidence level [4]. This limit can be indirectly constrained from global fits to high precision electroweak data, which suggest a mass of $m_H = 89^{+42}_{-30}$ GeV [5]. If we also assume that there is not physics beyond the SM up to a large scale Λ, then, on theoretical grounds, the upper limit on the Higgs mass can be set to ~1 TeV [6]. Therefore, there is a need for a machine that can probe the whole mass range and LHC has been designed for that.

- **Physics Beyond the Standard Model:** There are several arguments which indicate that the SM is not the final and complete theory. One of these, probably the strongest, is the so-called **hierarchy problem:** if the Higgs particle exists, then fermionic radiative corrections to its mass will be described (at one-loop) by the diagram in Figure 1.1.

Then, the (renormalized) mass of the Higgs particle would be:

$$M^2_{H,Ren} = M^2_{H,0} + \delta M^2_H \lessapprox (1\ \text{TeV})^2 \tag{1.1}$$

where $M_{H,0}$ is the bare Higgs mass that enters at the SM Lagrangian and the upper limit comes from theoretical reasons mentioned before. But the mass correction δM_H depends quadratically on the cut-off Λ for the momentum in loop:

$$\delta M^2_H \sim \int_0^\Lambda \frac{d^4k}{k^2} \sim \Lambda^2 \tag{1.2}$$

Finally, if we assume that there is not new physics beyond the Planck scale, then $\Lambda \simeq M_{Planck} \simeq 10^{19}$ GeV, which leads to:

$$M^2_{H,Ren} \ggg (1\ \text{TeV})^2 \tag{1.3}$$

Since this value does not agree with Equation 1.1, we start to believe that possible new physics must demonstrate itself at the TeV scale. More general theories (like SUSY - see [7]) give a solution to this problem by introducing new particles and by suggesting a new phenomenology, both of which are feasible to explore with the LHC.

- **Electroweak precision measurements:** Because of the high energy and the luminosity achieved, the LHC will be a factory of W and Z bosons as well as of top and bottom quarks[1]. The large statistics of the events will make it possible, despite the harsh hadronic environment, to improve the accuracy of the current values for many electroweak parameters. This goal becomes more important and gets connected to the previous one just by bringing into mind that any observed deviation from the predicted values for SM observables is a signal for new physics.

---

[1] It is estimated that the LHC, during the first year of operation, will give 10^8 $W \rightarrow e\nu$, 10^7 $Z \rightarrow e\nu$, 10^7 $t\bar{t}$, and 10^{12} $b\bar{b}$ events.

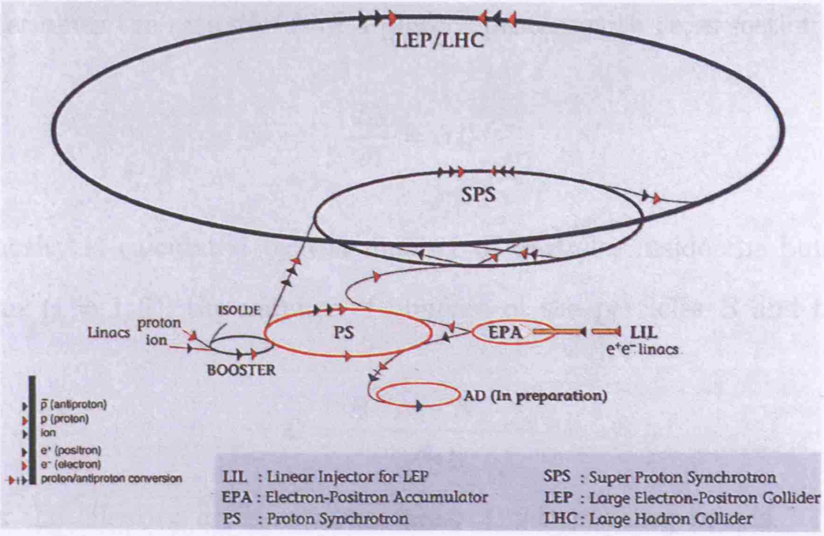

Figure 1.2: Diagram of the CERN accelerator complex.

1.1.2 Construction of the Large Hadron Collider

The Large Hadron Collider [8] is currently being constructed in the already existing LEP tunnel of (approximately) 27 km circumference. The machine will provide mainly proton-proton collisions, but it is also scheduled to provide heavy ion collisions as well.

The colliding proton beams will acquire energy of 7 TeV each, thus providing 14 TeV centre of mass energy (7 times bigger than the centre of mass energy provided by Tevatron, at Fermilab). Before the protons are injected into the LHC, they will be pre-accelerated in different facilities acquiring in each step more and more energy. The whole injector chain is given in Figure 1.2. Protons will be produced and initially accelerated by the proton linear accelerator (linac) to the energy of 50 MeV. At the next stage, they will be boosted to 1.4 GeV before they are injected in the Proton Synchrotron (PS), where they will reach the energy of 25 GeV, having a linear velocity almost 87% of the speed of light (0.87c). Finally, they will reach the energy of 450 GeV by accelerating inside the Super Proton Synchrotron (SPS). After this stage, the LHC will provide them with the final energy of 7 TeV each, with a relativistic speed of 0.9999997c.

One of the most important parameters of an accelerator is the **luminosity** that it delivers. The luminosity plays a crucial role for the physics programme of the LHC, because it determines the rate dN/dt of a physics process with cross-section σ:

$$\frac{dN}{dt} = \sigma\mathcal{L} \tag{1.4}$$

The luminosity is calculated by the number of particles inside the bunch N_i of the colliding beams ($i = 1,2$), the number of bunches of the particles B and the revolution frequency f_o:

$$\mathcal{L} = \frac{B \cdot N_1 \cdot N_2 \cdot f_o}{A_{eff}} \tag{1.5}$$

where A_{eff} is the effective cross sectional area of the colliding beams. There are two phases that are foreseen for the LHC: the first years the machine is planned to run at **low luminosity** with $\mathcal{L} = 2 \times 10^{33}$ cm^{-2}sec^{-1} and there will be a gradual upgrade to the design luminosity (**high luminosity**) of $\mathcal{L} = 10^{34}$ cm^{-2}sec^{-1}. Most commonly, the **integrated luminosity L** is used, which is the integral of the instantaneous luminosity over time:

$$L = \int \mathcal{L} dt \tag{1.6}$$

For example, integrated luminosity of $L = 10\ fb^{-1}$ corresponds to 1 year running at low luminosity, where $L = 100\ fb^{-1}$ corresponds to 1 year of high luminosity.

The two bunches of protons will collide every 25 nsec. Taking into account the cross section for the inelastic proton-proton collision ($\sigma_{pp}^{inel} = 60$ mb), we expect to have $\sim 10^{11}$ proton interactions per second, which is an unprecedent collision rate [2].

In order to bend the accelerated protons, super-conducting magnets will be used to provide a magnetic field of 8.39 T. It is one of the LHC characteristics the fact that, due to lack of space in the tunnel to accomodate two separate magnets, there will be a single, twin-aperture magnet with two coils accelerating the beams in opposite directions. The magnet coils are made of copper-clad niobium-titanium cables and in order to achieve the super-conducting properties, these should be cooled to a temperature of 1.9 K.

---

[2] The total proton-proton cross section at 7 TeV is approximately 110 mb. This comes in contribution from the inelastic (60 mb), single diffractive (12 mb) and the elastic (40 mb) collisions.

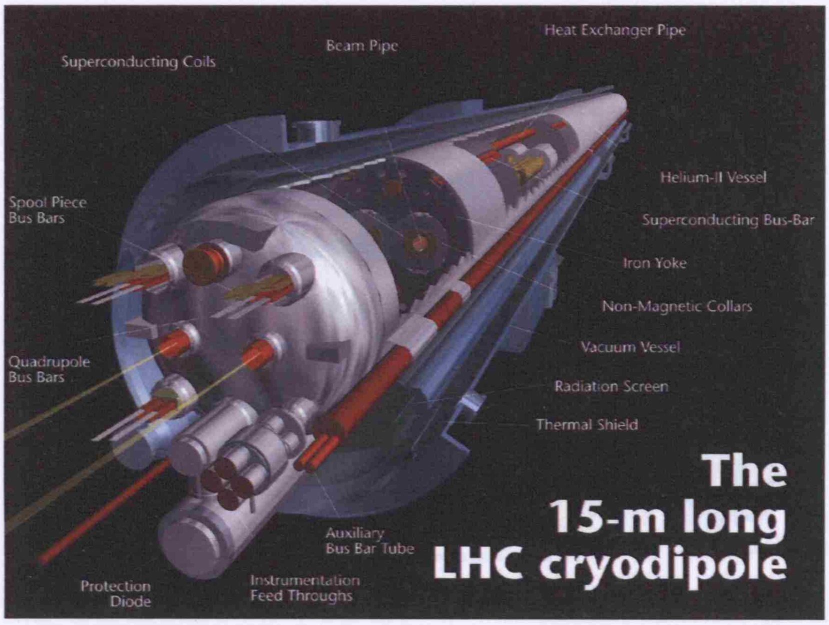

Figure 1.3: The LHC dipole magnet and cryostats setup. The two beams will lie next to each other under the same dipole magnet.

The cooling is done by a huge cryogenic system, common to both proton beams. It uses super-fluid helium, which has efficient heat transfer properties, allowing kilowatts of refrigeration to be transported over more than a kilometer with a temperature drop of less than 0.1 K.

The final setup of the LHC is illustrated in Figure 1.3.

1.2 The ATLAS Detector

The general overview of the ATLAS detector is given in Figure 1.4. It is a multi purpose detector and has the typical structure of any collider physics detector, built with a 4π coverage.

From the innermost towards the outermost layer, it consists of three parts:

- **Inner Detector** [9]: It is inside the solenoid magnetic field [10] of 2 T and it is used to detect charged particles and also to identify secondary vertices. In order to perform also pattern recognition, the Inner Detector employs sub-detectors of high

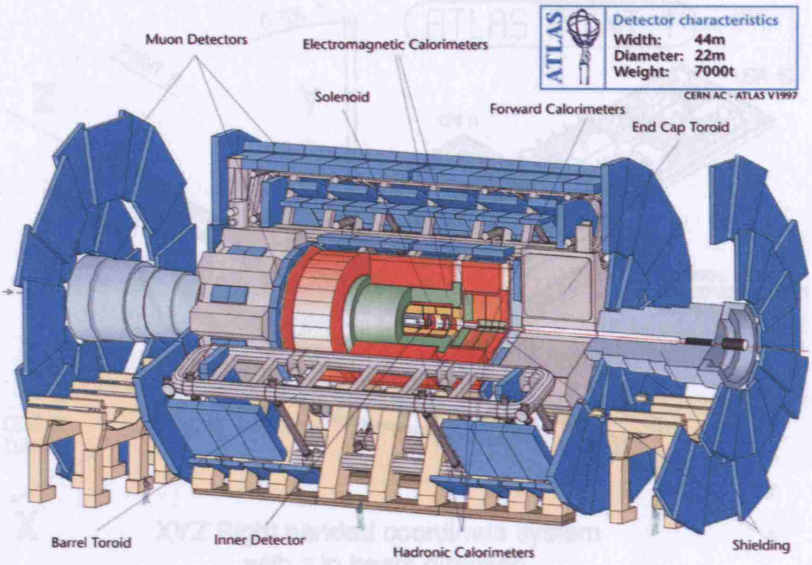

Figure 1.4: General overview of the ATLAS detector.

precision.

- **Calorimeter [11, 12]**:It is used to measure the energy and the position of the electrons and photons (EM Calorimeter) and of the hadrons and jets (Tile Calorimeter). From the energy deposited at the Calorimeter and due to the fact that the protons have negligible transverse component of momentum, one can calculate the missing transverse energy (E_T^{miss}), which accounts for the energy of the particles that haven't interacted with any part of the detector.

- **Muon Spectrometer [13]**: It is used to identify the muons. For a precise measurement of their momentum, the muon spectrometer is located outside the superconducting air-core toroid magnets [14, 15].

Figure 1.5 shows the general coordinate system used for the detector. It is a right-handed system with the x-axis pointing towards the center of the LHC ring. The beam axis defines the z-axis, while the y-axis points upwards. The azimuthal angle ϕ is defined in the XY plane, with $\phi = 0$ being the positive x-axis and it runs clock-wise. The polar angle θ is defined with respect to the beam pipe, with $\theta = 0$ being the positive z axis.

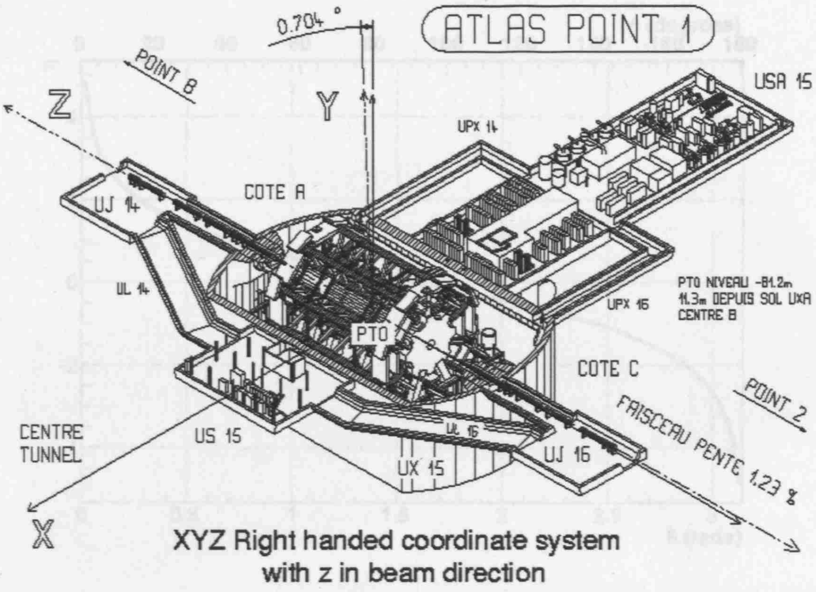

Figure 1.5: The coordinate system of the ATLAS detector.

For highly relativistic particles ($P >> m$), the term of **pseudorapidity** η is used, instead of the polar angle θ. The reason for doing so is the property that differences in pseudorapidity are invariant under boosts along the beam axis [16] and this is very helpful, since the P_z component of the interacting partons is not known, and therefore we can't actually use the rapidity [3] as a variable. The pseudorapidity is related to the polar angle through the equation:

$$\eta \equiv -\ln\left[\tan\left(\frac{\theta}{2}\right)\right] \tag{1.7}$$

Equation 1.7 is plotted in Figure 1.6. Particles which are traveling close to the beam pipe ($\theta \to 0$) will correspond to high values of pseudorapidity ($\eta \to \pm\infty$), whereas particles emitted vertical to the beam pipe ($\theta = \frac{\pi}{2}$) will correspond to zero pseudorapidity ($\eta = 0$).

The detailed description of the characteristics of the detector's parts may be found in the individual Technical Design Reports and beyond the scope of this Thesis. However, it is essential to give a basic information about the construction of the different parts, their principle of detection and the accuracy they are expected to achieve.

---

[3] The rapidity is defined by $y = \frac{1}{2}\ln\left(\frac{E+P_z}{E-P_z}\right)$.

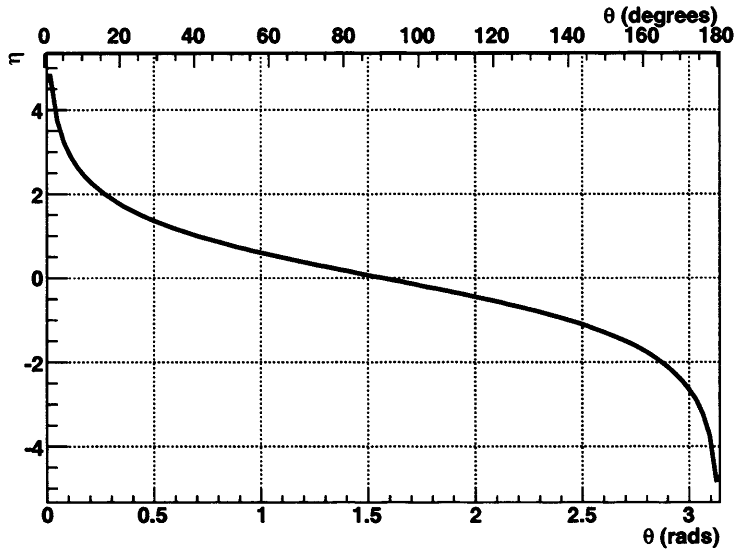

Figure 1.6: The relation between the pseudorapidity η and the polar angle θ (Equation 1.7).

1.2.1 The Inner Detector

The layout of the Inner Detector (ID) is given in Figure 1.7, while Figure 1.8 shows the transverse projection. It is 7 m long with 1.15 m outer radius, located inside the solenoidal magnetic field. Mechanically, it consists of the barrel part, which extends ±80 cm and the two endcap parts covering the rest of the cylindrical cavity over the full pseudorapidity range. The purpose of the ID is to achieve high-precision measurement of the momentum and trajectory of charged particles.

Given the harsh environment of the LHC, sub-detectors with fine granularity must be used. To fulfill these requirements, high-precision detectors are used close to the beam pipe. The total number of the precision detector elements is limited not only by their high cost, but also by the amount of material that they will introduce. Based on these criteria, the optimum layout for the barrel part consists of three pixel layers and eight silicon micro-strip detectors (semi-conductor tracker) arranged in four layers. For the endcap, there are five discs of pixel detectors, whereas the semi-conductor tracker is formed by rings of wedge-shaped modules.

Furthermore, to improve the momentum resolution, the **Transition Radiation Tracker**

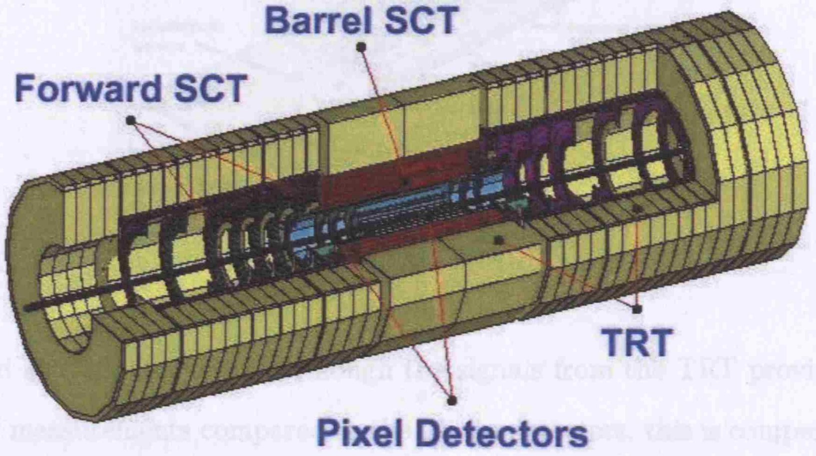

Figure 1.7: 3-D prospect of the Inner Detector.

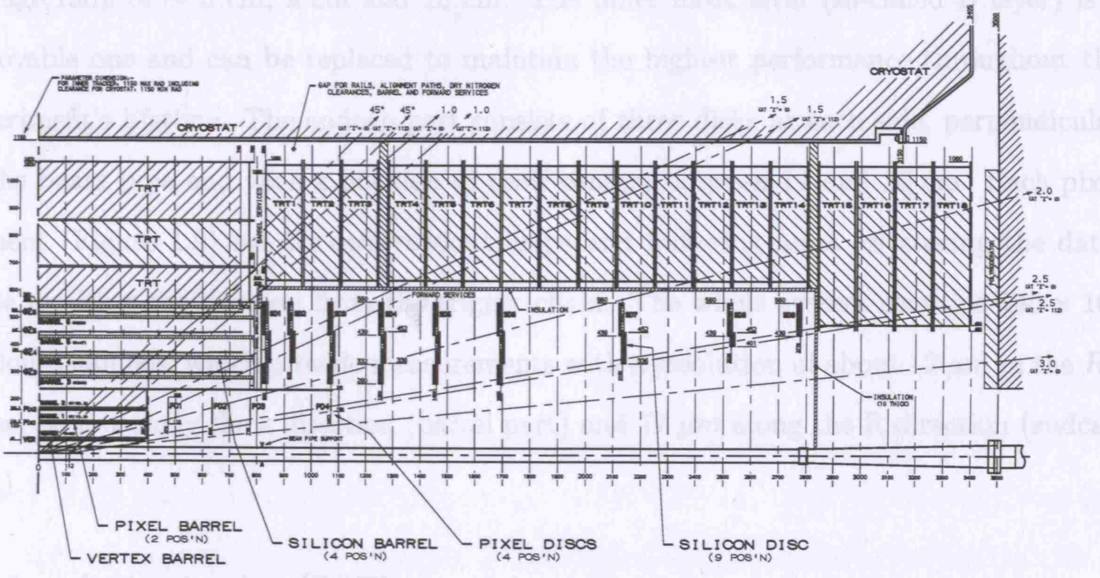

Figure 1.8: Projection of the Inner Detector on the transverse plane. The length units are expressed in mm.

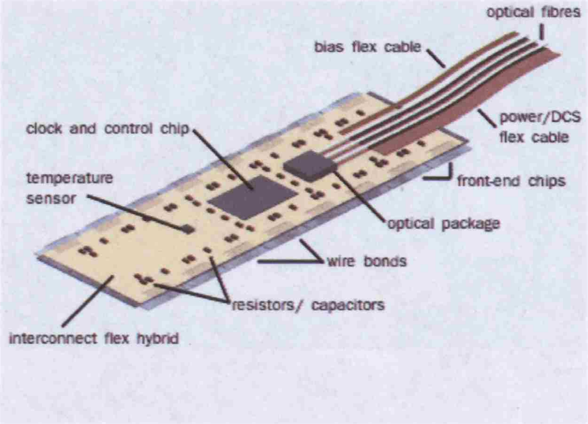

Figure 1.9: A pixel module.

(TRT) is used at the outer radii. Although the signals from the TRT provide a less precise trajectory measurements compared to the silicon detectors, this is compensated by the large number of measurements, obtained using much less and much cheaper material.

Pixel Detector

The purpose of the Pixel Detector is to provide a set of high precision measurements close to the interaction point. The barrel part consists of three concentric cylindrical layers at average radii of ~ 5 cm, 9 cm and 13 cm. The inner most layer (so-called B layer) is a removable one and can be replaced to maintain the highest performance throughout the experiment's lifetime. The endcap part consists of three disks at each side, perpendicular to the beam pipe and with z position of their centers between 11 and 20 cm. Each pixel element (Figure 1.9) has its own readout chips and buffering units for storing the data, while awaiting the decision from the trigger chain. The whole system contains 140×10^6 readout channels, which provide measurements with a resolution of about 12 μm in the $R\phi$ plane, 66 μm along the z direction (barrel part) and 77 μm along the R direction (endcap part).

Semiconductor tracker (SCT)

The SCT detector contributes to the measurement of both the momentum and the position of charged particles. Due to its high granularity, a very good pattern recognition is feasible.

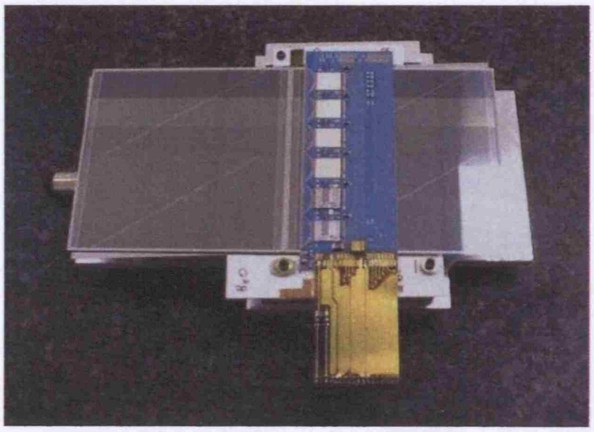

Figure 1.10: An SCT module.

Each silicon detector has an area of $6.36 \times 6.40\ cm^2$ consisting of 768 readout strips of 80 μm pitch between them. Two such detectors are wire-bonded together to form 12.8 cm long strips. Two such detector pairs are then glued together back-to-back to form a module (Figure 1.10). The two layers of the module are rotated by 40 mrad stereo angle with respect to each other, thus providing the z-coordinate. The barrel modules of the SCT are arranged again in concentric cylinders of radii 30.0, 37.3, 44.7 and 52.0 cm. The endcap modules are mounted up to three rings onto nine wheels starting at z $\sim$ 81 cm up to z $\sim$ 280 cm. There are 6.2×10^6 readout channels and the designed spatial resolution is 16 μm in the $R\phi$ plane and 580 μm for the second position coordinate. Two different tracks are detected as one only if they are separated by less than $\sim$ 200 μm.

Transition Radiation Tracker (TRT)

The edge of a TRT barrel module is shown in Figure 1.11. The main detector element of a TRT is a straw of 4 mm diameter and a maximum length of 144 cm in the barrel. The straw is filled with a gas mixture ($Xe : CO_2 : CF_4 = 70 : 20 : 10$). In the centre of the straw, there is a gold-plated W-Re wire of 30 μm diameter, which measures the drift time of the ionizing particles through the gas. The barrel part consists of about ~50,000 axial straws, arranged in 3 cylinders. Each straw is divided into two at the center and their readouts are at both ends. The endcap part consists of ~320,000 radial straws arranged

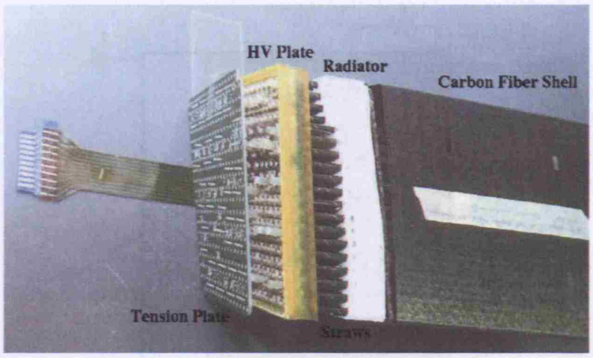

Figure 1.11: The end of one of the TRT barrel modules.

in 18 wheels on each side, with the readout at the outer radius. A track hits, in average, 36 straws and the designed resolution in the position of the hit, for both parts, is 170 μm.

Apart from very good pattern recognition, the TRT is used also for particle identification. This is due to the fact that between the straws there is a material (polypropylene foils), so that charged, ultra-relativistic particles emit radiation (photons) when they cross the boundary between materials with different dielectric constant. Light particles (like electrons) start producing transition radiation at low momentum (approximately 1 GeV) compared to heavy charged particles (like pions), which emit transition radiation at high momenta (approximately 100 GeV) [17]. Therefore, by tuning the readout threshold of each straw, one can identify and select particles.

1.2.2 The Calorimeters

The purpose of a Calorimeter is to measure the energy of the particles that travel through it. Schematically, the principle of a **sampling** calorimeter, such as the ATLAS ones, is given in Figure 1.12. By letting the particles interact with a material of high density (absorber), they deposit all of their energy inside the detection volume. Between the absorber plates, there is an active material (liquid argon (LAr) in the case of the ATLAS electro-magnetic calorimeter), which gets ionized by the charged particles produced in the absorber. Finally, under an applied electric field, the ions drift towards the electrodes, which give a signal proportional to the energy of the primary particle.

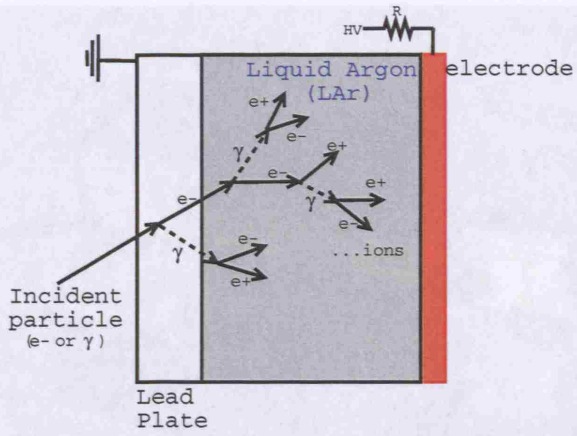

Figure 1.12: The detection principle of a sampling calorimeter. The materials given are for the ATLAS electromagnetic calorimeter.

The ATLAS detector has both an **Electromagnetic Calorimeter**, for electromagnetically interacting particles (electrons, positrons and photons), and a **Hadronic Calorimeter** for hadrons (like pions and kaons). The overall layout of the ATLAS Calorimeters is given by Figure 1.13. The electromagnetic calorimeter (barrel and endcap part) covers the pseudorapidity range of $|\eta| < 3.2$, with a gap in the range $1.3 < |\eta| < 1.5$. The hadronic barrel and 'extend barrel' part covers $|\eta| < 1.7$ and the hadronic endcap part $1.5 < |\eta| < 3.2$. For the whole calorimeter to be hermetic (so as to achieve a good measurement of the missing energy of the events and the detection of very forward jets), there is a fourth part, the very forward, which covers the range of $3.1 < |\eta| < 4.9$.

The Electromagnetic (EM) Calorimeter

The EM Calorimeter has an accordion shape, as shown in Figure 1.14. The absorber plates are made of lead and the electrodes, also accordion-shaped, are made of kapton. The modules are placed in the barrel and in the endcap in such way, that the absorber plates and the electrodes are perpendicular to the direction of the incident particle.

The barrel part consists of two identical halves, which are separated by a small gap (6 mm) at $z = 0$. The deposited energy is sampled by 3 samplings. The first sampling has a granularity of $\Delta\eta \times \Delta\phi = 0.003 \times 0.1$. [4]

---

[4] The pseudorapidity η is a dimensionless quantity and the angle ϕ is measured in rads.

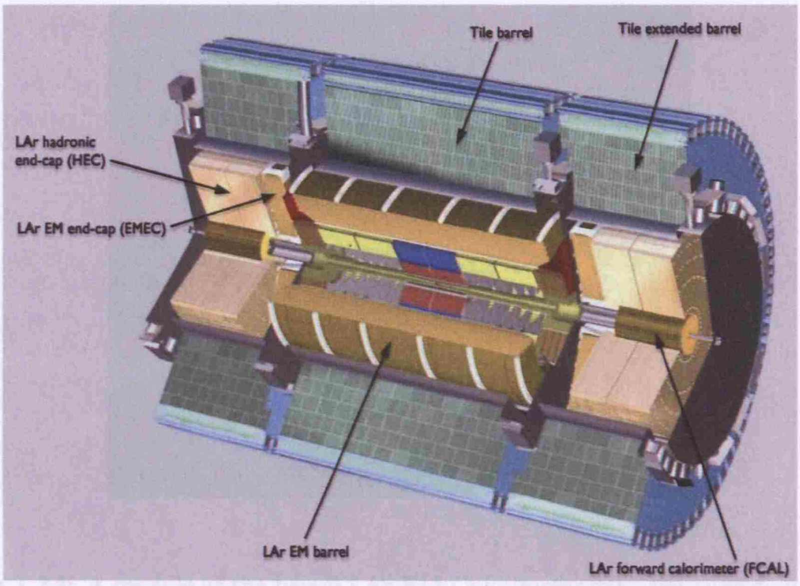

Figure 1.13: The Calorimetry of the ATLAS Detector.

The narrow strips in the η direction enhance the particle identification, since for instance, a very good γ/π^o and e/π separation can be achieved by looking at the shower profiles developed in the first sampling (for an example, see [18]). This high granularity helps also in identifying photons and electrons which originated from secondary decays, rather than the primary interaction point. The second sampling is segmented into square towers with dimensions $\Delta\eta\times\Delta\phi = 0.025\times0.025$ and the bulk of the EM energy is deposited here. This is why the last sampling has a coarse granularity of $\Delta\eta \times \Delta\phi = 0.05 \times 0.025$.

The endcap part is divided into two coaxial wheels (Figure 1.15): the inner wheel which covers the region $2.5 < |\eta| < 3.2$ and the outer wheel which covers the region $1.36 < |\eta| < 2.5$. Even though the energy is also sampled by three compartments, the difference between the two wheels is the granularity, which, for the inner wheel, is coarser. For example, the first sampling in the outer wheel has a granularity of $\Delta\eta\times\Delta\phi = 0.025\times0.1$ (approximately, since there is a strong η dependence), whereas in the inner wheel it is segmented into $\Delta\eta \times \Delta\phi = 0.1 \times 0.1$. The second sampling has granularity of $\Delta\eta \times \Delta\phi = 0.025 \times 0.025$ in the outer wheel and $\Delta\eta \times \Delta\phi = 0.1 \times 0.1$ in the inner. Finally, the third sampling is equally segmented for both wheels ($\Delta\eta \times \Delta\phi = 0.05 \times 0.025$).

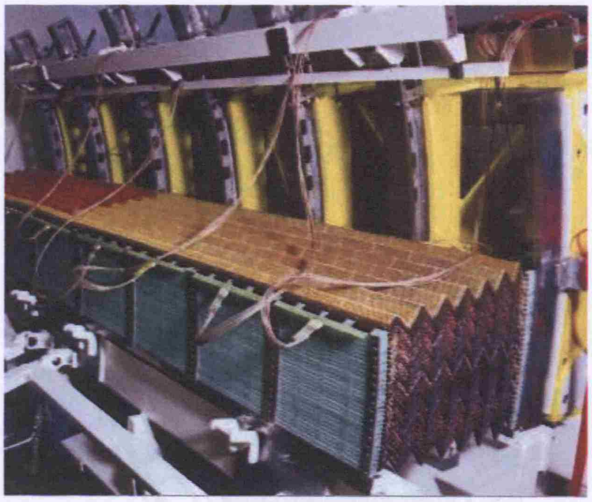

Figure 1.14: A module of the barrel LAr EM Calorimeter with the accordion shape.

A component of the electromagnetic calorimeter is the **presampler**. This is located in front of the LAr part, in the space with $|\eta| < 1.8$ and it has granularity of $\Delta\eta \times \Delta\phi = 0.025 \times 0.1$. It is installed immediately after the cryostat wall and its purpose is to correct for the energy loss in the material in front of the calorimeter (inner detector, coil and cryostats) on an event-by-event basis. The principle is that particles, which shower in the material in front of the presampler, lead to an increased particle multiplicity, which is measured by the presampler. It is then the combined information from the presampler and the calorimeter which allows the event-by-event measurement of the energy loss in front of the calorimeter.

Figure 1.16 shows the energy deposited by an electron into the four compartments of the EM Calorimeter. The blue lines are drawn to demonstrate the dimensions of each cell at each sampling and the energy measured in each cell is propotional to the yellow area inside this cell. One can see that the electron deposits the bulk of its energy at the first and second samplings, without energy spread in the last compartment.

The Hadronic Calorimeter (HCAL)

The HCAL has to be able to contain in its volume the hadronic showers of all the particles that have passed through the EM calorimeter (apart from the muons) and stop as many

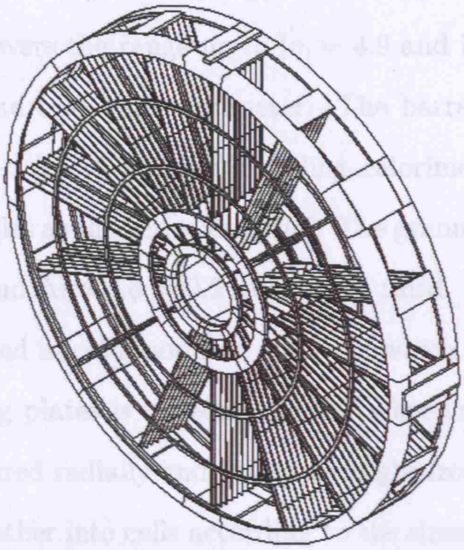

Figure 1.15: The endcap part of the EM Calorimeter.

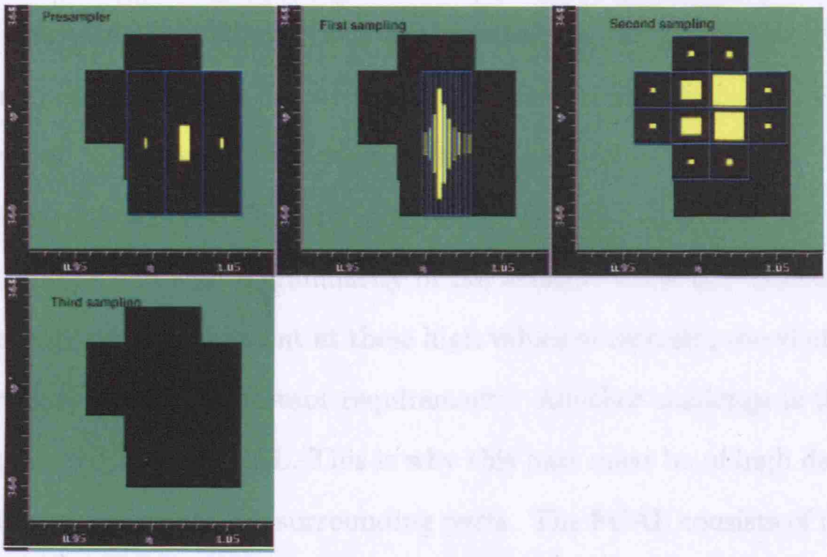

Figure 1.16: Energy deposition of an electron as it passes through the EM sampling Calorimeter. The figure has been created using the ATLANTIS event display [19].

as possible of them from passing to the muon spectrometer. It is also important to ensure that it covers a large range in η, providing a good measurement of the E_T^{miss}. Therefore, the hadronic calorimeter covers the range up to $|\eta| = 4.9$ and it consists of three parts.

The first part is the hadronic tile calorimeter. The barrel part ($|\eta| < 1.0$) and the extended barrel part ($0.8 < |\eta| < 1.7$) are sampling calorimeters which use iron as the absorber and scintillating tiles as the active material. The granularity is $\Delta\eta \times \Delta\phi = 0.1 \times 0.1$ in the first two samplings and $\Delta\eta \times \Delta\phi = 0.2 \times 0.1$ in the third. Azimuthally, the barrel and the extended part are divided into 64 modules, a view of which is given in Figure 1.17. The signal from the scintillating plates is collected by the Wavelength Shifting (WLS) fibres. The WLS fibres are configured radially and collect the light from both of the plates' edges. The fibres are grouped together into cells according to the sizes mentioned before and they are driven onto a single photo-multiplier.

The second part is the hadronic LAr calorimeter, which covers the range $1.5 < |\eta| < 3.2$ with granularity of $\Delta\eta \times \Delta\phi = 0.1 \times 0.1$ up to $|\eta| = 2.5$ and $\Delta\eta \times \Delta\phi = 0.2 \times 0.2$ for the rest. It consists of 32 triangular shaped modules (Figure 1.18-a) arranged in two independent wheels (Figure 1.18-b). Each module is made of several copper plates which are 25 mm thick at the inner wheel and 50 mm thick at the outer one. In both wheels, the plates are positioned 8 mm apart in a bath of LAr that is subjected to high voltage, induced by three parallel electrodes, the middle of which provides the readout.

The third part is the LAr forward calorimeter (FCAL). It covers the very forward region for $3.1 < |\eta| < 4.9$ with a granularity of $\Delta\eta \times \Delta\phi = 0.2 \times 0.2$. Due to the extreme particle and energy flux environment at these high values of rapidity, speed of response and radiation hardness are very important requirements. Another challenge is the limitations of the space provided for the FCAL. This is why this part must be of high density in order to ensure no energy leakage to the surrounding parts. The FCAL consists of three sections, the first being made of copper, the other two of tungsten. In each section the calorimeter consists of a metal matrix (Figure 1.19-a) in which hollow tubes of 5 mm inner diameter are embedded. Metal rods of 4.5 mm diameter (Figure 1.19-b) are centered inside the tubes

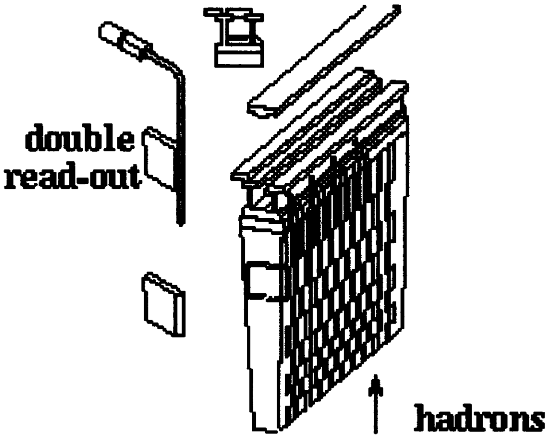

Figure 1.17: A module of the barrel tile HCAL.

and the LAr fills the small gaps between rod and tube wall. A few hundred volts between rod and tube produces the electric field to make electrons drift in the argon-filled gap.

Resolution of the Calorimeter

The energy resolution of a sampling calorimeter is given by the equation [20]:

$$\frac{\sigma(E)}{E} = \frac{a}{\sqrt{E}} \oplus \frac{b}{E} \oplus c \tag{1.8}$$

where E is expressed in GeV. The first term is the sampling term coming from the sampling fluctuations. The second term is the noise term which is associated with the electronic noise and the noise from the pile-up events and dominates at low energies (below 20 GeV). The third term is the constant term which is due to the mechanical imperfections, calibration etc. and dominates the resolution at high energies (above 40 GeV). To achieve the physics requirements, the designed resolution is expected to be [11]:

$$\frac{\sigma(E)}{E} = \frac{10\%}{\sqrt{E}} \oplus \frac{0.3\,\text{GeV}}{E} \oplus 0.7\% \tag{1.9}$$

The above parameters depend on η, but all the regions (with the crack region being the only exception) give values close to the designed ones. The behavior of the Calorimeter has

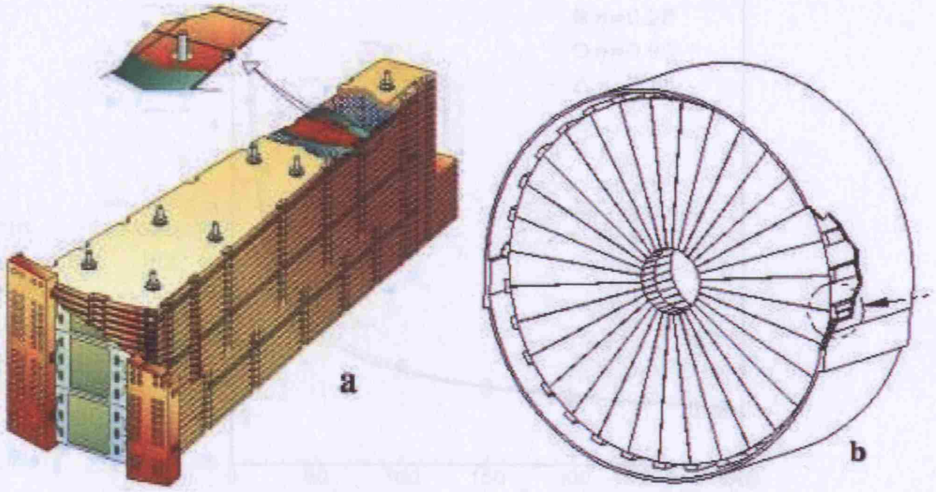

Figure 1.18: A module (a) and a wheel (b) of the endcap HCAL.

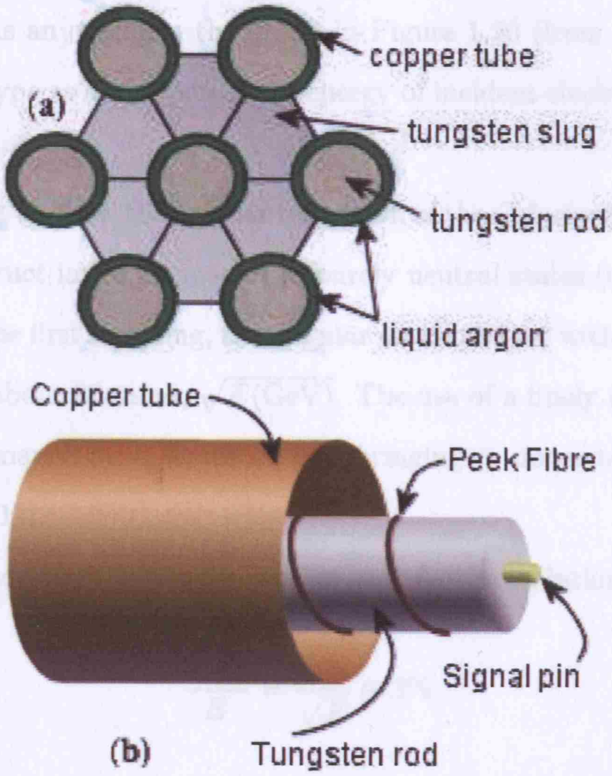

Figure 1.19: A matrix (a) and a rod (b) of the FCAL.

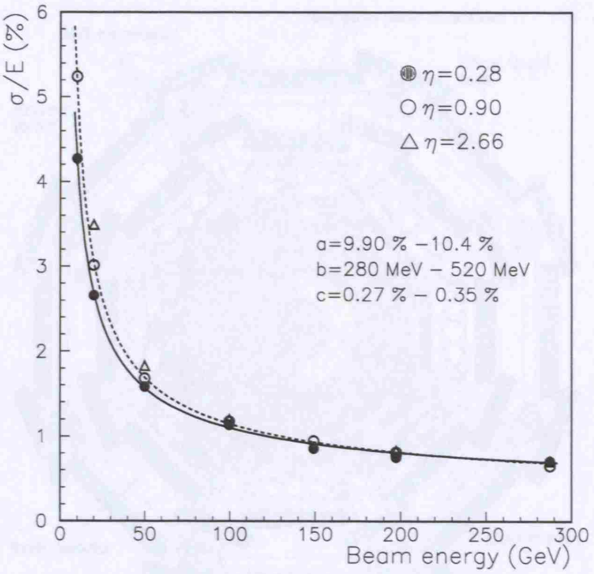

Figure 1.20: Fractional energy resolution as a function of the beam energy for electrons incident at $\eta = 0.28$ (closed circles), $\eta = 0.9$ (open circles) and $\eta = 2.66$ (triangles).

been extensively studied with test-beams and the response is in good agreement with the predicted one [21]. As an example, the graph in Figure 1.20 (from [22]) gives the energy resolution of a prototype as a function of the energy of incident electrons, at three different η positions.

It is also important to know the angular resolution of the Calorimeter since this is needed to accurately reconstruct invariant masses of purely neutral states (e.g. $H \to \gamma\gamma$). Due to the narrow strips in the first sampling, the angular measurement with the calorimeter alone gives a resolution of about 80 mrad$/\sqrt{E(\mathrm{GeV})}$. The use of a finely segmented presampler improves this performance by a factor of 2.5, bringing it down to the desired level of 40 mrad$/\sqrt{E(\mathrm{GeV})}$ [11].

Finally, for the hadronic calorimeter, the jet and E_T^{miss} resolution are:

$$\frac{\sigma(E)}{E} = \frac{50\%}{\sqrt{E}} \oplus 3\% \tag{1.10}$$

for $|\eta| < 3.0$ and

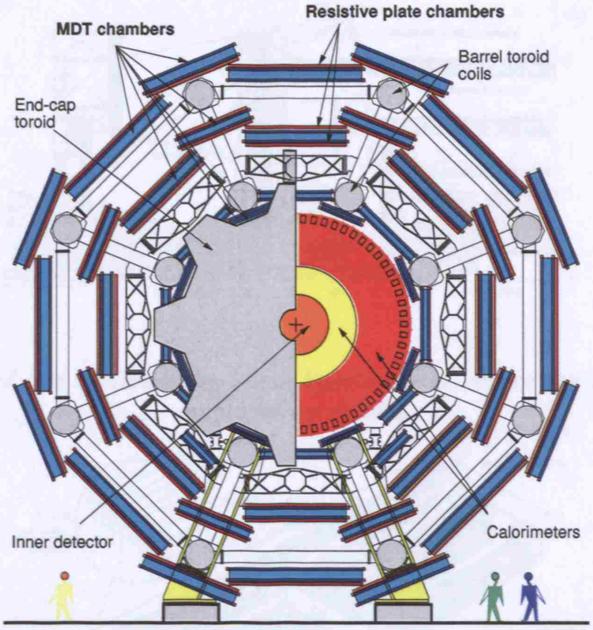

Figure 1.21: Transverse view of the Muon Spectrometer.

$$\frac{\sigma(E)}{E} = \frac{100\%}{\sqrt{E}} \oplus 10\% \tag{1.11}$$

for $3.0 < |\eta| < 4.9$.

1.2.3 The Muon Spectrometer

The Muon Spectrometer is shown in Figure 1.21 and in Figure 1.22. The purpose of the muon spectrometer is to precisely measure the position (and the momentum from the track curvature) of high energy muons, which, due to their insignificant interactions with the matter, managed to escape the rest of the detectors. Since the muons lose energy by ionization, the gas technology is widely used.

The measurement of the position is performed using the precision chambers, which are arranged in such a way that particles from the interaction point cross three layers (stations).

For the region $|\eta| < 2.0$, the technology of the **Monitored Drift Tubes (MDTs)** is employed. The basic detection element of the MDT is aluminum tube of 30 mm diameter

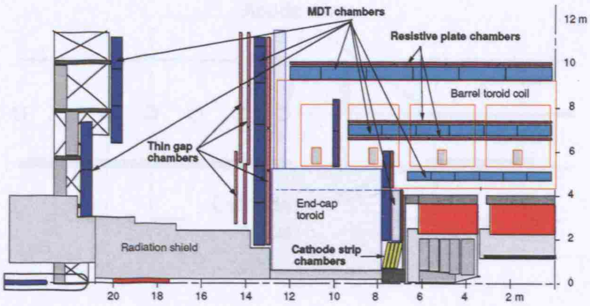

Figure 1.22: Side view of one quadrant the Muon Spectrometer, where the four chamber technologies employed are shown.

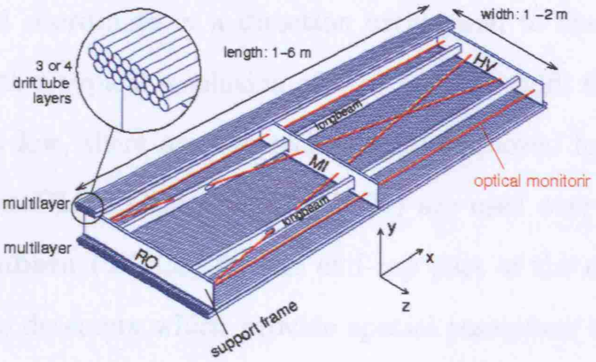

Figure 1.23: Schematic drawing of a rectangular MDT chamber.

and 400 μm wall thickness, with a 50 μm diameter central W-Re wire. The tubes are filled with a non-flammable $Ar-CH_4-N_2$ mixture at 3 bar absolute pressure. The single-wire resolution is typically 80 μm, except very close to the anode wire, where the resolution can reach the 200 μm. An MDT chamber consists of two multilayers of three or four dift tube layers, as is given by Figure 1.23.

For the innermost ring of the inner station at the end-caps ($2 < |\eta| < 2.7$), where particle fluxes are higher, the **Cathode Strip Chambers (CSCs)** (Figure 1.24) are used. The CSCs are multi-wire proportional chambers with a pitch of 2.54 mm between the anode wires and 5.08 mm between the cathode readouts. The second cathode of the chamber is placed perpendicular to the anode wires, providing a measurement of the transverse coordinate. The spatial resolution achieved by the CSCs is approximately 60 μm.

An interesting feature of the muon spectrometer is also the fact that it has its own triggering system, which faces the challenge of good time resolution (less than 25 nsec),

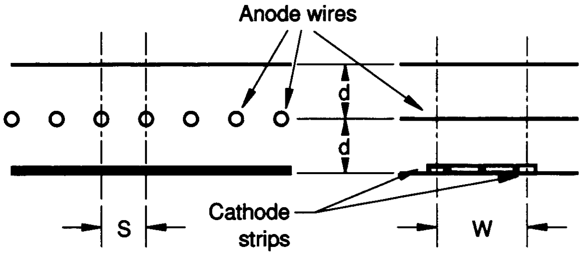

Figure 1.24: Schematic diagram of the Cathode Strip Chamber.

in order to enable bunch crossing identification. The muon trigger system is also designed to measure the second coordinate in a direction orthogonal to the one measured in the precision chambers with a typical resolution of 5-10 mm. To fulfil the above requirements while keeping the cost low, there are two technologies employed for the muon triggering system: The **Resistive Plate Chambers (RPCs)** are used over the barrel region and the **Thin Gap Chambers (TGCs)** for the end-cap part of the detector (Figure 1.22). The RPCs are gaseous detectors which provide spatial resolution of 1 cm in a period of time less than 1 nsec. For each MDT station, there are four RPCs, which are located at both sides of the middle MDT station, at the outer side of the outer MDT station and at the inner side of the inner MDT station. On the other hand, TGCs are designed in a way similar to multi-wire proportional chambers, but with the difference that the anode wire pitch is larger than the cathode-anode distance.There are three stations of TGCs placed near the middle MDT station. One of the most important characteristics of a TGC is its fast response (typical rise-time of 10 nsec) and the time resolution that is of the order of 5 nsec.

Momentum resolution of the Muon Spectrometer

The measurement of the momentum is based on the magnetic deflection of muon tracks. The magnetic field is induced by the large superconducting air-core magnets, the toroidal configuration of which is such that the field is mostly perpedicular to the muon trajectories, while minimising multiple scattering. Together with its own triggering system, the muon spectrometer can perform stand-alone muon reconstruction, which can be combined with

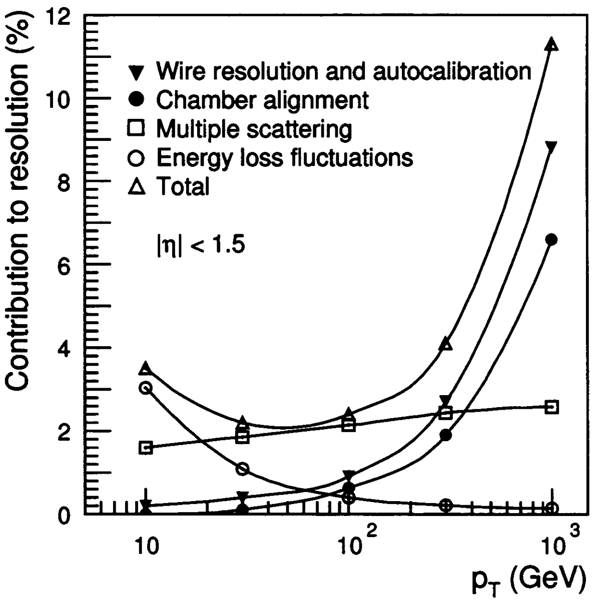

Figure 1.25: Contributions to the momentum resolution of the muon spectrometer, averaged over $|\eta| < 1.5$ and azimuthal angle, in a standard sector.

the information from the Inner Detector to achieve a better perfomance.

Figure 1.25 (from [13]) gives the momentum resolution ($\Delta P_T/P_T$) as it has been computed for the barrel part of the Spectrometer. At low momenta (< 20 GeV), the resolution is limited by energy loss fluctuations, where at high momenta (~ 1 TeV) the detector resolution dominates. The multiple scattering effect is almost constant at 2% all over the momentum spectrum. The total momentum resolution is typically 2-3% over most of the kinematic range apart from very high momenta, where it increases to approximately 11% at P_T=1 TeV.

1.3 The Trigger System

1.3.1 Overview

The task of the ATLAS Trigger System [23] is to efficiently select the interesting (hard-scattering) events, which come from the proton-proton collisions over the background ones, mainly from soft QCD interactions. After selecting these events, the Data Acquisition

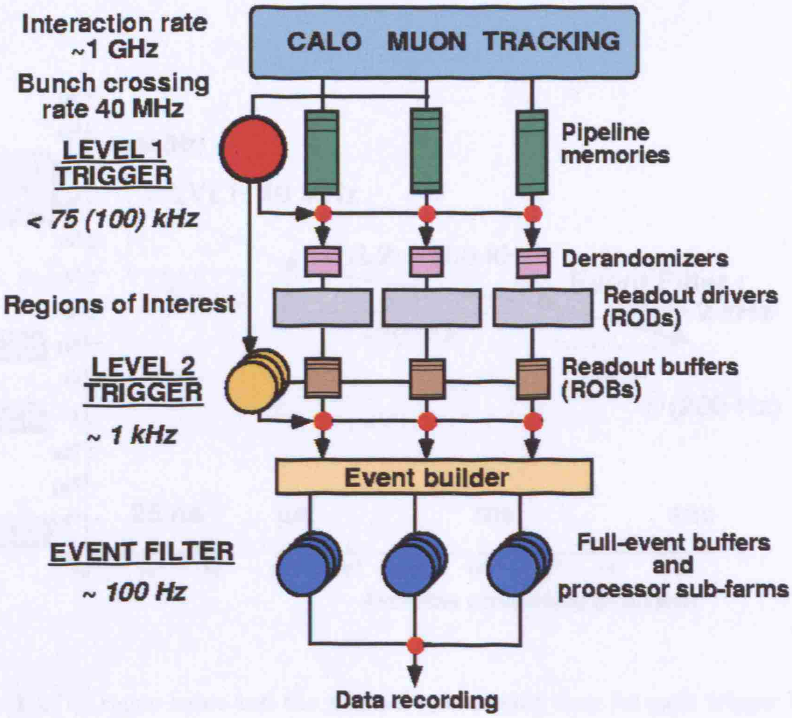

Figure 1.26: Overview of the Trigger and DAQ system.

(DAQ) System is responsible for transferring the data from the individual sub-detectors to the permanent storage elements for the offline analysis.

The ATLAS Trigger consists of three levels, the architecture of which is given in Figure 1.26 and the event rate at each one, together with the available processing time are presented in Figure 1.27.

The first level trigger (**LVL1**)[24] is a hardware based trigger in contrast with the second level (**LVL2**) and the last level (normally named **Event Filter-EF**), which are based purely on software. Together the LVL2 and EF consist what is called the **High Level Trigger (HLT)**[25]. The trigger chain is designed to reduce the event rate of 40 MHz down 100-200 Hz within few seconds. That practically means that only around five in every million bunch crossings will be selected and eventually stored. The final size of each event is expected to be at the order of 1.5 MB and the total amount of data to be stored is estimated to be around 1 PB per year.

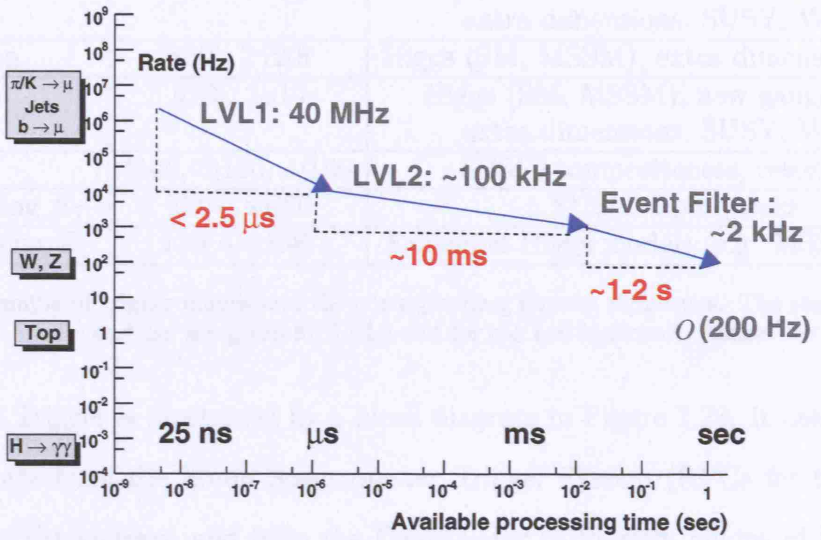

Figure 1.27: Trigger rates and the available processing time for each trigger level.

An important concept of the Triggering system is the **trigger menus**. The trigger menus are combinations of objects, which pass different thresholds and finally are grouped together in a coincidence or in a veto, according to the physics they aim to cover. The current state of the trigger menus is given in [26] and an example is presented in Table 1.1. For instance, 2e15i means that 2 isolated electrons with $P_T > 15$ GeV are required. The trigger menus are designed so as to make sure that they include all the interesting physics that is known or expected. On the other hand these menus should be inclusive to the unexpected physics. It is essential to mention that the trigger menus are constantly evolving in order to achieve the optimal final efficiencies and rejection factors, but they will also be updated during the running of the experiment, once the performance of the detector is well understood.

1.3.2 The LVL1 Trigger

As it can be seen by Figure 1.27, the LVL1 Trigger is designed to reduce the bunch crossing of 40 MHz down to approximately 100 kHz. The designed time for LVL1 to take and pass the decision (usually called latency) is 2.0 μs with 0.5 μs safety margin.

Trigger Objects	Trigger Items	Examples of physics coverage
Electron	e25i, 2e15i	Higgs (SM, MSSM), new gauge bosons extra dimensions, SUSY, W, top
Photon	γ60i, 2γ20i	Higgs (SM, MSSM), extra dimensions, SUSY
Muon	μ20i, 2μ10	Higgs (SM, MSSM), new gauge bosons extra dimensions, SUSY, W, top
Jet	j400, 3j150, 4j100	SUSY, compositeness, resonances
Jet + Missing E_T	j60 + xE60	SUSY, leptoquarks
Tau + Missing E_T	τ30 + xE40	Extended Higgs models (e.g. MSSM), SUSY

Table 1.1: Example of trigger menus and the corresponding physics signatures. The required values for P_T and E_T are given for LVL2 and for the low luminosity phase.

The LVL1 Trigger is illustrated by a block diagram in Figure 1.28. It uses the reduced granularity data from the Muon Spectrometer Trigger System (RPCs for the the barrel and TGCs for the endcap) and from the Calorimeter to identify muons of high P_T, jets, large missing transverse energy and (isolated) electromagnetic clusters, which come from electrons, photons and taus decaying into hadrons.

The detailed technical description and the performance of the LVL1 Trigger can be found in [27]. It is, however, essential to comment on how the Calorimeter is used for the LVL1 Trigger. All of the Calorimeter components are divided into **Trigger Towers**, which have granularity of $\Delta\eta \times \Delta\phi = 0.1 \times 0.1$ for $|\eta| < 2.4$. Signals from the more forward calorimeters, required for the trigger, are used with a coarser granularity. The signal of each tower is simply the summation of all the signals from the cells belonging to this tower and then front-end preprocessors digitize the signal.

The output of the Calorimeter and Muon Trigger is passed to the Central Trigger Processor (CTP), which makes the decision according to the Trigger Menus, specially designed for this level. The CTP passes then the decision to the Timing, Trigger and Control (TTC) system, which is responsible for distributing the signals to the front-end system. During the time that LVL1 needs to take the decision, the data are stored in pipelined memories, until they are either passed to the next level trigger or deleted once and for all. A positive result from LVL1 contains information about the type and the thresholds of the accepted trigger and also the geometrical position of the interesting activity. The latest piece of information is used by LVL2 to construct the Region of Interest, as it will

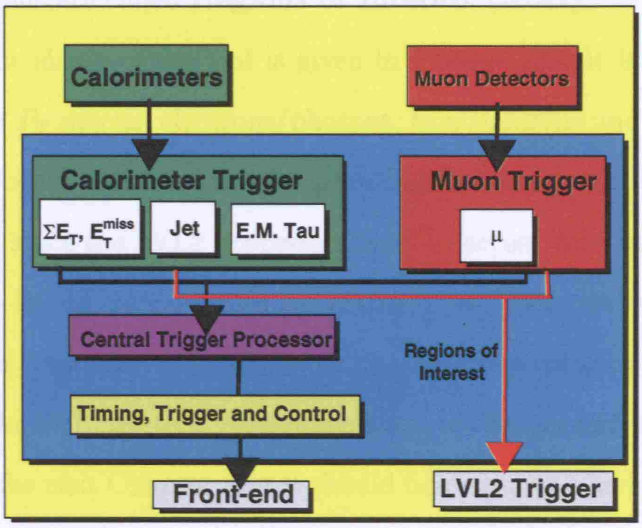

Figure 1.28: Block diagram of the LVL1 trigger system

be discussed during the next section.

A major requirement of the LVL1 is that it should be able to uniquely identify the time of the bunch crossing. For this reason the processors at this level are synchronized with the 40 MHz LHC Clock, which gives the signal for the data acquisition. LVL1 also accepts the bunch-zero signal, which identifies the number of the bunch crossing in the LHC machine.

1.3.3 The LVL2 Trigger

Overview

LVL2 has to reduce the rate coming from LVL1 (maximum of 100 kHz) down to approximately 2 kHz, within a period of time of about 10 ms.

When an event is accepted by LVL1, the data for this event are moved from the pipeline memories to the specially designed **Read-Out Buffers (ROBs)**, where they are stored for the whole processing time of LVL2. LVL2 can access event data from all the ATLAS sub-detectors with the **full** granularity and precision and in the case of a positive decision, the whole event is passed to the next level. Since the available time is not sufficient for a full event reconstruction, LVL2 is looking only into the specific interesting regions identified by LVL1. These regions are called **Regions of Interest (RoIs)**.

An example of the shape of the RoI is given in Figure 1.29. It is the region at which LVL1 has found high P_T muons, electrons/photons, taus/hadrons and jets and it is passed to LVL2 in the form of its position in $\eta - \phi$ space together with the LVL1 thresholds. The RoI plays a key role, since the LVL2 processors need to access data fragments only from a small fraction of the ROBs, as explained by Figure 1.30. This mechanism (selecting and transferring only the important data) reduces the required network bandwidth and the computing load on the LVL2 system. The dimensions of the RoI and how it is constructed will be explained in the next Chapter, but it should be mentioned here that the typical size of an RoI containing an electromagnetic cluster is $\Delta\eta \times \Delta\phi = 0.2 \times 0.2$. This size and the location of the RoI can be further defined more accurately after each LVL2 processing step, resulting in a further reduction of the required CPU resources.

At LVL2, the event processing can be divided into the following steps:

- **The Feature Extraction (FEX):** At this stage, for each RoI, the data from the detectors are grouped together to form physics-like quantities. For example, in the case of the calorimeter, that would mean that the cells are grouped to give the clusters.

- **The Object Building:** The elements constructed by the previous step are combined, for each RoI again, to give the particle parameters and the particles' type, wherever that is possible. For instance, the shape of an EM cluster can be combined with the absence of a track in the ID to form a photon.

- **The Trigger Type Selection:** At this phase, all the objects found inside all RoIs are combined with the rest of the event topology (missing E_T for instance) and the resulting combinations are checked against the Trigger Menus (Table 1.1). For each Trigger Menu a flag is set.

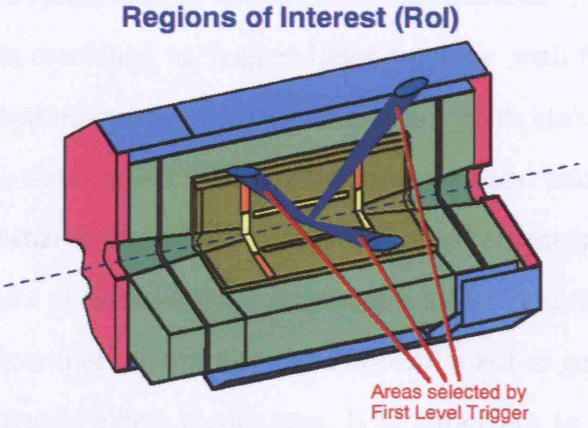

Figure 1.29: Geometrical shape of the Region of Interest.

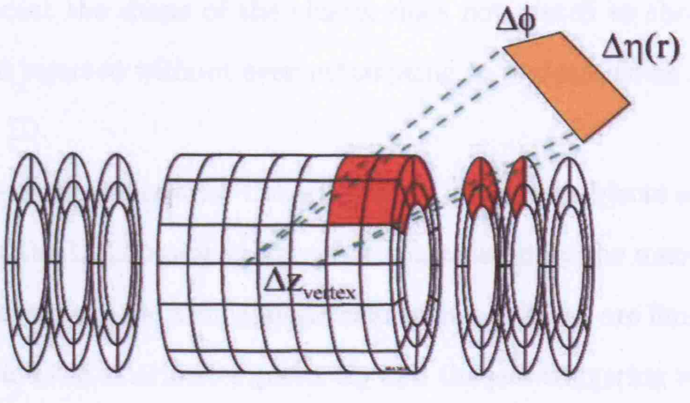

Figure 1.30: For each RoI, only the Detectors Elements which are located inside are transfered from the ROB and analyzed by the LVL2 algorithms.

Event Selection

The event selection at LVL2 [28] uses the Trigger Menus in the same way as they were used at LVL1: Trigger Objects such as muons, electrons, photons [5], charged hadrons, taus, jets and missing E_T are combined in Trigger Items together with the Trigger Conditions (number of Objects, Isolation criteria, P_T and/or E_T thresholds etc). The difference is that the Trigger Objects are constructed with a better accuracy and using the full granularity, but also the Trigger Items include tighter cuts compared to the previous level. At the same time, LVL2 consists of selection criteria that are looser than those used for the final analysis, since the resolution of the reconstructed objects is not as good as the one achieved using the more sophisticated offline algorithms. It is important to stress once again that the Trigger Menus will evolve with the first analyses of the data and that different sets are foreseen according to the luminosity of the LHC machine.

An important feature for the event selection at LVL2 (but also at the EF) is the sequential approach to signature validation. After each feature extraction step, the result is checked against each individual trigger item and therefore uninteresting events are rejected at the earliest possible step. For example, for an event that has been accepted by LVL1 due to an electromagnetic RoI, LVL2 tries first to reconstruct the EM cluster, at the FEX stage. If at that point the shape of the cluster does not match to that of an electron or photon, the event is rejected without even attempting to perform track reconstruction and matching with the ID.

Finally, the geometrical limits for the acceptance of trigger objects are given by the detector: the limits of the LVL2 muon triggers are constrained by the muon trigger chambers ($|\eta| \leq 2.4$), the tracking and electromagnetic calorimeter triggers are limited to $|\eta| < 2.5$ by the inner detector and the calorimeter geometry and the jets triggering will use information up to $|\eta| < 3.2$.

---

[5] At this stage, in contrast with LVL1, it is possible to distinguish between electrons and photons.

1.3.4 The Event Filter

The last level of the Triggering System (EF) is the stage just before the whole information from all the detectors is stored to the permanent storage. It receives the approximately 2 kHz of the previous LVL2 Trigger and it has to reduce it further to the order of 100 Hz within few seconds. Since there is enough time, more sophisticated algorithms are used, often similar to those used for the offline analysis, allowing thus a direct comparison.

The selection algorithms are seeded by the LVL2 result and they have access to the data from all the detector systems, to the full detector geometry and calibration databases. Together with the primary task of the event filtering, the EF will also perform monitoring and calibration/alignment tasks. This is feasible due to the long available processing time, but also due to the access to the complete events.

The time for data transfer at the EF will be a very small fraction of the total latency. The rest will be spent on the data processing. Therefore EF will be using intensively the available CPU, which -most likely- will be in a farm of commercial processors.

CHAPTER 2

Reduction of the Region of Interest size using the EM calorimeter

This chapter is the work which has been reported in [29] and presents the study for optimizing the size of the EmTau Region of Interest (RoI) using the pointing information from the Electromagnetic Calorimeter. The benefits from the reduced RoI size in terms of timing and performance for track reconstruction in the Inner Detector at LVL2 Trigger using the IDSCAN package are discussed in detail.

2.1 Introduction

As was explained in the previous chapter, the concept of the **Region of Interest (RoI)** plays a crucial role in the Trigger System of ATLAS since it defines a geometrical area in which the LVL1 trigger identified some activity based on which it accepted the event. It has also been mentioned that at the LVL2 trigger stage, only the data within the RoIs in the event are transfered from the readout buffers (ROBs) to the LVL2 processors, to reduce CPU and network usage [30]. Each event can have more than one RoI, depending on the event topology. There are, on average, 1.4 RoIs per LVL1 accepted event and each

RoI represents $\sim 2\%$ of a complete event data volume [31]. As a result the dimensions of the RoI are of major importance, having a direct impact on the network data volume and CPU processing resources required to handle the event, and therefore to the effectiveness of the LVL2 trigger.

There are several types of RoI, including electromagnetic, muonic and jet RoIs. The study presented in this note refers only to the electromagnetic RoIs, which include e/γ and τ objects, and so are referred to as **EmTau** RoIs [25]. Information for the EmTau RoI comes only from the calorimeter at LVL1, in the form of an electromagnetic cluster.

2.1.1 Dataset and event selection

The subsequent study was performed using single electron Monte Carlo events generated with $P_T = 20$ GeV and added to pile-up events at low luminosity ($\mathcal{L} = 10^{33}\ cm^{-2}sec^{-1}$) and a sample of single electrons generated with $P_T = 30$ GeV and added to pile-up events at high luminosity ($\mathcal{L} = 10^{34}cm^{-2}sec^{-1}$). The events were then reconstructed using the 9.0.4 ATLAS Offline software release, with the noise in the LAr calorimeter switched on. For the reconstruction inside the calorimeter during the LVL2 trigger, the `T2Calo` package was used. For each event, the number of RoIs, the clusters reconstructed by `T2Calo` (online clusters) together with the clusters reconstructed by the offline calorimeter package (offline clusters) were used.

Since the modified RoI description is intended for use online during the trigger chain, the online clusters are appropriate. However, for release 9.0.4 the LVL2 clusters were missing important information, such as the energy deposited in each sampling, due to the fact that this information had not been required before[1]. Consequently, for the current study, the offline clusters were used instead.

---

[1] The work to introduce the required information to the LVL2 clusters was underway by the time of preparing this Thesis.

2.2 The shape of the Region of Interest

2.2.1 The current RoI

Processing of an EmTau RoI at LVL2 starts from the calorimeter. The `LVL2Calo` code [32, 33, 34, 35] has access to the η_{LVL1} and ϕ_{LVL1} information and it uses the full calorimeter granularity. Based on this information, `LVL2Calo` determines with better precision than LVL1 processing the position of the RoI and passes it on to LVL2 tracking.

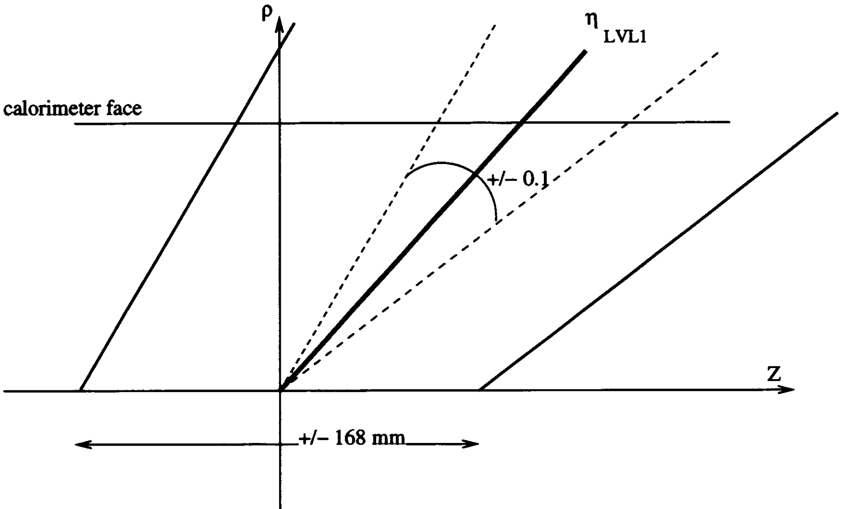

Figure 2.1: Construction of the RoI in the $\rho - z$ plane at LVL2 trigger level. The quantity ρ is defined as $\rho = \sqrt{x^2 + y^2}$, in the coordinate system given by Figure 1.5.

The currently implemented shape of the EmTau RoI, used by the LVL2 tracking algorithms, is described in Figure 2.1. LVL1 gives the η position (with respect to the origin of the detector) of the accepted EM Cluster. The RoI is shaped by opening by $\Delta\eta \times \Delta\phi = 0.2 \times 0.2$ around this direction. The resulting pyramid is extended at its tip, near the beam line, by $\Delta z = \pm 168$ mm to take account of the spread in the position of the interaction vertex along the beam direction. Figure 2.2 gives the distribution of the z coordinate of the primary proton-proton interaction in single electron simulated events. The interaction vertex has been randomly selected from a normal distribution with $\sigma = 5.6$ cm. Therefore, the extension of the RoI along the beam line corresponds to ±3 standard deviations of the vertex spread.

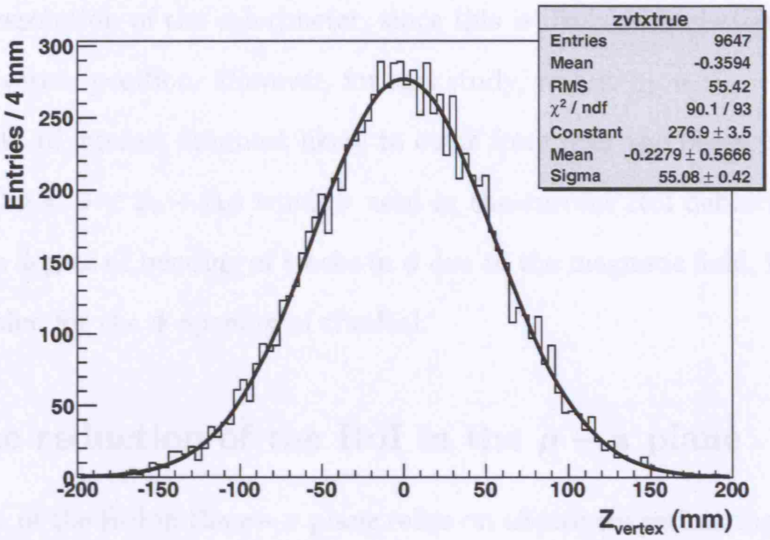

Figure 2.2: Distribution of the vertex of the primary proton-proton interaction along the z-direction.

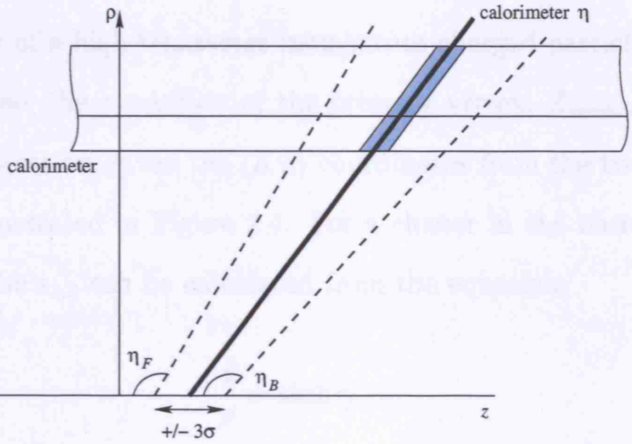

Figure 2.3: Proposed improvement of the RoI in the $\rho - z$ plane at LVL2 trigger level. The value of σ is taken from the gaussian distribution of Figure 2.2.

2.2.2 An improved RoI

In this study we aim, using the information from the different samplings of the electromagnetic calorimeter, to obtain an estimate of the z-position of the primary interaction to allow the reduction of the size of the RoI in η. This is illustrated in Figure 2.3. Because of the improved estimate of the vertex position, the required window in z need not cover the entire interaction region. In addition, allowing the opening of the window in pseudorapidity to be independent at either end, i.e. allowing η_F and η_B to be independent, allows the trapezoid search window in the $\rho - z$ plane to be closed at the calorimeter face using the position resolution of the calorimeter, since this is likely to be better known than the extrapolated vertex position. However, for this study, we use $\eta_F = \eta_B = \eta$.

Since tracks of interest are most likely to come from near the beam line, we retain the simple $\phi_0 - \Delta\phi < \phi < \phi_0 + \Delta\phi$ window used in the current RoI definition. However, we also study the degree of bending of tracks in ϕ due to the magnetic field, in order to choose an optimal value for the ϕ opening of the RoI.

2.2.3 The reduction of the RoI in the $\rho - z$ plane

The reduction of the RoI in the $\rho - z$ plane relies on effectively estimating the z position of the primary interaction vertex using the first and second samplings of the LAr calorimeter.

Since the trajectory of a high transverse momentum charged particle is approximately linear in the $\rho - z$ plane, the z position of the primary vertex, Z_{vertex}, can be estimated by simple linear extrapolation, given the (ρ, z) coordinates from the two samplings of the calorimeter. This is illustrated in Figure 2.4. For a cluster in the barrel calorimeter, the $\rho_{1,2}$ are known, while the $z_{1,2}$ can be calculated from the equation:

$$\frac{z}{\rho} = \sinh\eta \tag{2.1}$$

where the index refers to 1st or 2nd sampling and the η is calculated with respect to the origin of the detector. For a cluster in the calorimeter endcap, the $z_{1,2}$ are known and the $\rho_{1,2}$ are calculated from equation 2.1. The primary vertex position can then be calculated from the coordinates of the two points using:

$$Z_{\text{vertex}} = \frac{z_1\rho_2 - z_2\rho_1}{\rho_2 - \rho_1}. \tag{2.2}$$

From the geometry of the LAr calorimeter, one can get the maximum radius of the 1st and 2nd barrel samplings and the maximum z of the 1st and 2nd endcap samplings. This is plotted in Figure 2.5. For the barrel (endcap) coordinates $\rho_{1,2}$ ($z_{1,2}$), it is clear that there is no obvious choice for which values to actually use. The following options were studied

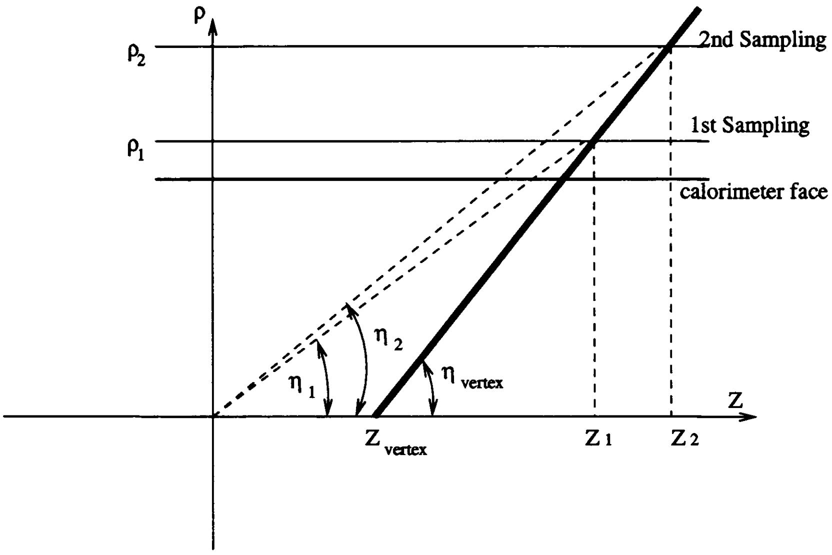

Figure 2.4: Definition of the quantities given in eq. 2.1 and eq. 2.2.

and, for each one, the resolution for Z_{vertex} was checked.

- Option 1: The maximum values of $\rho_{1,2}$ (barrel samplings) and $z_{1,2}$ (endcap samplings), as given by Figure 2.5. The resolution achieved was 49.76 mm.
- Option 2: The geometrical centre of each sampling with fixed values of ρ_1=1545.3 mm, ρ_2=1759.2 mm, z_1=3766.0 mm and z_2=3980.0 mm. The resolution achieved was 55.53 mm.

Therefore, the outermost points of the samplings were used and the analytical equations of the parametrisation functions used are given in Appendix A.

After this calculation, we have an estimation of the vertex position in z making use only of the calorimeter information. The RoI can then be extended along the z-axis by an amount depending on the Z_{vertex} resolution, parameterized as a function of η. The window used throughout this study is $\pm 3\sigma$ of the Z_{vertex} resolution.

2.2.4 The crack region in the LAr Calorimeter

The information for the energy deposited in a cluster comes in a sequence of 2 blocks. The first block includes the energy deposited in the presampler and the first, second and third samplings of the barrel part of the Calorimeter, whereas the second block refers to

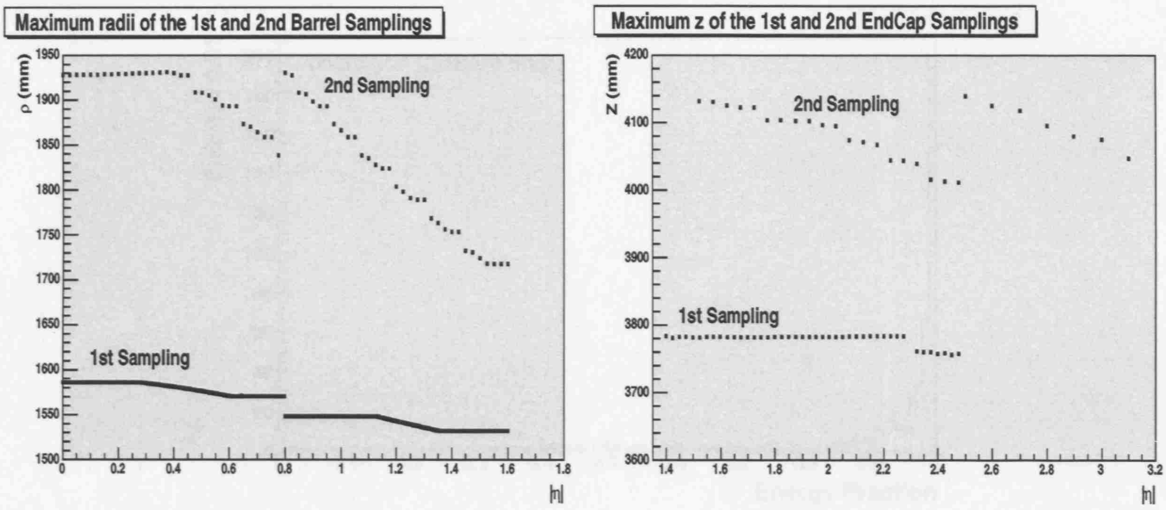

Figure 2.5: The maximum radius of the 1st and 2nd barrel samplings (left) and the maximum z of the 1st and 2nd end-cap samplings (right). The break at $|\eta| = 0.8$ is due to the thinner lead used in the absorber plates.

the same quantities for the endcap part. Thus, a cluster is regarded as a pure barrel when the second block has zero values and as a pure endcap when the first block has zero values. Whether the cluster is barrel or endcap, either the ρ or the z coordinate is known from the geometry, with the other coordinate being calculated from the cluster position, as discussed previously. However, in addition, there are cases where the energy of the cluster is deposited in both the calorimeter barrel and endcap, which results in both blocks having non-zero values. The majority of such "transition region" events can be treated as barrel events, since most of their energy is deposited in the barrel, as demonstrated by Figure 2.6.

Events where more than 90% of the energy is in the barrel (endcap) are treated as barrel (endcap) events. Studies showed that when the energy is split more evenly between barrel and endcap, the determination of Z_{vertex} is unreliable, so the reduction of the RoI size in η is not applied to these events. The number of events in each category is shown in Table 2.1.

2.3 Implementation and results

In order to evaluate the effectiveness of the proposed method and determine the optimal values for the different parameters (for example of the $\Delta\phi$ window), the LVL2 tracking

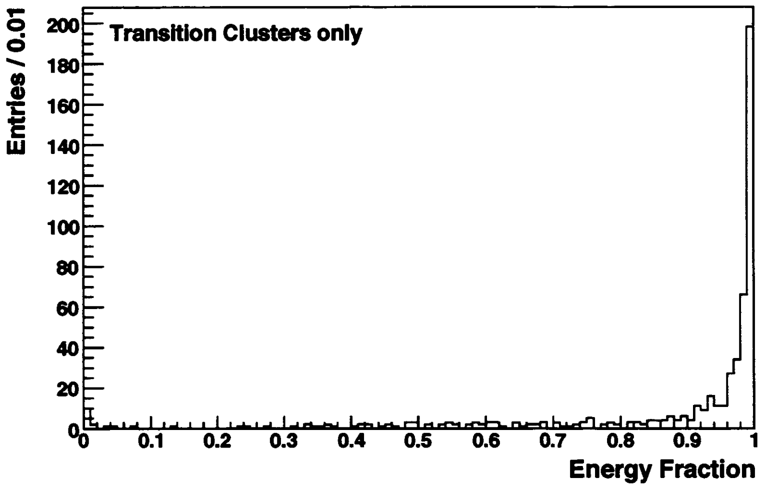

Figure 2.6: Fraction of the energy deposited in the barrel samplings from a transition region cluster. Most of the energy is deposited at the barrel part, since this is before the endcap one.

	Low Luminosity	High Luminosity
Events Processed	4,720	9,647
Barrel Events	2,650 (56.1%)	5,164 (53.5%)
Endcap Events	1,870 (39.6%)	3,751 (38.9 %)
Transition Events	200 (4.2%)	732 (7.6%)
η reduction wasn't applied	92 (1.9%)	441 (4.6%)

Table 2.1: Event Statistics for optimizing the RoI size.

package IDSCAN was used. The architecture and performance of IDSCAN are described elsewhere [36, 37]. Using three-dimensional space points from the Pixel and the SCT detectors, IDSCAN starts by finding the vertex of the primary interaction and uses this to reconstruct tracks in the Inner Detector. This first step is performed using the ZFinder algorithm [38].

For comparison purposes, IDSCAN was seeded first with the space points contained in the original RoI as defined in Section 2.2.1. The RoI was subsequently defined in η and ϕ according to the prescription described above and IDSCAN was executed over the same events, seeded this time with the space points contained in the reduced RoI. The performance was evaluated each time in terms of the efficiency for determining the vertex

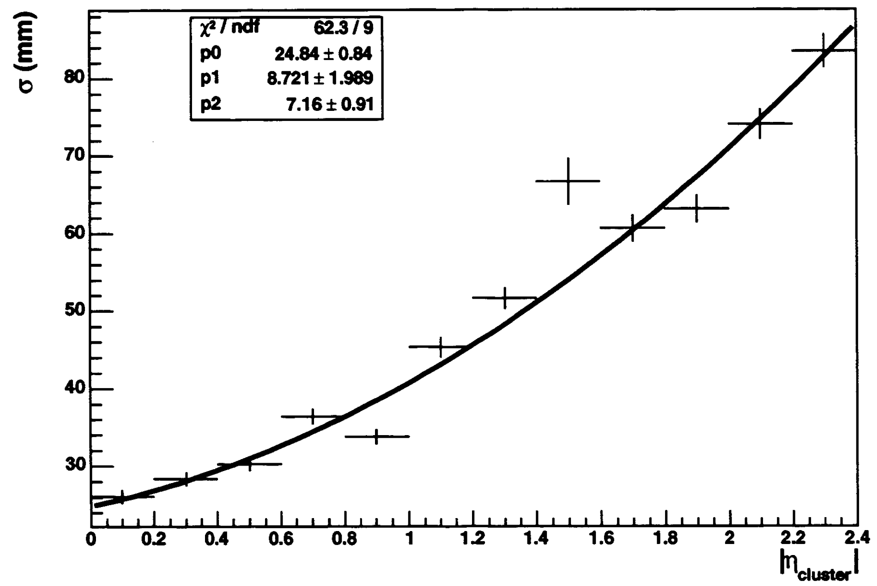

Figure 2.7: Calorimeter pointing resolution as a function of η, fitted with a parabola.

of the primary interaction, where correct determination was defined to be when:

$$|Z_{\text{vertex}} - Z_{\text{true}}| \leq 2\,\text{mm} \tag{2.3}$$

2.3.1 The Z_{vertex} resolution and reduction of RoI extent in z

In order to open a window around the z position which is calculated using the calorimeter, it is first necessary to know the resolution with which Z_{vertex} can be determined. This is shown in Fig.2.7 as a function of the absolute value of the η of the cluster and it was checked that it does not depend on the luminosity. The absolute value of η is used here to increase the statistical significance, since the distribution was seen to be symmetric in η. Both the dependence of the resolution for the high and low luminosity samples are similar indicating that the resolution is not significantly influenced by the additional pp pile-up interactions in the bunch crossing and the different electron transverse momenta.

For the very central region, the resolution is of the order of 25 mm, rising to approximately 80 mm in the forward region. The drop of the resolution around $|\eta|$=0.8 is caused by the thinner lead used in the absorber plates [2].

---

[2] In the barrel region, the particles travel through more passive material at higher η values To compensate

The resolution is worse for η approximately in the range 1.4-1.6, which is due to the transition region. The data were fitted using a second order polynomial with the parametrised form:

$$\sigma = 7.16 \cdot |\eta|^2 + 8.72 \cdot |\eta| + 24.84 \quad \text{(mm)} \tag{2.4}$$

Although a symmetric function is really desired to reflect the symmetry of the detector and the observed variation of the resolution, the small difference with respect to this around $|\eta| \sim 0$ is of minor significance since the spread of the resolution at any $|\eta|$ itself is large, and variations in the calorimeter granularity might cause differences from the smooth functional form if greater statistics were available.

2.3.2 The ϕ resolution and reduction of RoI extent in ϕ

The residuals in ϕ of the true electron position with respect to the calorimeter cluster position are shown in Figure 2.8 for both low and high luminosity events with no corrections for bremsstrahlung and no extrapolation from the calorimeter back to beam axis. The different P_T of the electrons in the two samples is responsible for the difference in the overall shift of the peaks – the higher momentum of the high luminosity sample meaning the track bends less in the magnetic field.

The degree of curvature in ϕ is additionally different for particles in the barrel and the endcap regions due to the weaker magnetic field towards the endcaps [39]. It is worth noting that the form of the ϕ residual has contributions from several sources. Although the position of the peak would be in principle calculable from the bending of the track in the magnetic field, the position will also be smeared by the calorimeter resolution in ϕ and smeared to larger $|\Delta\phi|$ by bremsstrahlung and energy loss as the track travels through the material of the detector. For this reason, optimizing the ϕ window of the RoI merits a study, where the effects of both calorimeter resolution and bremsstrahlung are properly taken into account.

---

for this problem, for the barrel region with $|\eta| > 0.8$, the thickness of the lead used for the absorber plates is reduced and this is demonstrated as a discontinuity in the border where the two regions meet.

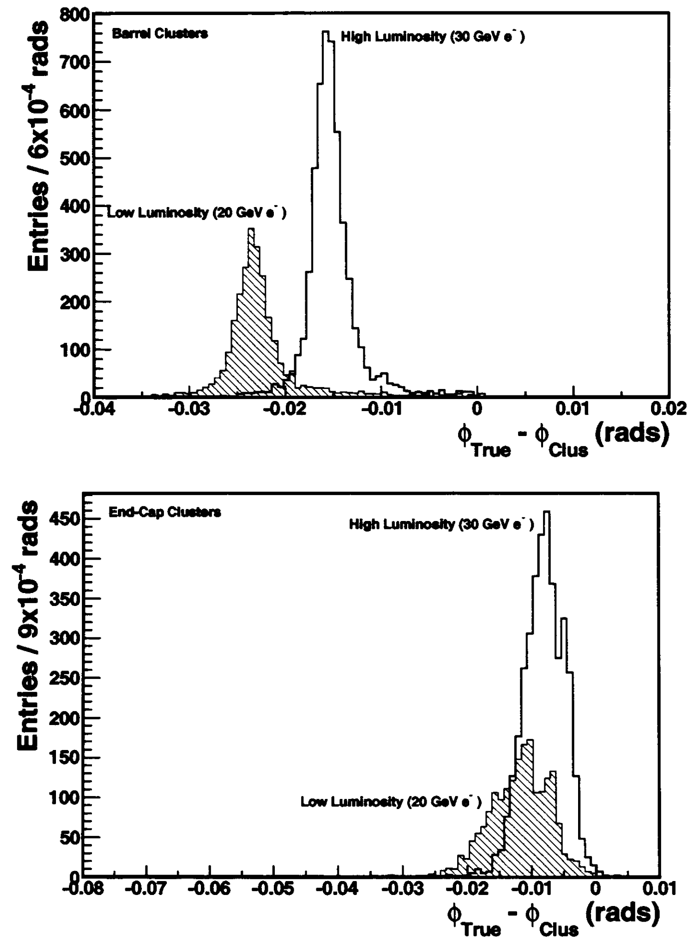

Figure 2.8: The ϕ resolution of the electromagnetic clusters in the barrel region (top) and in the end-cap region (bottom) for low and high luminosity.

Since for electrons with $P_T > 20$ GeV the $|\Delta\phi|$ residual is always less than 0.04 rad it is clear that the ± 0.1 rad window in ϕ used until now is too large for these RoIs. Although this would not naïvely be expected to affect the efficiency, if all the hits are included within the RoI, the large extent of the RoI means that a significant number of pile-up hits at large $\Delta\phi$, not associated with the electron will be included in the pattern recognition stage of the algorithm. This will increase the number of unwanted, incorrect combinations that have to be considered (therefore extending the execution time of the algorithm) and increase the possibility of an incorrect assignment being made, so reducing the efficiency.

In order to find the optimal size in ϕ for each region of the calorimeter, and for each data set, we applied different windows around the reconstructed ϕ position of the cluster, and studying the effect on the Z_{vertex} efficiency of the IDSCAN ZFinder.

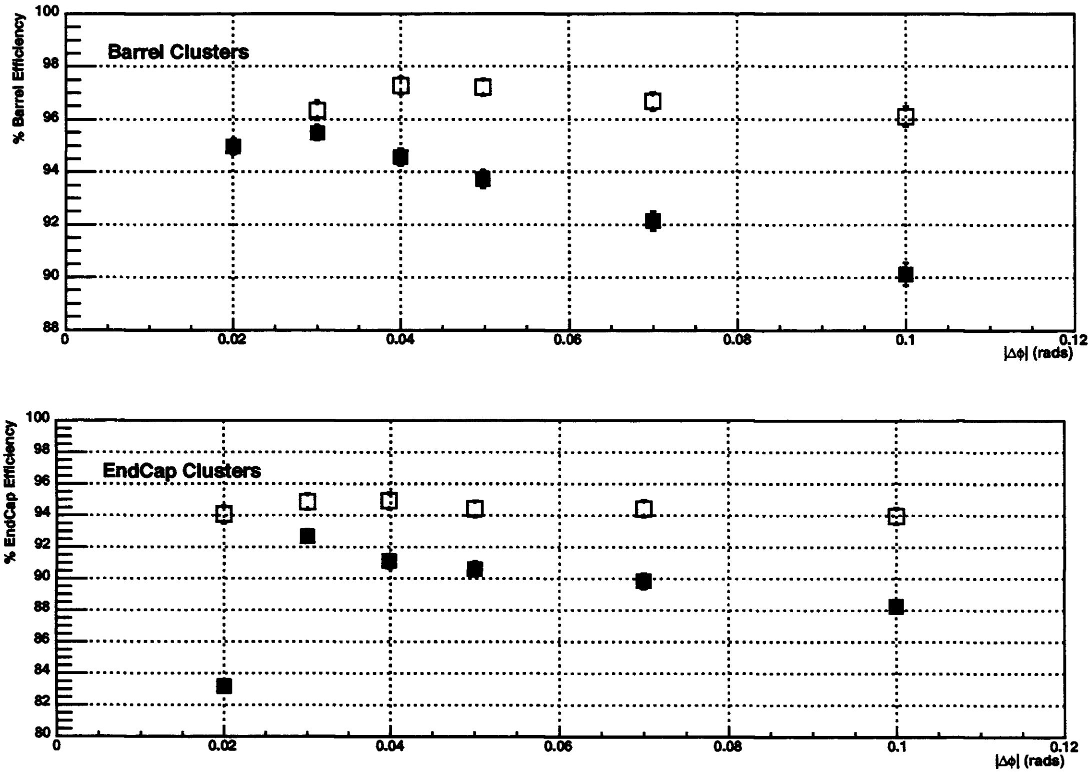

Figure 2.9: Effect of the ϕ window around the cluster on the ZFinder efficiency for low (open squares) and high (solid squares) luminosity events.

The results are illustrated in Figure 2.9. As the $\Delta\phi$ window increases from 0, more of the space points from the tracks are included so that the efficiency approaches its maximum. As we move out from the peak to include the entire distribution within the window, the efficiency falls: further increasing the window, allows more and more background space points to be included, but with no additional space points from the tracks themselves, so increasing the chance of an error in the pattern recognition.

In our case, the positions of the maxima in the residuals lie at different $\Delta\phi$ for the high and low luminosity samples, so the position of the maxima on the efficiency curves are different – for example, for the barrel samples the maxima lie near 0.03 rad for the high luminosity sample and 0.04 rad for the low luminosity sample.

Of course, during real data taking conditions, the trigger would have to deal with the full spectrum of electron momentum, and as such, the window size would be dependent on the lower threshold of P_T of electrons that were required to pass the trigger. A common window of $\Delta\phi = \pm 0.04$ rad around ϕ_{cluster} should therefore be sufficient for electrons with $P_T > 20$ GeV and this has been applied for the results presented here.

In contrast to the reduction in the $\rho - z$ plane, the reduction in ϕ was also applied to electrons in the calorimeter transition region as well as those in the barrel and endcap regions.

2.3.3 Improvement on the ZFinder efficiency

The efficiency for reconstructing the correct primary vertex as a function of $|\eta|$ for both high and low luminosity is given in Figure 2.10. Figure 2.11 and Table 2.2 summarize the efficiencies for each of the barrel, endcap and transition regions of the detector as well as the overall efficiency. It can be seen that the efficiency achieved using the new reduced RoI is higher than that obtained using the original RoI description. Since the ZFinder is a combinatorial algorithm, reducing the size of the RoI leads to fewer combinations of random background space points. This means the likelihood of obtaining an incorrect combination of hits is reduced, while that for finding a correct combination should remain unchanged. For exactly this reason, the observed improvement is larger with the high luminosity events (6%) than in the low luminosity case (1.3%).

	Low Luminosity		*High Luminosity*	
	Original RoI	**Reduced RoI**	**Original RoI**	**Reduced RoI**
Barrel	96.11 ± 0.38	97.36 ± 0.31	90.12 ± 0.42	96.69 ± 0.25
Transition	95.00 ± 1.54	94.50 ± 1.61	92.62 ± 0.97	95.63 ± 0.76
End-cap	93.96 ± 0.55	95.35 ± 0.49	88.24 ± 0.53	92.59 ± 0.43
Overall	95.21 ± 0.31	96.44 ± 0.27	89.58 ± 0.31	95.01 ± 0.22

Table 2.2: ZFinder efficiencies.

2.3.4 Improvement on the ZFinder execution time

The design of the ZFinder algorithm means that the execution time is found to scale almost linearly with the number of space points in the RoI so that a reduction in the size of the

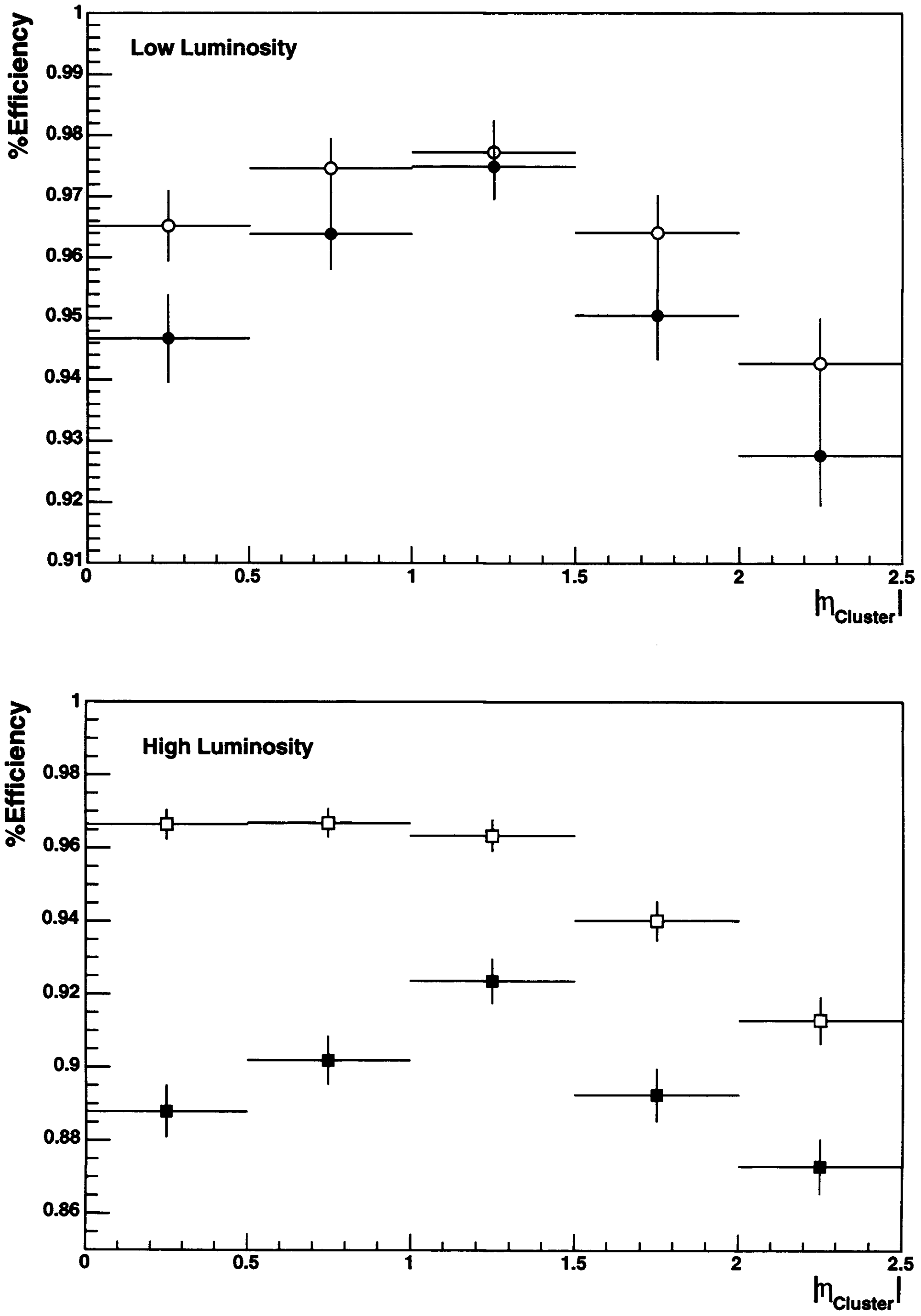

Figure 2.10: ZFinder efficiencies as a function of $|\eta|$ for low (up) and high (down) luminosity using the original RoI (solid markers) and the reduced RoI (open markers).

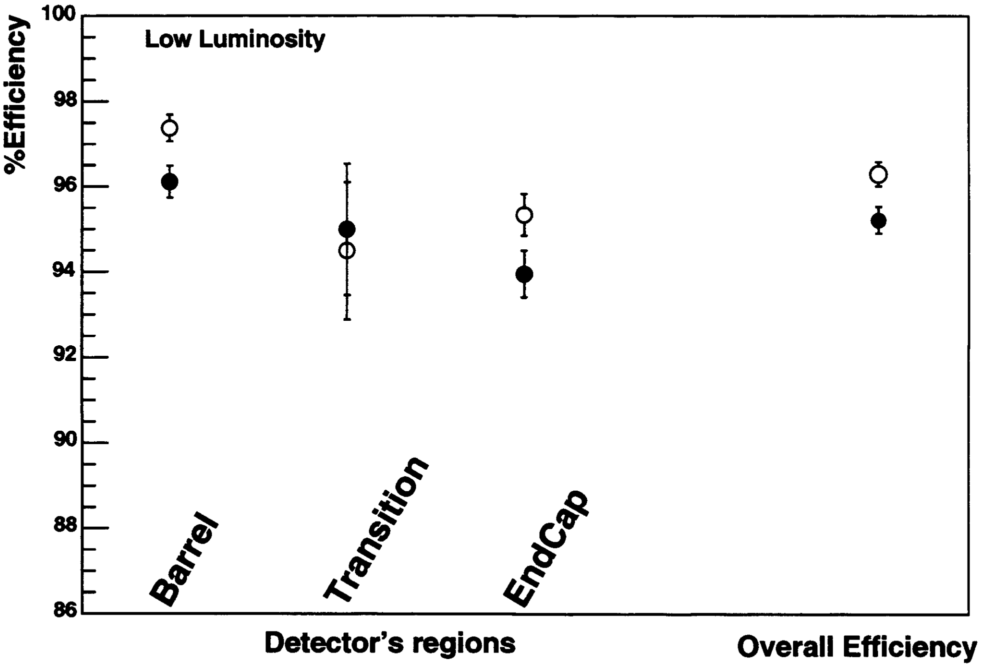

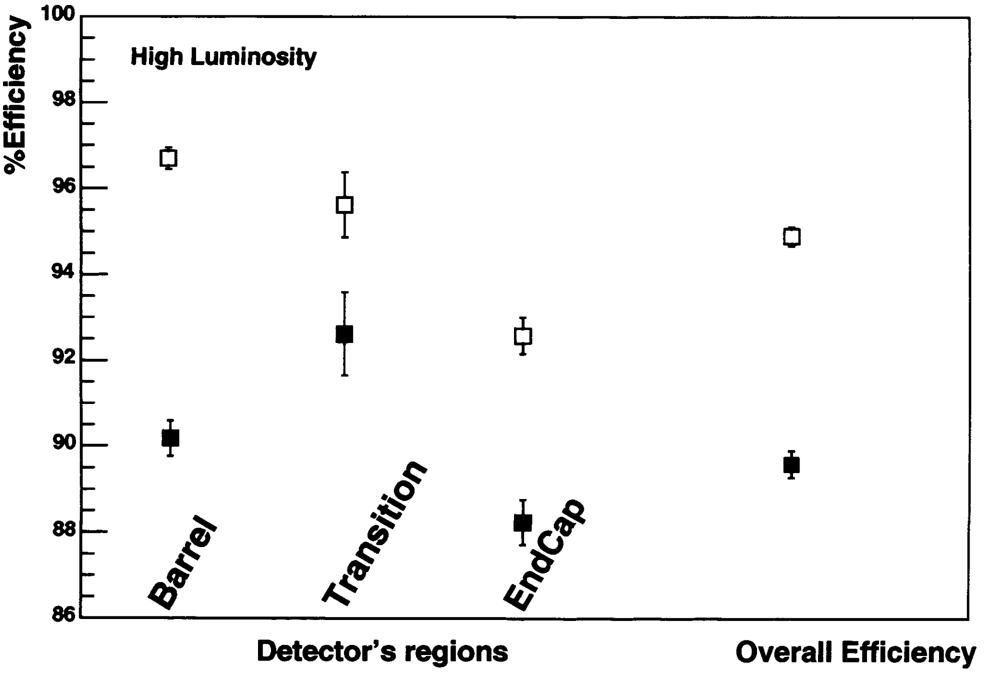

Figure 2.11: ZFinder efficiencies for the barrel, transition and end-cap regions of the detector for low (up) and high (down) luminosity using the original RoI (solid markers) and the reduced RoI (open markers). The overall efficiency is also given at the right of the graphs.

	Low Luminosity		*High Luminosity*	
	ZFinder mean execution time	**Mean number of space points**	**ZFinder mean execution time**	**Mean number of space points**
Original RoI	0.32 ms	43.06	0.81 ms	156.2
Reduced RoI	0.23 ms	18.12	0.34 ms	44.07
% difference	-28.13%	-57.92%	-58.02%	-71.79%

Table 2.3: Improvement on ZFinder mean execution time and on the mean number of space points.

RoI would be expected to lead to an improvement, not only in the transfer time of the data, but also in the execution time of the algorithm itself.

For this study, the execution time of the ZFinder was measured using a 2.4 GHz Pentium-IV processor. Table 2.3 shows the results for execution time of the ZFinder obtained using both the original and the reduced RoI definitions for both high and low luminosity samples. The mean execution time is reduced by ~28% in low luminosity RoIs and by ~58% in high luminosity RoIs.

In the same table, the number of space points contained in the reduced RoI is also shown and is almost a factor four smaller compared to the original RoI at high luminosity, which directly reflects the actual reduction of the RoI size. At high luminosity, the number of space points from the true electron is essentially negligible compared to the total so the execution time is dependent purely on the data volume.

This result is particularly important, because the average execution time for LVL2 tracking is dominated by the data preparation, i.e. the unpacking of the Pixel/SCT bytestream, the clustering and the space point formation. Therefore, a significant improvement in the overall execution time is expected when the whole LVL2 tracking chain is performed inside only this reduced RoI. Moreover, this will also reduce the amount of data required to be transfered from the Readout Buffers to the LVL2 processors, hence reducing the overall network traffic with the DAQ system.

2.4 Conclusions and prospects

This study has shown that the performance of the LVL2 tracking can improve significantly both in terms of increased efficiency and in reduced latency, by using an optimized description of the size of RoI. To achieve this, it is necessary to use all the information available from the LVL2 calorimeter reconstruction. By the time these lines were written, work to implement the calculations necessary to obtain this information for LVL2 clusters was underway. Also underway was work to introduce the proposed RoI shape into the RegionSelector, which is the mechanism for providing the detector elements (and thus access to the relevant data) inside a given RoI. This is the way to properly integrate the new RoI shape in the LVL2 trigger software chain.

In order to exploit the full potential of the proposed improvement, it would be interesting to test it using a broader P_T spectrum. Since the electrons used here have essentially the minimum P_T currently required in every trigger menu, the improvements obtained using a full spectrum of momenta might be expected to be similar or even better. Also, samples with more than one electron (for instance for the 2e15i trigger menu) would be important to be studied.

Several improvements might still be envisaged, such as better treatment of the transition region and further optimization of the ρ and z position of the calorimeter samplings in the barrel and endcap regions respectively. It is also possible to study the resolution of the cluster position on the face of the calorimeter, so that the RoI can become narrower while going towards the cluster. All these enhancements might be expected to allow further improvements in the performance of LVL2 tracking, although the bulk of the improvement is achieved with the work presented here.

Part II

The Physics

CHAPTER 3

Vector boson scattering in the Chiral Lagrangian Framework

In this Chapter, the motivation for exploring the scattering processes of vector bosons is discussed. Since it is beyond the scope of this Chapter to address the issue within its full mathematical background, a more descriptive and quantitative way has been chosen instead. Following a short introduction to the Electroweak Symmetry Breaking (EWSB), the theoretical framework of the Electroweak Chiral Lagrangian will be presented, providing at the same time the link to the analysis carried out and which is given in the following Chapters.

3.1 Motivation for studying vector boson scattering at high energies

3.1.1 The problem of the EWSB and the Higgs mechanism

For the past years, the Standard Model (SM) has been a successful theory, since it is in agreement with the recent precision data (see for example [1]). The SM is based on the

$SU(3)_C \bigotimes SU(2)_L \bigotimes U(1)_Y$ gauge symmetry, which provides the basis for describing the electroweak and strong interactions. The requirement of a given Lagrangian to exercise a local gauge invariance under U(1) or SU(3) transformations has led to the well known gauge fields of the photon and the gluons, which are massless, as predicted. But the problem arises when we study SU(2) transformations, simply by the fact that the weakly interacting gauge bosons $W^{\pm}$ and Z are not massless at all.

The SM way to give masses to those particles is to apply the mechanism of the **spontaneous symmetry breaking** to the electroweak interaction. This mechanism is just a way to identify the ground state of the given Lagrangian.

Within the SM, the EWSB is implemented via the **Higgs mechanism**, the formalism of which can be found in many text books (see for example [40]). The result of the Higgs mechanism is that the gauge bosons acquire their masses but also a massive, scalar particle (the so-called **Higgs particle**) is introduced.

3.1.2 The vector boson scattering as a way to probe the EWSB

The formalism of the spontaneous symmetry breaking uncovers from a Lagrangian the hidden mass terms by giving to the ground state (the vacuum) a specific non-zero value. But, according to Goldstone's theorem, any such process is always accompanied by the appearance of one or more massless particles, the Goldstone bosons.

The Higgs mechanism, together with the Higgs particle, produces 3 Goldstone bosons, which eventually, by picking up the correct gauge, are swallowed by the-previously massless- $W^{\pm}$ and Z. Eventually, the vector fields can be polarized not only on the transverse plane, but also they can now have longitudinal polarization. Therefore, since the longitudinal components of the gauge bosons $W^{\pm}$ and Z are really the Goldstone bosons in disguise, the way to probe the EWSB sector is the study of processes which involve the longitudinally polarized modes of these gauge bosons. Things become more clear when we go to energies much greater than their masses where, according to the Equivalence Theorem [41, 42, 43], the $W_L^{\pm}$ and Z_L behave more and more like the original swallowed degrees of freedom.

3.2 The Electroweak Chiral Lagrangian

To explain the origin of EWSB several theoretical models have been proposed in the literature. From a phenomenological point of view, these models can be (roughly) divided into two categories, according to the strength of their interactions: (i) the weakly coupled models, which contain a few light particles below the TeV scale. Typical examples are the Minimal Standard Model with just one doublet of the Higgs boson and the supersymmetric models with more than one doublet, (ii) the strongly coupled models, which are characterized by the absence of light particles. In that case, perturbative calculations are not valid any more and the tree-level amplitude for the scattering of gauge bosons will violate unitarity at the TeV region. To restore the unitarity, specific unitarisation proceedures should be applied, resulting in the appearance of heavy resonances.

The Minimal Standard Model with a heavy Higgs doublet or Technicolor with composite heavy particles are examples of such strongly interacting models [44]. Even though from very general symmetry considerations all of these models share the same dynamics at low energies, their predictions at high energies can vary greatly from one another. The Electroweak Chiral Lagrangian (EWChL) provides a general way to describe those different strongly interacting models as a low energy effective theory without making any assumption about the detailed interactions of the underlying theory.

The EWChL is based on the Chiral Perturbation Theory [45, 46] of low energy pion dynamics in QCD and it is an expansion in derivatives of the Goldstone boson fields. The construction takes into account only symmetry considerations, which are common to any strongly coupled EWSB model.

3.2.1 Formalism

The details of constructing the EWChL can be found in [47, 48]. To obtain the lowest-order term, one can start by requiring that the the most general Lagrangian should employ the spontaneously broken $SU(2)_L \bigotimes U(1)_Y$ symmetry down to $U(1)_{em}$ and therefore it should involve three Goldstone bosons. The building block of the chiral Lagrangian is the matrix field:

$$U = exp\left(i\frac{\omega^{\alpha}\tau^{\alpha}}{u_v}\right) \tag{3.1}$$

where τ^{α} ($\alpha = 1, 2, 3$) are the Pauli matrices, ω are the three Goldstone bosons and $u_v \simeq 246$ GeV is the vacuum expectation value of the Higgs field[1].

The second requirement is set by the fact that the system presents a global chiral $SU(2)_L \bigotimes SU(2)_R$ symmetry that is broken to $SU(2)_L$. This residual symmetry is responsible for ensuring the masses of the gauge bosons (custodial symmetry) satisfy the equation $M_W^2 = M_Z^2 \cos^2\theta_W$ [2]. The only remaining term of order-2 is:

$$\mathcal{L}^{(2)} = \frac{u_v^2}{4} Tr\{D_{\mu}UD^{\mu}U^{\dagger}\} \tag{3.2}$$

and the $SU(2)_L \bigotimes U(1)_Y$ covariant derivative of U is defined as:

$$D_{\mu}U \equiv \partial_{\mu}U + ig\frac{\tau^{\alpha}}{2}W_{\mu}^{\alpha}U - ig'U\frac{\tau^3}{2}B_{\mu} \tag{3.3}$$

At the next order in the derivative expansion (p^4 or equivalently $\hat{s}^2$), there are many operators of dimension-4. But, in order to describe genuine vector boson interactions, one should focus on pure quartic vertices, ignoring diagrams which include anomalous triple gauge-boson vertices. With this consideration, the EWChL is expressed by the following equation:

$$\mathcal{L}_{EWChL} = \mathcal{L}^{(2)} + \mathcal{L}^{(4)} + ... = \frac{u^2}{4}Tr\{D_{\mu}UD^{\mu}U^{\dagger}\} + \alpha_4\left(Tr\{D_{\mu}UD^{\mu}U^{\dagger}\}\right)^2 + \alpha_5\left(Tr\{D_{\mu}UD^{\nu}U^{\dagger}\}\right)^2 \tag{3.4}$$

The dependence on the underlying model is introduced via the dimensionless parameters α_4 and α_5: different choices of the value and the sign of those parameters would correspond to different models of the strongly interacting electroweak symmetry breaking sector. Moreover, in the case that the scattering amplitudes ought to be calculated at

---

[1] The vacuum expectation value of the Higgs field is related to the Fermi constant G_F: $u_v^2 = \frac{1}{\sqrt{2}G_F}$

[2] This argument is explored usually by defining the parameter ρ as $\rho = M_W^2/M_Z^2 cos^2\theta_W$.

the order of $\hat{s}^2$, one should also include one-loop correction to the $\mathcal{L}^{(2)}$ term, since those are of the same order. The main effect when doing so, is to introduce a scale dependence of the chiral couplings α_4, α_5 so they actually become $\alpha_4(\mu)$, $\alpha_5(\mu)$, where μ is the renormalization scale. A detailed discussion is given in [47]. It is important to mention that the values of the parameters can be constrained by fits to the electroweak precision data and, for this analysis, they are considered to vary in the range [-0.01, 0.01] [49].

3.2.2 Scattering amplitudes

Since we have an $SU(2)_{L+R}$ symmetry, it is convenient to work within the weak isospin space. The scattering amplitude can be written as:

$$\mathcal{M}(V_L^a V_L^b \rightarrow V_L^c V_L^d) \equiv A(s,t,u)\delta^{ab}\delta^{cd} + A(t,s,u)\delta^{ac}\delta^{bd} + A(u,t,s)\delta^{ad}\delta^{bc} \tag{3.5}$$

where $V_L^i = W_L^+, W_L^-, Z_L$ and:

$$\begin{aligned} W_L^{\pm} &= \frac{1}{\sqrt{2}}(W_L^1 \mp iW_L^2) && (3.6)\\ Z_L &= W_L^3 && (3.7) \end{aligned}$$

The quantities s, t, u are the usual Mandelstam kinematical variables and the indices a,b,c are the weak isospin indices with values 1,2,3. Equation 3.5 can describe the dynamics of any vector boson scattering process [50]. For example, for the $W_L^{\pm}W_L^{\pm}$ scattering, this becomes:

$$\mathcal{M}(W_L^{\pm}W_L^{\pm} \rightarrow W_L^{\pm}W_L^{\pm}) = A(t,s,u) + A(u,t,s) \tag{3.8}$$

The function $A(s,t,u)$ is calculated up to the order of s^2 and is given by the expression:

$$\begin{aligned} A(s,t,u) = {} & \frac{s}{u^2} + \frac{1}{4\pi u^4}\left(2\alpha_4(\mu)s^2 + \alpha_5(\mu)(t^2+u^2)\right) + \\ & + \frac{1}{16\pi^2 u^4}\left(-\frac{t}{6}(s+2t)\log\left(-\frac{t}{\mu^2}\right)\right) - \\ & - \frac{1}{16\pi^2 u^4}\left(\frac{u}{6}(s+2u)\log\left(-\frac{u}{\mu^2}\right) - \frac{s^2}{2}\log\left(-\frac{s}{\mu^2}\right)\right) \end{aligned} \tag{3.9}$$

3.3 Unitarisation of the Electroweak Chiral Lagrangian

The EWChL, as it has been presented so far, is an effective low-energy approach, which demonstrates a major problem: the scattering amplitudes violate unitarity for vector bosons' invariant masses around 1-2 TeV. The standard treatment to overcome this obstacle is the unitarisation of the scattering amplitudes, using a specific unitarisation protocol. Most commonly, the **Padé** (or **Inverse Amplitude**) [51] and the **N/D** [52] protocols have been used in the literature. The formalism of these unitarisation protocols is beyond the studies of this Thesis, but a detailed description and comparison between those two approaches is given in [53].

3.3.1 Resonance scenarios

An important result of the unitarisation procedure is that the final, unitarised scattering amplitudes can reproduce a resonant behavior. The mass and the type of the resulting resonances depend on the values of the effective couplings α_4, α_5, but also on the applied unitarisation protocol. For the analysis presented here, the Padé protocol was used, which predicts the following mass and width for a scalar (spin-0) resonance:

$$M_S^2 = \frac{12u_v^2}{16[11\alpha_5(\mu) + 7\alpha_4(\mu)] + \frac{101-50\log(M_S^2/\mu^2)}{48\pi^2}}, \qquad \Gamma_S = \frac{M_S^3}{16\pi u_v^2} \tag{3.10}$$

and

$$M_V^2 = \frac{u_v^2}{4[\alpha_4(\mu) - 2\alpha_5(\mu)] + \frac{1}{144\pi^2}}, \qquad \Gamma_V = \frac{M_V^3}{96\pi u_v^2} \tag{3.11}$$

for a vector (spin-1) resonance.

By fixing the renormalisation scale to the value $\mu = 1$ TeV, we construct the $\alpha_4 - \alpha_5$ parameter space illustrated in Figure 3.1. We notice that certain combinations of the chiral parameters are excluded theoretically [54]. Any straight line which is drawn parallel to the blue or to the red lines would correspond to resonances of equal masses. Points which lie at the region from the red line and upwards right will correspond to scalar resonances, whereas points inside the region from the blue line and upwards left will result in vector

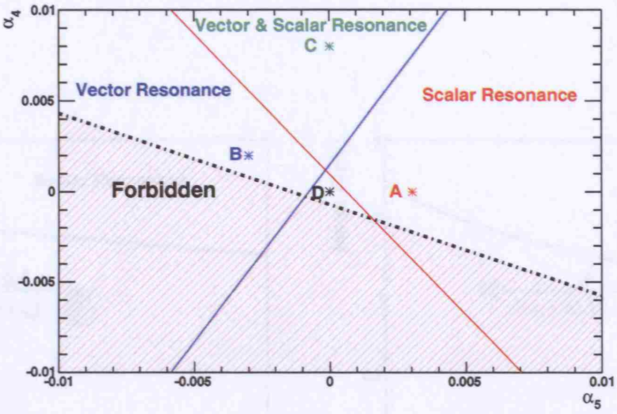

Figure 3.1: The $\alpha_4 - \alpha_5$ parameter space as predicted using the Padé protocol. From [53].

resonances. Point A is an example of a scalar resonance of mass ~1 TeV and point B is an example of a vector resonance with mass of ~ 1.4 TeV. There is also a common area between these two regions, where one can find both a scalar and a vector resonance. Point C is an example of this scenario. Finally, there is an interesting region, where no resonances will be produced (Point D). In that case, the invariant mass of the vector bosons will have a continuum spectrum. The values of the α_4, α_5 parameters for the four example scenarios are summarized in Table 3.1. Figure 3.2 shows the dependence of the resonance mass on the combination of the chiral parameters.

In order to study those different scenarios, the PYTHIA Monte Carlo generator [55] has been modified to include the EWChL approach. The parton-level predictions for the differential cross-section are given in Figure 3.3 for the process $pp \rightarrow W^+W^-qq + X$, where one of the bosons decays leptonically and the other decays hadronically.

Scenario	α_4	α_5	Resonance Mass (GeV)
Scalar(A)	0.0	0.003	989.8
Vector(B)	0.002	-0.003	1360.3
Scalar + Vector (C)	0.008	0.0	809.6 + 1360.3
Continuum (D)	0.0	0.0	NA

Table 3.1: Values of the α_4 and α_5 parameters and the mass of the predicted resonance for the A, B, C and D scenarios. The values have been calculated at $\mu = 1$ TeV.

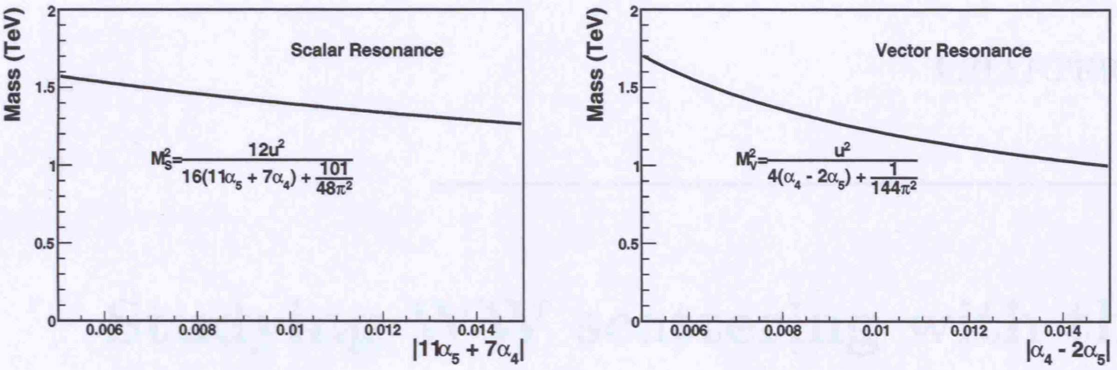

Figure 3.2: Dependence of the mass of the resonance (scalar or vector) on the combination of the α_4, α_5 parameters.

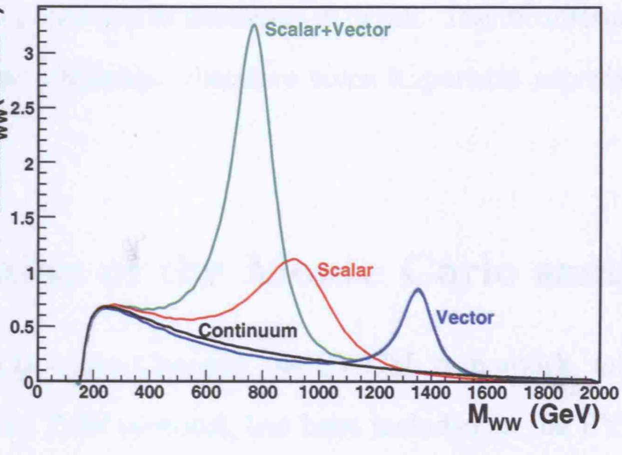

Figure 3.3: The differential cross section for the process $W^{\pm}W^{\pm} \rightarrow W^{\pm}W^{\pm}$ as a function of the WW mass for the A, B, C and D scenarios.

CHAPTER 4

Studying WW scattering with the ATLAS Detector

The aim of this Chapter is to present the tools for the generation and the simulation of the data samples, defining at the same time the signal and the background processes. Since we will use W bosons, which decay into leptons and hadrons, the methodology for reconstructing those bosons will be described in detail. The reconstruction of a hadronically decaying W is a great challenge, therefore some important aspects of this issue will be discussed.

4.1 Generation of the Monte Carlo samples

As mentioned in the previous Chapter, the EWChL framework, followed by the unitarisation according to the Padé protocol, has been included in the PYTHIA (version 6.226) event generator.

A typical diagram of a vector boson scattering is given in Figure 4.1. By controlling the chiral parameters α_4 and α_5, 600,000 WW scattering events of the A,B,C and D scenarios have been generated for each one. The scattering of the vector bosons includes any charge combination and all the possible decays of the W boson are allowed.[1] For the following, we focused of the events where one of the Ws decays leptonically and the other hadronically.

The dominant backgrounds are the QCD $t\bar{t}$ and W+jets production, where the jets fake the hadronically decaying W.

The corresponding diagrams are given in Figure 4.1. In order to improve the generation efficiency, the minimum transverse momentum of the hard scatter has been set to 300 GeV for the $t\bar{t}$ process and to 250 GeV for the W+jets.

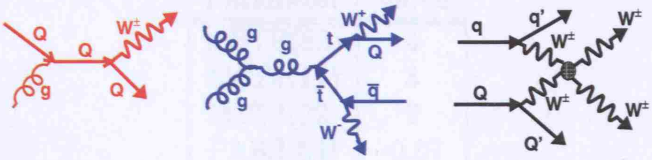

Figure 4.1: Typical diagrams for the W+jets (red) and $t\bar{t}$ (blue) production and for the WW scattering (black). The production of the $t\bar{t}$ pair via the gluon-gluon fusion dominates the production via quark-quark annihilation.

The cross sections for each of the signal scenarios and the background processes are given in Table 4.1. We notice that the W+jets is the dominant background with 4 times higher event rate than the $t\bar{t}$ process. The cross sections have been obtained by using the Leading Order (LO) calculations of the generator. More accurate calculations, at the Next-to-Leading Order (NLO), are expected to affect the processes, which involve gluons and the $t\bar{t}$ production via the gluon fusion has the largest uncertainty. Even though the quality of our modeling of this effect, as it is implemented in the generator will be tested against the collected data, estimations give a K-factor [2] in the range from 1.5 up to 2.0 (see for example [57]).

Finally, while almost all of the PYTHIA parameters were set to their default values, a set of parameters, controlling mainly the Underlying Event model, have been modified in accordance with the settings adopted by the ATLAS Collaboration (Rome Tuning [58]). These parameters, together with their values, are listed in Table 4.2.

---

[1] The branching ratio for the leptonic decay of the W boson ($W \to \ell\nu$, $\ell = e, \mu, \tau$) is $(10.80 \pm 0.09)\%$, where for the hadronic decay ($W \to q\bar{q}$) is $(67.60 \pm 0.27)\%$ [56].

[2] The K-factor is defined as the ratio $\frac{\sigma_{NLO}}{\sigma_{LO}}$.

Process	σ (fb)
Scalar Signal (A)	74.9
Vector Signal (B)	52.4
Scalar + Vector Signal(C)	118.2
Continuum Signal(D)	44.0
$t\bar{t}$ Background	15640
W+jets Background	62600

Table 4.1: Cross-sections for the signal and background processes obtained from PYTHIA within the EWChL framework. For the signals, the values for α_4 and α_5 are those given in Table 3.1.

Parameter	Value
MSTP(82)	4
MSTJ(11)	3
MSTJ(22)	2
PARJ(54)	-0.07
PARJ(55)	-0.006
PARP(82)	1.8
PARP(84)	0.5

Table 4.2: Values of the PYTHIA input parameters according to the Rome-tuning [58].

4.2 Simulation and Reconstruction

The generated events were simulated and reconstructed in a single step, using the fast simulation package for the ATLAS detector, ATLFAST [59]. ATLFAST parametrises the response of the detector according to studies done by the full simulation. It is an intermediate level between the simple, but often misleading parton-level analysis and the very sophisticated but time and CPU consuming full detector simulation. The results from ATLFAST have been validated in the past using specific physics channels, but a big effort is currently under way to evaluate its performance against the latest fully simulated samples [60].

ATLFAST starts from the generated event. By assuming a homogeneous, solenoidal magnetic field of 2 T, all the stable, charged particles which have $P_T > 0.5$ GeV are extrapolated to the entrance of the Calorimeter. It is assumed that there is no separation between the EM and the Hadronic Calorimeters and no simulation of the Inner Detector or the Muon Spectrometer is performed. Also, the particles do not interact with any material and the Bremsstrahlung (for electrons) or pair production (for photon) effects are not simulated. This means that all the particles reach the calorimeter having their initial energies. The following physics objects are then constructed:

- **ATLFAST Calorimeter clusters:** The Calorimeter is divided into cells of dimensions $\Delta\eta \times \Delta\phi = 0.1 \times 0.1$, for $0 \leq |\eta| < 3.2$ and $\Delta\eta \times \Delta\phi = 0.2 \times 0.2$, for $3.2 \leq |\eta| < 5$. Each of the particles deposits its energy inside the associated cell.

  For a simple cone-type algorithm, each cell with $E_T > 1.5$ GeV (initiator) is scanned to verify whether the total E_T summed over all cells inside a cone $\Delta R = 0.4$ exceeds the minimum required threshold for a reconstructed cluster (typically $E_T^{min} = 5$ GeV). If so, those cells are grouped into a cluster, the coordinates of which are taken to be the coordinates of the barycenter.

- **ATLFAST Electrons:** Each true electron is selected according to selection criteria (typically $P_T > 5$ GeV and $|\eta| < 2.5$) and a reconstructed cluster within a distance $\Delta R_{e-cluster} < 0.15$ is searched to associate with the true electron. In order for a cluster to be identified as an electron, isolation criteria are applied. These include the distance from other clusters (typically $\Delta R > 0.4$) and the total transverse energy deposited in a cone around the cluster axis (typically, it is required that $\sum E_T < 10$ GeV of all the un-clustered cells inside a cone of $\Delta R = 0.2$ around the cluster axis). If a cluster is taken to come from an electron, the particle's four-vector is smeared according the resolution function (all the smearing functions can be found in Appendix C).

  It is important to stress the fact that ATLFAST does not take into account efficiencies for identifying electrons (that is assumed to be 100%) or misidentifying jets as electrons (it is assumed 0%). This is also the case for the photon and muon reconstruction.

- **ATLFAST Photons:** The photons are reconstructed by applying the same selection and isolation criteria as for the electrons. The photon's four-vector is smeared using again a resolution function.

- **ATLFAST Muons:** For the muons, similar selection and isolation cuts are applied. The interesting point is that the energy is smeared according to a resolution which depends on the muon P_T, $|\eta|$ and ϕ. Also, there are three different resolution functions, depending on which sub-detectors are assumed to be used for the muon reconstruction: the stand alone Muon Spectrometer, the stand alone Inner Detector or the combination of the two systems.

- **ATLFAST Jets:** All the clusters which have not been associated with isolated electrons, photons or muons are used to reconstruct the jets. At first stage, their energies are smeared according to a resolution function. Furthermore, the energy of the non-isolated muons which are found inside the cluster cone is added to the smeared energy of that cluster. If the resulting jet passes the selection criteria (normally $E_T > 10$ GeV and $|\eta| < 5.0$), then it is labeled as a reconstructed jet.

  ATLFAST also performs the jet tagging for tau-jets, b-jets or c-jets using the specialized package ATLFAST-B. The technique for doing so is analytically explained in [59] and since the current analysis does not require any jet-tagging information, details are not given. It is essential to mention though that, during the jet-labeling procedure, efficiencies for jet identification or jet misidentification are taken into account for all the types of jets, parametrised as a function of their P_T.

- **ATLFAST $\mathbf{E_T^{miss}}$:** By summing up the transverse momenta of the identified isolated electrons, photons and muons, the jets, the remaining clusters (not identified as jets) and of the no-isolated muons which were not used in any jet cluster, the E_T^{obs} is calculated. In this quantity, the transverse energies of all the cells not used in clusters are added, after smearing with the resolution function. The missing transverse energy is $E_T^{miss} = E_T^{obs}$ and its components are given by the relations: $P_x^{miss} = -P_x^{obs}$ and $P_y^{miss} = -P_y^{obs}$.

  ATLFAST uses parametrisations for both the low and high luminosity scenarios. For the current studies, all of the ATLFAST parameters were used with their default values for low luminosity.

4.3 Event Reconstruction

The following sections describe the methodology for reconstructing the physical objects. In our case, since we are interested in the events where one W decays leptonically and the other hadronically, we will try to reconstruct the leptonically decaying W ($\mathrm{W^{lept}}$) and the hadronically decaying W ($\mathrm{W^{had}}$). The WW system is simply reconstructed by adding the Lorentz vectors of $\mathrm{W^{lept}}$ and $\mathrm{W^{had}}$:

$$WW_{\mu} = W_{\mu}^{lept} + W_{\mu}^{had} \tag{4.1}$$

Concerning the triggering of the signal events, that will not be an issue, since, as it will be described in the following sections, we will require final state objects with energies far more greater than those set by the triggering menus.

Finally, for the Signal, the Continuum scenario was used as a case study.

4.3.1 Reconstruction of the Leptonic W

The leptonic W is reconstructed using the leading lepton (electron or muon) and the $\mathrm{E_T^{miss}}$ of the event. The $\mathrm{E_T^{miss}}$ accounts for the neutrino in the decay channel and since the z-component of its momentum is unknown, only the transverse parameters of the $\mathrm{W^{lept}}$ can be calculated directly. To overcome this problem, the neutrino's P_z can be calculated by fixing the mass of $\mathrm{W^{lept}}$ and using the equation:

$$M_W^2 = \left(E^{lept} + \sqrt{P_T^{\nu 2} + P_z^{\nu 2}}\right)^2 - \left(P_x^{lept} + P_x^{\nu}\right)^2 - \left(P_y^{lept} + P_y^{\nu}\right)^2 - \left(P_z^{lept} + P_z^{\nu}\right)^2 \tag{4.2}$$

The mass of the $\mathrm{W^{lept}}$ has been set to 80.4 GeV and the algebraic solution of the above equation is derived in the Appendix B.

Since it is a quadratic equation in P_z, two possible solutions are foreseen. In that case, two possible $\mathrm{W}^{\mathrm{lept}}$ can be constructed with the same P_T and mass, but different P_z. Figure 4.2 gives the distance in the $\eta-\phi$ space between the true $\mathrm{W}^{\mathrm{lept}}$ and the reconstructed $\mathrm{W}^{\mathrm{lept}}$ in the case of using the solution with the minimum $|P_z|$ (W^{lept}_{slow}) or with the maximum P_z (W^{lept}_{fast}). Most of the times, the W^{lept}_{slow} is closer to the true $\mathrm{W}^{\mathrm{lept}}$. Since there are no physical reasons to predict the best reconstructed solution, based purely on this statistical argument, the $\mathrm{W}^{\mathrm{lept}}$ with the minimum P_z is used.

Events which don't have any isolated reconstructed leptons (~62% of the generated events) or for which there is not a neutrino solution (~10% of the generated events) are rejected.

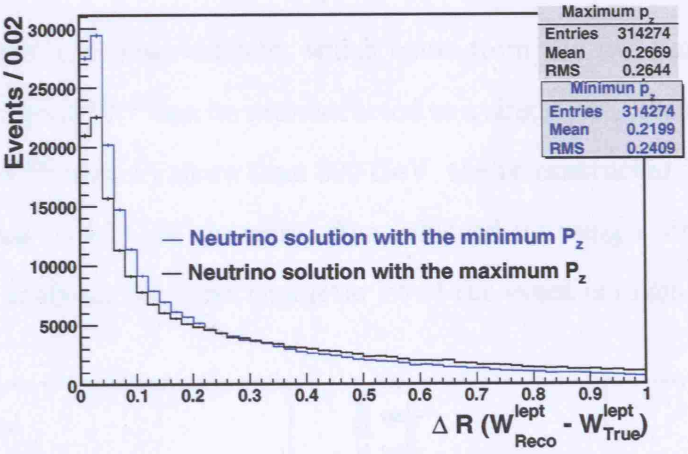

Figure 4.2: Distance in the $\eta-\phi$ space between the true and the reconstructed $\mathrm{W}^{\mathrm{lept}}$ for the two neutrino solutions.

4.3.2 Reconstruction of the Hadronic W

To reconstruct the hadronic W, we notice that, for a highly boosted W, the quarks from its decay will be very close to each other. This is demonstrated by the left histogram in Figure 4.3, which gives the distance ΔR in $\eta-\phi$ space between the emerged quarks and the P_T of the W that they originated from. As the W becomes more boosted, the distance between the quarks becomes smaller. For very energetic bosons (transverse momentum more than 300 GeV), the distance of the two partons is given on the right histogram of Figure 4.3.

The mean value is close to 0.5 and the most probable value can be found around 0.4.

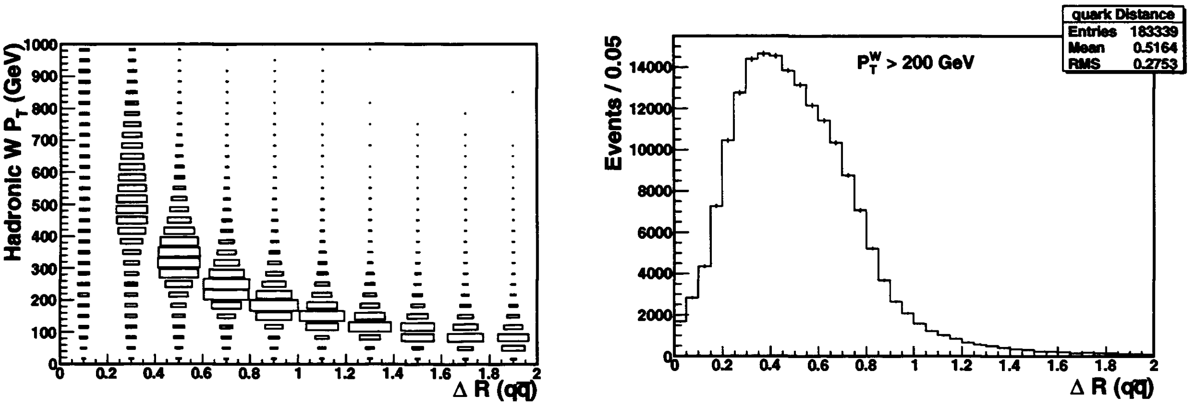

Figure 4.3: Left: Distance in the $\eta - \phi$ space between the quarks that originate from a W versus the the P_T of the W. Right: Distribution of the distance between quarks emerging from a highly boosted W.

As a consequence, the observed jets, which come from the two partons, will overlap. Therefore, very energetic W^{had}can be reconstructed as a single jet[3]. This is demonstrated in Figure 4.4. For a W^{had} with P_T more than 300 GeV, the reconstructed W with mass closer to the nominal mass ($\sim$ 80 GeV) is more often achieved by using a single jet. Therefore, for the rest of the analysis, the most energetic jet of the event is taken to be the W^{had} .

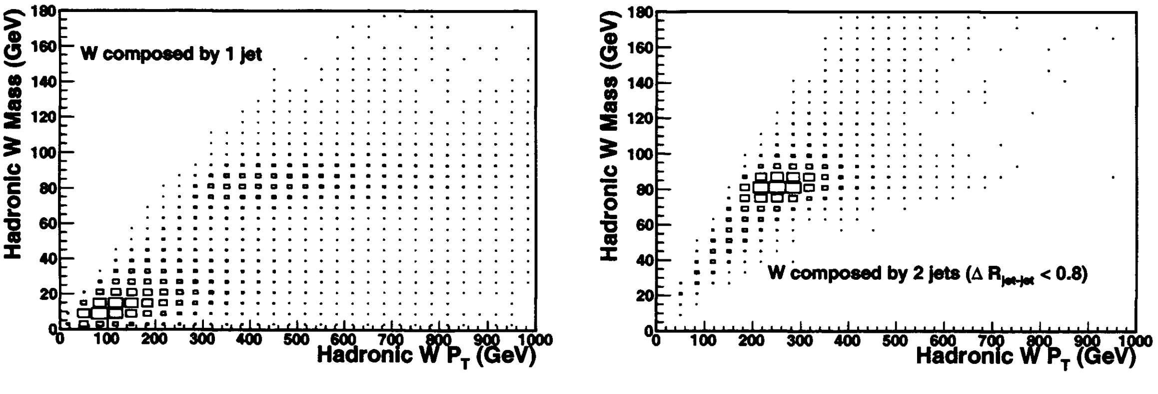

Figure 4.4: The reconstructed mass of the hadronic W versus its reconstructed P_T, when the W is reconstructed by a single jet (left histogram) or by two jets (right histogram).

---

[3] The jets were reconstructed using the $k_\perp$ algorithm, as it will be discussed later.

Hadronic W reconstruction with the $k_\perp$ algorithm

At present, there are essentially two classes of jet algorithms: (i) the cone-type algorithms, where jets are defined by maximizing the amount of energy which can be covered by cones of fixed size and (ii) the clustering algorithms, where the final state particles are grouped together into jets where a given energy-angle resolution variable exceeds a fixed resolution parameter.

Regarding the first class, the jet clustering using the Cone algorithm has been extensively studied [61] and it was found that the best $\mathrm{W}^{\mathrm{had}}$ reconstruction as a single jet is achieved using a cone radius of 0.7.

For the current analysis the $k_\perp$ algorithm [62, 63], which is a representative example of the second class of jet algorithms, has been used throughout and a generic introduction to its formalism is presented in Appendix D. The major motivation for doing so was the fact that one can apply the algorithm on a single jet and, once the constituents of the jet are available, its structure can be investigated. This procedure (called sub-jet analysis) is particularly useful in our case, where the $\mathrm{W}^{\mathrm{had}}$ is reconstructed as one single jet, since one could look inside that jet and find the original two jets, which came from the W decay. Another advantage of the $k_\perp$ approach is the feature that it is invariant under boosts along the W direction and this is important, when one wants to study the shape of a quantity (like a cross-section, as it will be discussed later) as a function of the WW centre-of-mass energy. This feature does not appear in the simple cone algorithms, in which case the applied cone radius should be dependent on the P_T of the W.

With the leading jet of the event, the sub-jet analysis, as it is analytically explained in [63], was carried out: requiring n+1 jets to merge to n, a resolving parameter $y_{n+1,n}$ can be calculated. For our case, the resolving parameter y_{21} was used and for convenience, we define the quantity:

$$Y \text{ scale} \equiv \log\left(P_T^{HadW} \times \sqrt{y_{21}}\right) \tag{4.3}$$

Given the way in which the resolving parameter y_{21} is defined and due to the fact that the parameters are defined in the centre-of-mass frame of the hadronic W, the Y-scale is expected to be at the order of $\log(M_W)$, for a highly boosted genuine decaying W. This distribution is given in Figure 4.5 for both the signal and the background processes. For the signal and the $t\bar{t}$ samples, where there is a genuine $\mathrm{W^{had}}$, the distribution gives a peak around 1.8, which is not the case for the W+jets sample, where the jets fake the $\mathrm{W^{had}}$.

This distribution will be later shown to be a strong cut for rejecting the bulk of the W+jets events.

The $k_\perp$ algorithm depends on a parameter R, which is analogous to the cone size parameter in the Cone algorithm. To decide upon the optimum value, the algorithm was used with five different R-parameters: 0.2, 0.4, 0.5, 0.8 and 1.2. The effect on the mass of the reconstructed $\mathrm{W^{had}}$ is shown in Figure 4.6. As the R-parameter increases, the peak moves towards high masses and with R=1.2 an asymmetric tail appears. This is caused by adding to the leading jet other jets, not associated with the hard scatter process. With R=0.2 and with small values in general, a second peak at low masses emerges, due to the fact that the $\mathrm{W^{had}}$ is resolved into two jets, therefore it cannot be reconstructed by a single one. The best resolution of the mass is achieved using R-parameter=0.5, which is the value used for the rest of the analysis. The distribution of the mass, after imposing a cut on the Y-scale, is shown on the right histogram of Figure 4.6. A fit with a gaussian function in the range 70 GeV - 95 GeV gives a resolution σ = 7.16 GeV, which will be used later for selecting the $\mathrm{W^{had}}$ candidates. The mean value is shifted approximately 4 GeV with respect to the nominal mass of the W, but this doesn't cause any problems, since an offline jet calibration will bring the distribution at the correct position.

4.3.3 Selection criteria

In order to estimate whether and to what extent it is possible to see the different strongly interacting processes over the expected backgrounds, we first apply initial selection cuts on both the leptonic and hadronic W distributions. The order in which the cuts are applied is given by the sequence they are presented.

Figure 4.7 gives the distributions of the P_T and η of the leading lepton in the event, expected to be at the order of $\log(M_W)$, for a highly boosted genuine decaying W. This distribution is given in Figure 4.5 for both the signal and the background processes. For the signal and the $t\bar{t}$ samples, where there is a genuine W^{had}, the distribution gives a peak around 1.8, which is not the case for the W+jets sample, where the jets fake the W^{had}.

This distribution will be later shown to be a strong cut for rejecting the bulk of the W+jets events.

The $k_\perp$ algorithm depends on a parameter R, which is analogous to the cone size parameter in the Cone algorithm. To decide upon the optimum value, the algorithm was used with five different R-parameters: 0.2, 0.4, 0.5, 0.8 and 1.2. The effect on the mass of the reconstructed W^{had} is shown in Figure 4.6. As the R-parameter increases, the peak moves towards high masses and with R=1.2 an asymmetric tail appears. This is caused by adding to the leading jet other jets, not associated with the hard scatter process. With R=0.2 and with small values in general, a second peak at low masses emerges, due to the fact that the W^{had} is resolved into two jets, therefore it cannot be reconstructed by a single one. The best resolution of the mass is achieved using R-parameter=0.5, which is the value used for the rest of the analysis. The distribution of the mass, after imposing a cut on the Y-scale, is shown on the right histogram of Figure 4.6. A fit with a gaussian function in the range 70 GeV - 95 GeV gives a resolution $\sigma = 7.16$ GeV, which will be used later for selecting the W^{had} candidates. The mean value is shifted approximately 4 GeV with respect to the nominal mass of the W, but this doesn't cause any problems, since an offline jet calibration will bring the distribution at the correct position.

4.3.3 Selection criteria

In order to estimate whether and to what extent it is possible to see the different strongly interacting processes over the expected backgrounds, we first apply initial selection cuts on both the leptonic and hadronic W distributions. The order in which the cuts are applied is given by the sequence they are presented.

Figure 4.7 gives the distributions of the P_T and η of the leading lepton in the event,

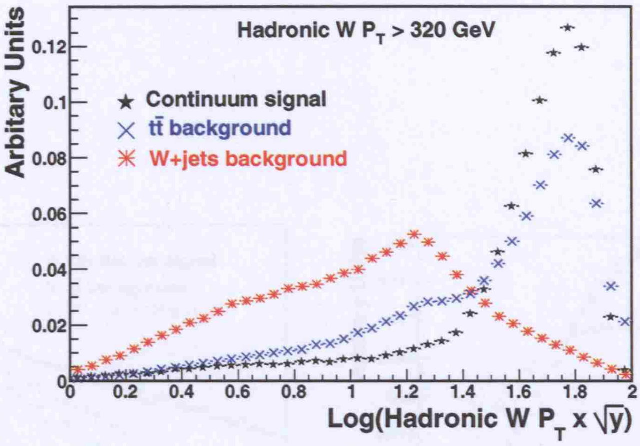

Figure 4.5: The quantity Y-scale≡ $\log\left(P_T^{HadW} \times \sqrt{y_{21}}\right)$ for the signal and the background processes. The histograms are normalized to unit area.

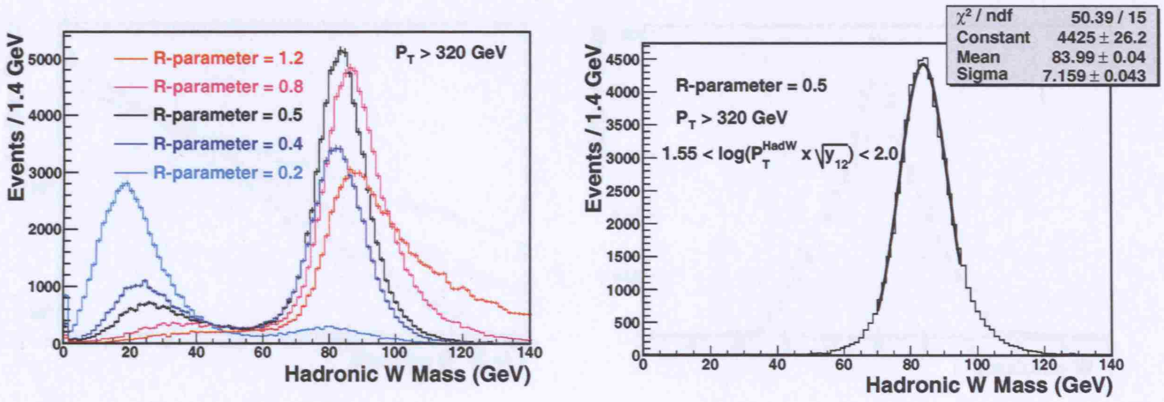

Figure 4.6: Left: Reconstructed mass of the $\mathrm{W}^{\mathrm{had}}$ from a single jet using different sizes of the $k_{\perp}$ algorithm. Right: Reconstructed mass of the $\mathrm{W}^{\mathrm{had}}$ using $k_{\perp}$ R-parameter=0.5. The fit is done with a gaussian function in the range of 70 GeV-95 GeV.

the $\mathrm{E}_{\mathrm{T}}^{\mathrm{miss}}$ and the P_T distribution for the finally reconstructed $\mathrm{W}^{\mathrm{lept}}$ for both the signal and background samples. Since we are interested in the relative shape of the distributions, each of the histograms has been normalized to its area.

For the signal and the $t\bar{t}$ background, the lepton is distributed mainly in the central region of the detector, whereas the W+jets sample gives a lepton which is distributed over a larger area of the detector. The $\mathrm{W}^{\mathrm{lept}}$, for all the cases, is found predominately in the central region and the signal process gives harder P_T spectrum than the background ones.

For an event to be processed, the reconstructed $\mathrm{W}^{\mathrm{lept}}$ is required to have $P_T > 320$ GeV.

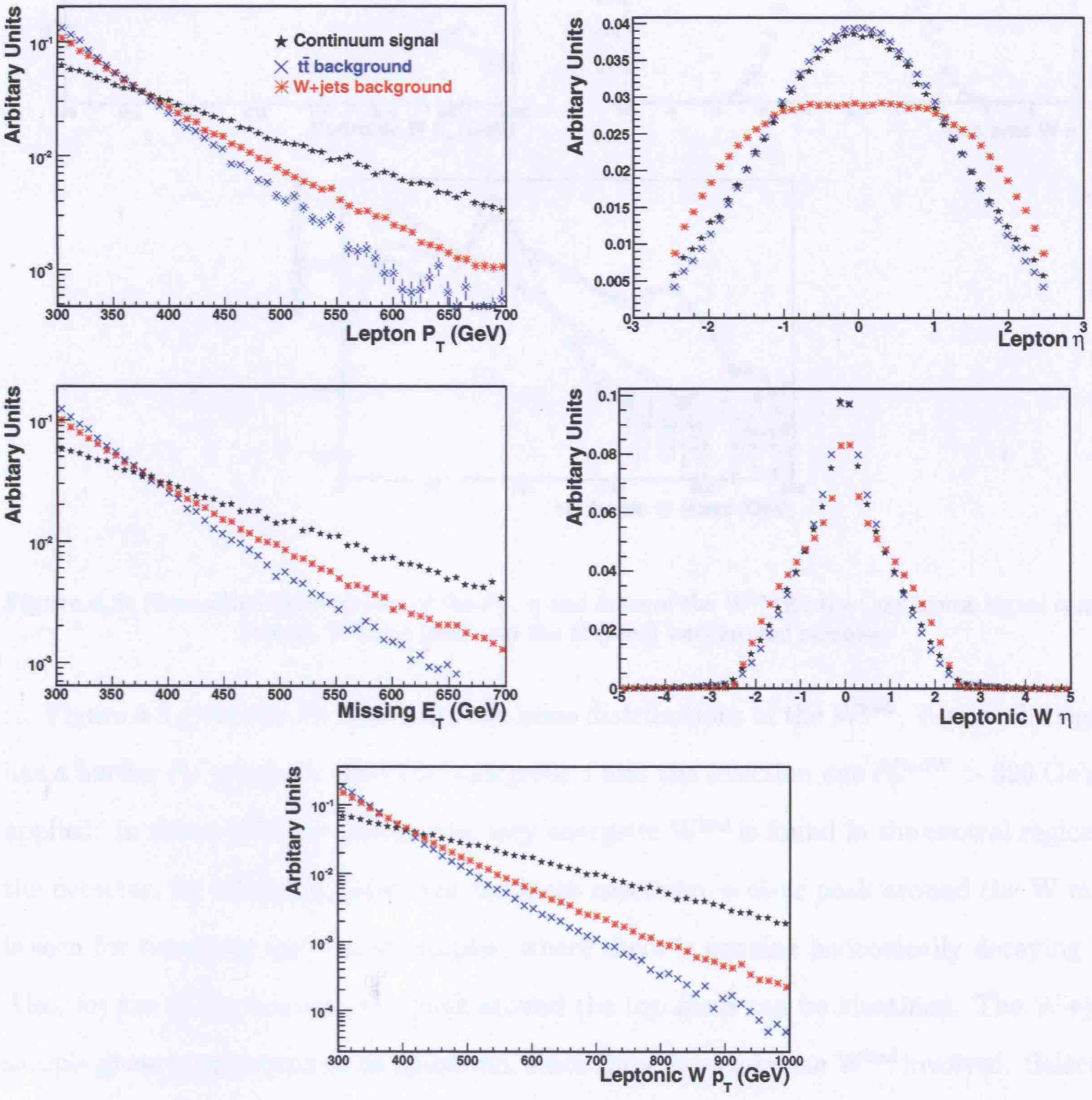

Figure 4.7: Normalized distributions of the leading lepton, the E_T^{miss} and the W^{lept} for the Continuum signal sample (black), W+jets (red) and the $t\bar{t}$ (blue) background samples.

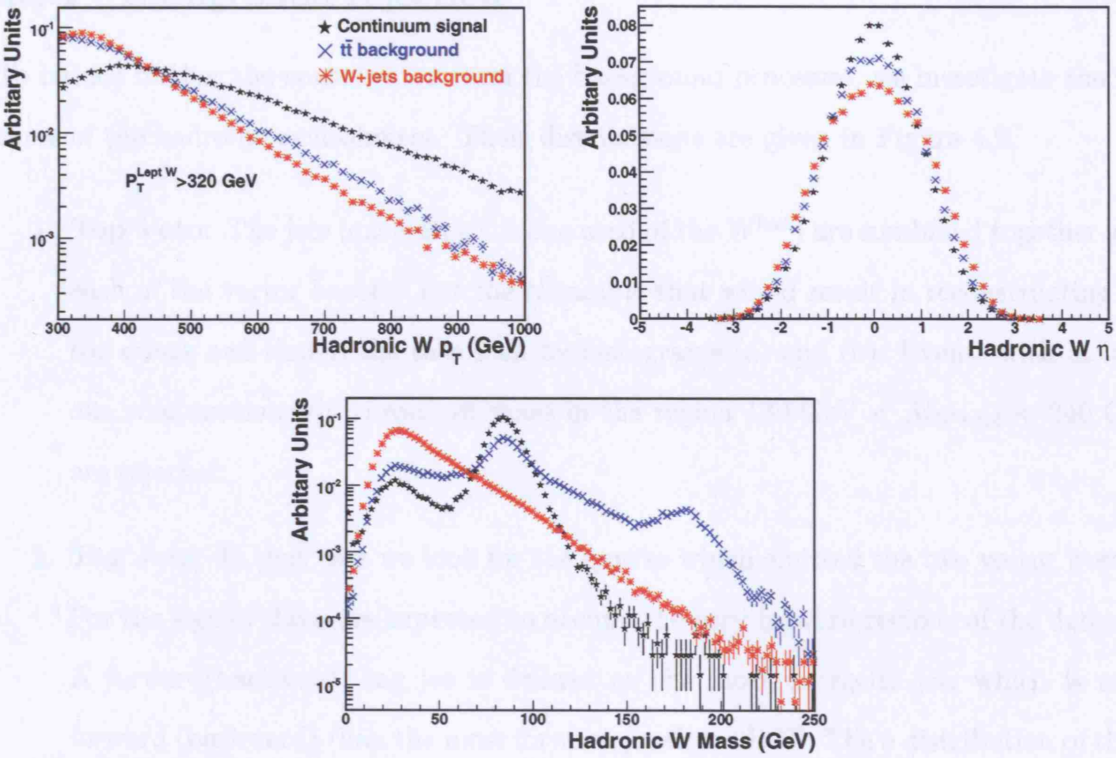

Figure 4.8: Normalized distributions of the P_T, η and mass of the $\mathrm{W^{had}}$ for the Continuum signal sample (black), W+jets (red) and the $t\bar{t}$ (blue) background samples.

Figure 4.8 gives the P_T, the η and the mass distributions of the $\mathrm{W^{had}}$. Again, the signal has a harder P_T spectrum than the background and the selection cut $P_T^{\mathrm{HadW}} > 320$ GeV is applied. In terms of the geometry, the very energetic $\mathrm{W^{had}}$ is found in the central region of the detector, for all the samples. For the mass spectrum, a clear peak around the W mass is seen for the signal and the $t\bar{t}$ samples, where there is genuine hadronically decaying W. Also, for the $t\bar{t}$ distribution, the peak around the top mass can be identified. The W+jets sample gives a continuum mass spectrum, since there is no genuine $\mathrm{W^{had}}$ involved. Selected events were those which give mass in the range $\pm 2.5\sigma$ around the mean reconstructed mass, as taken from the gaussian fit of the distribution in Figure 4.6 ($\sigma = 7.16$ GeV, $\mu = 83.99$ GeV).

The last selection cut is applied on quantity Y-scale, which was defined in Section 4.3.2 and it is plotted in Figure 4.5. Selected events where those which give 1.55 <Y-scale< 2.0.

4.3.4 Background rejection

To reduce further the contribution from the background processes, we investigate the features of the hadronic environment. Their distributions are given in Figure 4.9.

1. **Top Veto:** The jets (excluding the one used of the W^{had}) are combined together with each of the vector bosons. For the $t\bar{t}$ sample that would result in reconstructing the top quark and that is the case seen by histograms (a) and (b). Events with at least one combination with invariant mass in the region 130 GeV $< M_{W+jet} <$ 240 GeV are rejected.

2. **Tag Jets:** In that case we look for the quarks which emitted the two vector bosons. For the signal, these are expected to occupy the very forward regions of the detector. A forward(backward) tag jet is defined as the most energetic jet, which is more forward (backward) than the most forward (backward) W. The η distribution of those jets is given by histogram (c). Accepted events are those which have at least one tag jet (both forward and backward) with P_T more than 20 GeV and $E >$ 300 GeV in the region $2.0 < |\eta| < 4.5$.

3. **Hard P_T:** For the signal process, the system of the two tag jets combined with the two vector bosons should not have transverse momentum, as can be seen from Figure 4.1. The P_T distribution of the system is given by histogram (d). Events with $P_T >$50 GeV are rejected.

4. **Mini-jet veto:** The mini-jets are defined as all the jets with $P_T >$15 GeV inside the region $|\eta| < 2.0$. Since there is no color exchange between the quarks which emitted the W bosons and the bosons themselves, signal processes are expected to give no mini-jets. The distribution of the number of mini-jets is given by histogram (e). Events which have mini-jets are rejected.

Table 4.3 summarises all the selection cuts and theirs values.

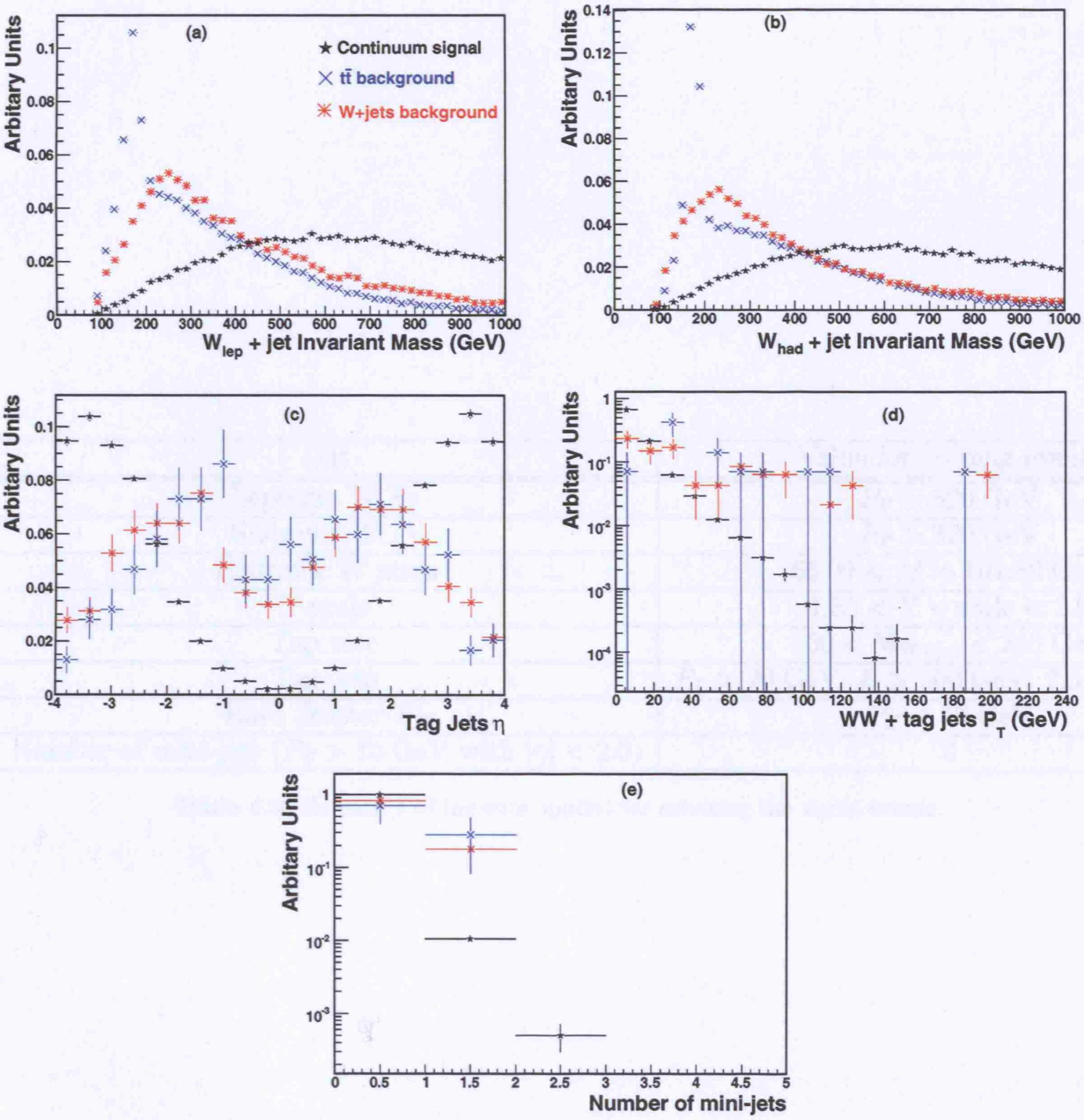

Figure 4.9: Distributions of the features from the hadronic environment, as described in the text, for both the signal and background samples: (a-b) Mass of the W^{lept} and the W^{had} combined with each of the jet in the event, other than the W^{had} . (c) η distribution of the tag jets. (d)P_T distribution of the system $W_{lept}W_{had}$+tag jets (e) Number of mini-jets.

Cut	Value for keeping events
Leptonic W P_T	$P_T > 320$ GeV
Hadronic W P_T	$P_T > 320$ GeV
Hadronic W mass	$66.09 < M < 101.89$ GeV
Y-scale	$1.55 < \mathrm{Y} - \mathrm{scale} < 2.0$
Top veto	$130 < \mathrm{M}_{\mathrm{W+jet}} < 240$ GeV
Tag Jets	$P_T > 20$ GeV, $E > 300$ GeV, $2.0 < \|\eta\| < 4.5$
Hard Scatter P_T	$P_T < 50$ GeV
Number of mini-jets ($P_T > 15$ GeV with $\|\eta\| < 2.0$)	0

Table 4.3: Summary of the cuts applied for selecting the signal events.

CHAPTER 5

Results

The final Chapter presents the results of the analysis, focusing on the potential of the ATLAS detector to see strong vector scattering signals above the background and to distinguish the different spin states of the possible resonances. The WW scattering cross section will be an important measurement, therefore the methodology for doing so will be presented. Beyond that, a comparison between ATLFAST and the GEANT (Full) simulation of the detector will demonstrate the very good agreement between the two. Finally, issues such as the effect of the underlying model and of the pile-up will be also discussed.

5.1 Final significance

The effect of each one of the previous cuts on the cross section for both the signal and background samples is presented in Table 5.1. The Y-scale cut has an important effect on the W+jets background, with a rejection factor of 45%, while for the signal sample, this is 15%, coming mainly from the misidentified W^{had} , which survived the previous mass cut. The top-veto reduces most of the $t\bar{t}$ events, as expected, with a rejection of 95%, while keeping the rejection of the signal low, around 9%. The rest of the hadronic cuts have very small effect on the signal sample. For instance, the cut on the hard scatter gives a

Cross-section σ (fb)	Signal	$t\bar{t}$	W+jets	Significance
Generated	44	15640	62600	0.86
Cuts				
P_T Leptonic W	3.301±0.011	387.481±0.992	2879.670±5.354	0.32
P_T Hadronic W	2.579±0.009	174.524±0.671	1813.100±4.285	0.32
Mass Hadronic W	2.038±0.008	80.739±0.456	208.354±1.472	0.66
Y Scale	1.735±0.008	65.839±0.413	114.015±1.090	0.71
Top Veto	1.585±0.007	3.308±0.092	52.782±0.742	1.16
P_T, E, η Tag Jets	0.449±0.004	0.039±0.010	0.490±0.071	3.38
P_T hard scatter	0.439±0.004	0.018±0.007	0.292±0.055	4.32
Number of Mini-jets	**0.434±0.004**	**0.013±0.006**	**0.240±0.050**	**4.73**

Table 5.1: The effect of the applied cuts (see text) on the cross section for both the signal (continuum scenario) and background samples. The errors are due to statistics only and the significance is given for integrated luminosity of $L = 30\ fb^{-1}$.

Cross-section σ (fb)	Continuum	Vector	Scalar	Scalar + Vector
Generated	44.0	52.4	74.9	118.2
Cuts				
P_T Leptonic W	3.301±0.011	4.696±0.014	7.666±0.021	11.548±0.032
P_T Hadronic W	2.579±0.009	3.773±0.012	5.853±0.018	7.590±0.026
Mass Hadronic W	2.038±0.008	3.037±0.011	4.692±0.017	5.922±0.024
Y Scale	1.735±0.008	2.595±0.010	4.096±0.016	5.243±0.022
Top Veto	1.585±0.007	2.351±0.010	3.692±0.015	4.660±0.021
P_T, E, η Tag Jets	0.449±0.004	0.680±0.005	1.025±0.008	1.267±0.011
P_T hard scatter	0.439±0.004	0.665±0.005	0.100±0.008	1.233±0.011
Number of Mini-jets	**0.434±0.004**	**0.658±0.005**	**0.990±0.008**	**1.226±0.011**

Table 5.2: The effect of the applied cuts (see text) on the cross section for all signal scenarios.The errors are due to statistics only.

rejection only 2% on the signal, 40% on the W+jets and almost 54% on the $t\bar{t}$ sample. It is important to mention, though, that the MC statistical errors, while small in the case of the signal sample (1% for the final cross section), they can not be ignored in the case of the W+jets and the $t\bar{t}$ samples (21% and 50% respectively).

Table 5.2 presents the effect of the cuts on the cross section for all the signal scenarios.

The significance S for an integrated luminosity L is computed with the formula:

$$S = \frac{N_{signal}}{\sqrt{N_{background}}} = \frac{\sigma_{signal}}{\sqrt{\sigma_{background}}} \cdot \sqrt{L} \qquad (5.1)$$

Scenario	Final Significance
Scalar Resonance (A)	10.78
Vector Resonance (B)	7.16
Scalar+Vector Resonance (C)	13.35
Continuum (D)	4.73

Table 5.3: Final significance for integrated luminosity of $L = 30\ fb^{-1}$ for the scenarios A, B, C and D.

where σ_{signal} and $\sigma_{background} = \sigma_{W+jets} + \sigma_{t\bar{t}}$ are the signal and background cross sections respectively. For an integrated luminosity of 30 fb^{-1}, the effect of the cuts on the significance is given in the last column of Table 5.1, where Table 5.3 summarizes the final significance for the scenarios A, B, C and D. All scenarios, apart from the Continuum, give significance more than 5σ and we could support that a resonance of any type could be seen above the background. The continuum scenario is the most pessimistic one. It gives very low significance compared to the rest.

Finally, to get the expected number of events for the signal and the background processes for integrated luminosity L and as a function of the WW invariant mass, one should scale the final histogram by a factor of:

$$F = \frac{L \cdot \sigma}{N_{MC}} \tag{5.2}$$

where N_{MC} is the number of generated events. For the different resonances and the continuum scenario this is shown on the plot (a) of Figure 5.1. The error bars at each entry come from the Monte Carlo statistical errors, scaled at the desired luminosity.

Since the experimental data will include both processes, it is more realistic to plot the sum of the signal and the background expected events. This is shown at plot (b) and now the error bars come from the statistical errors of each bin:

$$\begin{aligned} N_i &= S_i + B_i \\ \sigma_{N_i} &= \pm\sqrt{N_i} \end{aligned} \tag{5.3}$$

If we want to get the actual number of the signal events, then the background should be subtracted from the last distribution. The background estimation comes from the Monte Carlo simulation and its reliability should be checked against a set of reference data. For this analysis, we assume that the background processes are well described by the generator. The number of the signal events and the expected error will now be:

$$
\begin{aligned}
N_i^{Signal} &= N_i - B_i \\
\sigma_{N_i^{Signal}} &= \pm\sqrt{\sigma_{N_i}^2 + \sigma_{B_i}^2}
\end{aligned}
\tag{5.4}
$$

The final expected number of signal events after the background subtraction is shown at plot (c) of Figure 5.1, where Figure 5.2 gives the same distribution for three values of integrated luminosity: 30, 100 and 1000 fb^{-1}. As more and more data is collected, the statistical errors become smaller, allowing an increase of the significance of the observation.

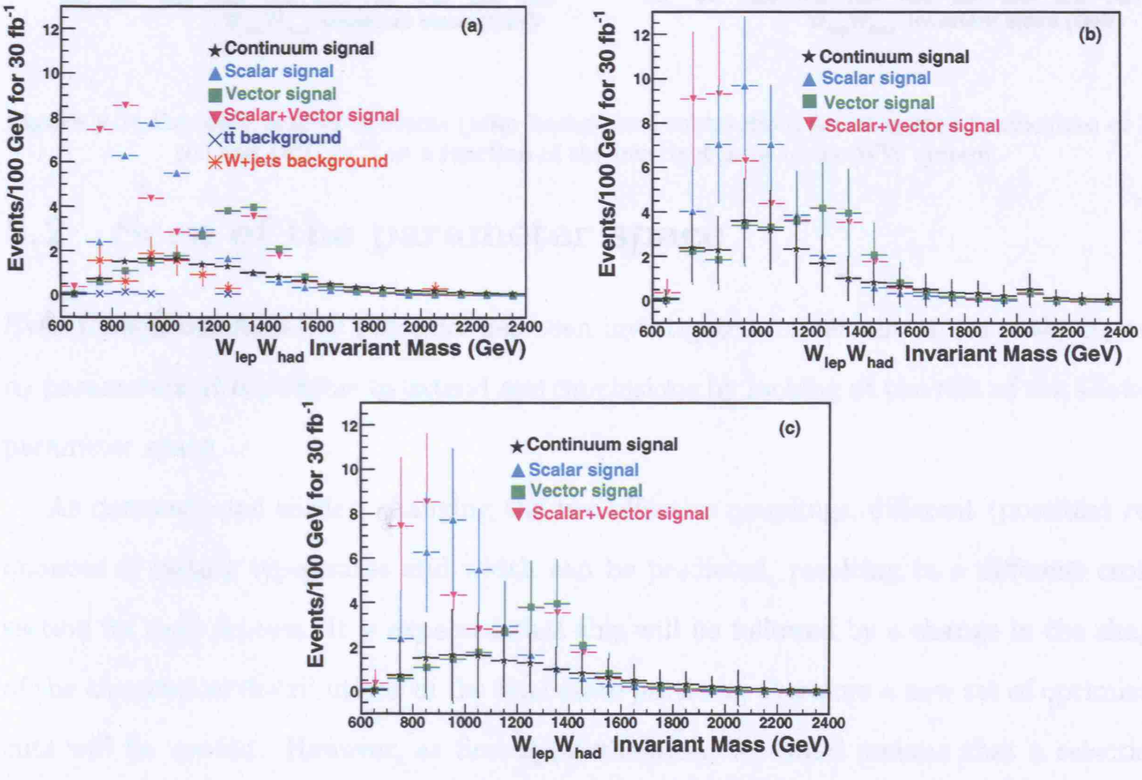

Figure 5.1: Expected number of events for integrated luminosity of $L = 30\ fb^{-1}$ as a function of the invariant mass of the WW system:(a) for the signal and background samples (with MC statistical errors) (b) for the sum of the signal and background (c) for the signal after background subtraction.

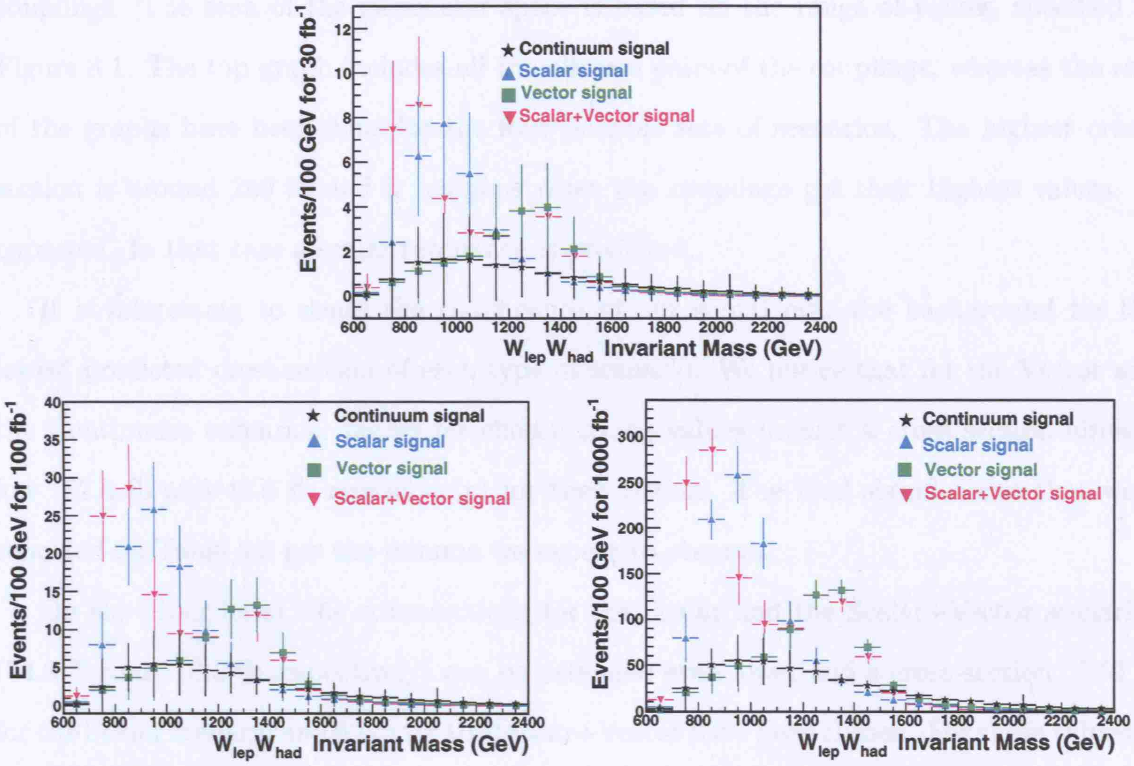

Figure 5.2: Expected number of events (after background subtraction) for integrated luminosities of 30, 100 and 1000 fb^{-1} as a function of the invariant mass of the WW system.

5.2 Scan of the parameter space

Even though the discovery potential has been investigated for certain values of the α_4 and α_5 parameters, it is possible to extend our conclusions by looking at the rest of the allowed parameter space.

As demonstrated earlier, changing the two effective couplings, different (possible) resonances of certain type, mass and width can be predicted, resulting in a different cross-section for each process. It is expected that this will be followed by a change in the shape of the kinematical distributions of the final state particles, therefore a new set of optimized cuts will be needed. However, at first approximation, we could assume that a selection of different (α_4, α_5) pairs, within a given region of the parameter space, will affect the distributions only by a scale factor, proportional to the cross-section.

Figure 5.3 shows the cross-section for WW scattering for different values of the effective couplings. The scan of the parameter space is based on the range of values, specified in Figure 3.1. The top graph includes all the allowed pairs of the couplings, whereas the rest of the graphs have been done for the four possible sets of scenarios. The highest cross-section is around 250 fb and it happens when the couplings get their highest values, as expected. In that case a scalar resonance is predicted.

It is interesting to study the significance of our signal over the background for the lowest predicted cross-section of each type of scenario. We notice that for the Vector and the Continuum scenarios, the so far chosen α_4, α_5 values predict a cross section already low (52.4 fb and 44.0 fb respectively) for their region. The final significances that were reported on Table 5.3 are the minima we expect to observe.

On the other hand, the cross-sections for the Scalar and the Scalar+Vector scenarios (74.9 fb and 118.2 fb respectively) can be extended even lower and a cross-section of 50 fb for the Scalar scenario and 60 fb for the Scalar+Vector have been chosen. For these values of the cross-section, it is easily calculated that the final significance for integrated luminosity of $L = 30\ fb^{-1}$ is 7.19 for the Scalar and 6.78 for the Scalar+Vector scenarios, again higher than 5σ with respect to the background. To extend that over the whole parameter space, the required integrated luminosity for 5σ observation of WW events above the expected background is plotted in Figure 5.4 and with approximately 32 fb^{-1} the ATLAS detector will be in position to say whether the observed WW events are coming from expected SM processes or not.

5.3 Observation of Resonances above the Continuum

To distinguish a resonance spectrum from the Continuum, one should start by understanding the shape of the Continuum distribution: a monotonically decreasing distribution with a peak, introduced by the kinematic cuts on the reconstructed objects. For this reason we parametrize the whole shape using a Landau function of the form:

$$P(x; m, s) = \frac{1}{x\sqrt{2\pi s^2}} e^{-(\ln x - m)^2/2s^2},\ x > 0 \tag{5.5}$$

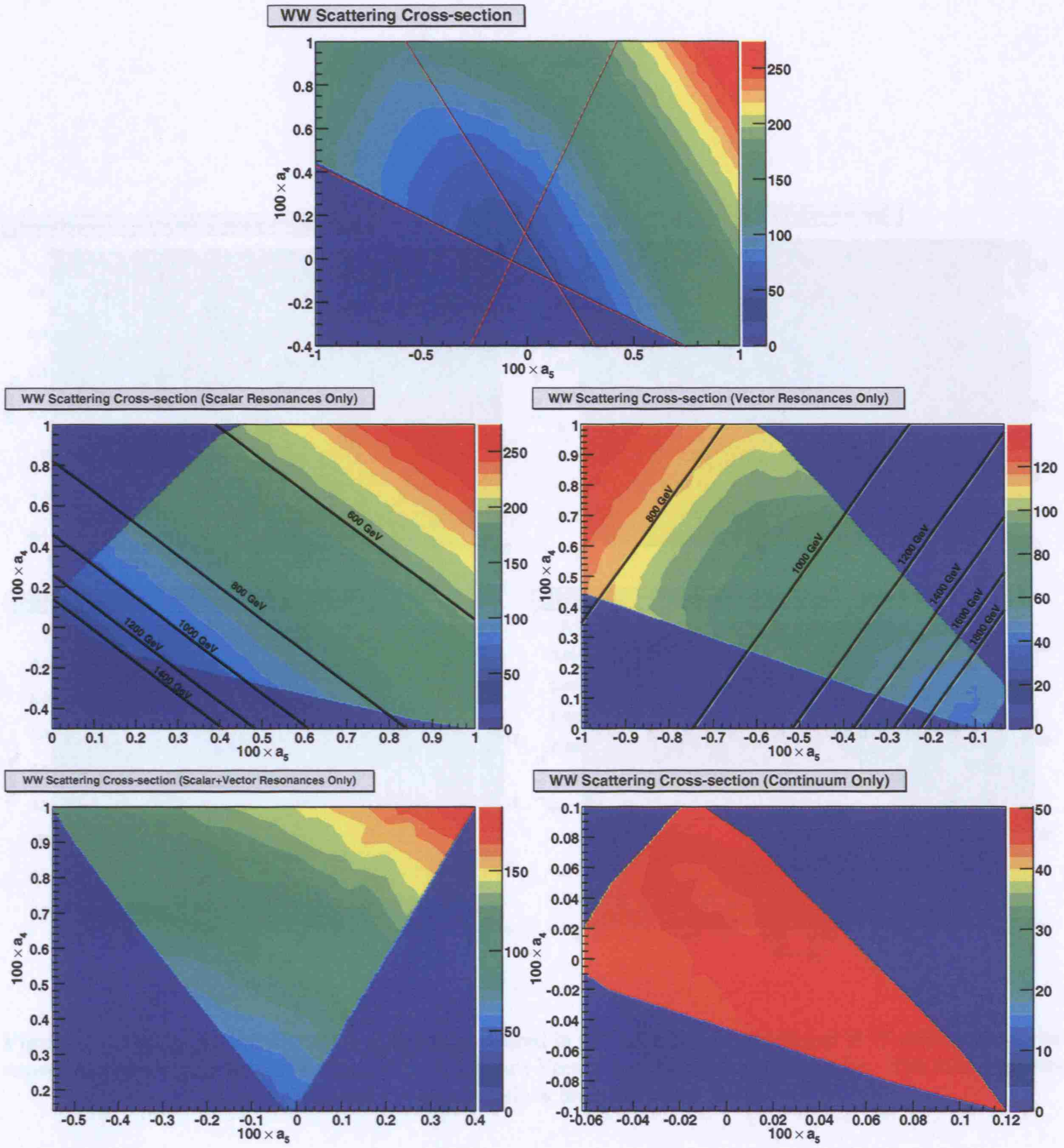

Figure 5.3: WW scattering cross-sections (with the coloured scale on the right in fb) for different values of the α_4, α_5 couplings in all the allowed parameter space (top) and more specifically for regions of a Scalar, Vector, Scalar+Vector and a Continuum scenario. For the Scalar and the Vector scenarios the lines of equal masses are drawn.

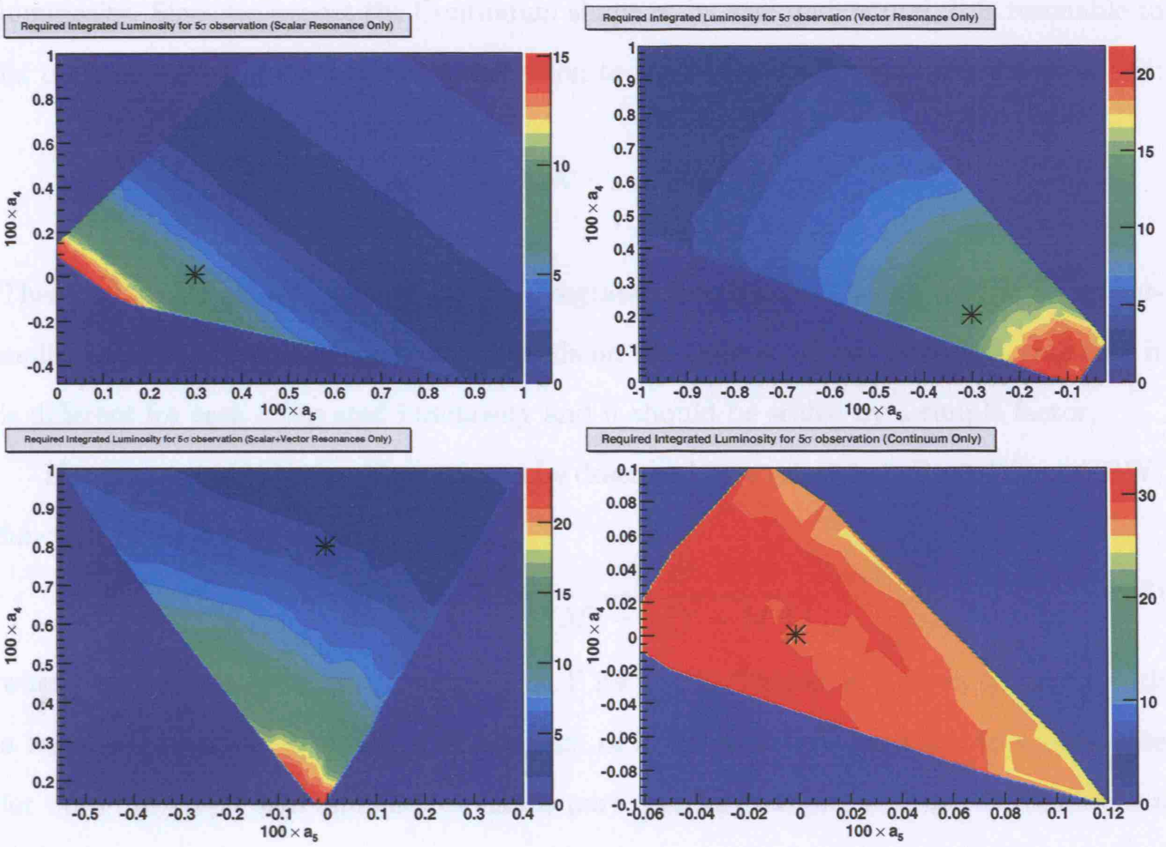

Figure 5.4: Required integrated luminosity, measured in fb^{-1}, for 5σ observation of WW events above the expected background for the Scalar, Vector, Scalar+Vector and Continuum scenarios. The star markers indicate the α_4, α_5 values used as a case study.

where m is the Most Probable Value and s is the width of the distribution, in which the integral of this function is normalized:

$$\int_0^\infty P(x; m, s)dx = s \tag{5.6}$$

Figure 5.5 shows the fit of the expected Continuum spectrum with 30 fb^{-1} integrated luminosity. Since we expect the Continuum shape to be well understood, it is resonable to fix the parameters of the Landau distribution to their values obtained from the shown fit:

$$m = 1000\,\mathrm{GeV}\ ;\ s = 140\,\mathrm{GeV}$$

These values should not depend on the integrated luminosity. On the contrary, the normalization factor (Landau constant) depends on the amount of data collected, therefore it is different for each integrated luminosity and it should be scaled by a simple factor.

If a resonance is present, the peak can be described by a relativistic Breit-Wigner (BW) function of the form:

$$f(M; m_o, \Gamma) = \frac{C}{(M^2 - m_o^2)^2 + M^2\Gamma^2} \tag{5.7}$$

where m_o is the mass of the resonance and Γ its width. Therefore, a given spectrum with a resonance part can be fitted with the sum of a Landau+BW function, to accomodate for both the continuum and the resonance part. As an example, a fit of the distribution of the Vector scenario is shown in Figure 5.5. In order for the fitting proceedure to give reasonable output parameters, the following limits are set on the BW mass and width:

$$m_o = 600 - 2400\,\mathrm{GeV}\ ;\ \Gamma = 200 - 700\,\mathrm{GeV}$$

The mass limits are set such that they cover the whole measurable range. The lower limit on the width is selected to accomodate for the binning of the histograms (100 GeV/bin), whereas the upper limit comes from the relation between the mass of the resonance and its width (Equation 3.11).

Finally, in order to estimate the probability of observing a resonance peak above the Continuum, we use a Toy Monte Carlo method based on the expected distributions. The principle of this technique is that, for each bin i, we use the expected value E_i of a specific scenario (continuum, vector or scalar) to generate a random number O_i from a Poisson distribution with mean $\mu = E_i$. The resulting M_{WW} distribution is fitted with a function, which is the sum of the Landau and the BW. After the fit, the significance of the BW constant parameter is checked, since the Continuum spectrum is expected to have no BW component. One can find in Appendix E examples of such fits for each luminosity phase and for the Vector and the Continuum scenarios.

For integrated luminosities of 30, 100 and 1000 fb^{-1}, Table 5.4 shows how often the BW constant has significance more than 2σ, 3σ or 5σ in the case of the Continuum, the Scalar and the Vector scenarios.

For 30 fb^{-1}, only 2% of the fits of a Continuum spectrum give BW constant greater than twice its error, whereas this is almost 64% for fits of a Scalar resonance and 46% for a Vector resonance. If we further require significance greater than 3σ, then there are (almost) no such cases for the Continuum scenario but 41% of the fits of a Scalar scenario and 7% of a Vector will satisfy this requirement. Finally, there are no cases where the BW constant will have more than 5σ significance.

As we increase the integrated luminosity, a resonance peak will be distinguished above the Continum. At this point, it should be stressed that, while more data is collected, statistical errors of the distributions become smaller, therefore a better description of the Continuum spectrum will be feasible. Since for the 30 fb^{-1} the statistical errors are not negligible, a Landau function fits the data with resonably well. But this is not the case for higher integrated luminosities, where the fit of a Landau function was not always of a good quality.

The small number that we get for the Vector resonance at 100 fb^{-1} is due to the fact that, since this particularly chosen scenario has a small cross-section, it is very difficult to spot the resonance with 5σ significance at an early stage. It will require more than

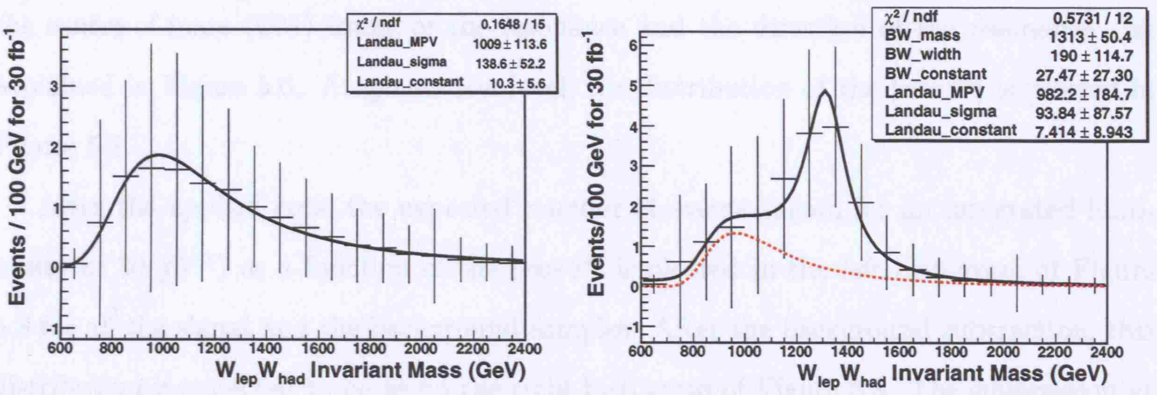

Figure 5.5: For 30 fb^{-1}, the expected Continuum spectrum fitted with a Landau distribution (left) and the scenario of a Vector resonance fitted with a Landau+BW distribution (right), where the Landau component is shown in red.

100 fb^{-1} to significantly see peaks of low cross-sections.

	$L = 30\ fb^{-1}$	$L = 100\ fb^{-1}$	$L = 1000\ fb^{-1}$
Continuum			
2σ	1.9 ± 0.4 %	5.9 ± 0.7 %	6.7 ± 0.8 %
3σ	$< 10^{-3}$ %	1.3 ± 0.4 %	0.4 ± 0.2 %
5σ	$< 10^{-3}$ %	$< 10^{-3}$ %	$< 10^{-3}$ %
Scalar			
2σ	63.5 ± 1.5 %	98.3 ± 0.4 %	100.0 %
3σ	41.0 ± 1.6 %	72.9 ± 1.4 %	100.0 %
5σ	$< 10^{-3}$ %	57.9 ± 1.6 %	100.0 %
Vector			
2σ	45.6 ± 1.6 %	92.2 ± 0.8 %	100.0 %
3σ	7.0 ± 0.8 %	69.2 ± 1.4 %	100.0 %
5σ	$< 10^{-3}$ %	1.6 ± 0.4 %	100.0 %

Table 5.4: Frequencies of the significance of the BW constant for 30, 100 and 1000 fb^{-1} integrated luminosity and for Toy Monte Carlo distributions from the Continuum, Scalar and Vector scenarios.

5.4 Distinguish among different scenarios

Once we can see a resonance, it is important to investigate whether it is a vector (spin-1) or a scalar (spin-0) particle.

The difference between the spin states is demonstrated by the distribution of the helicity angle θ^*, which is defined by the angle between one of the vector bosons, boosted in the centre-of-mass (CM) frame of the resonance and the direction of the resonance , as explained in Figure 5.6. At generation level, the distribution of the $|\cos\theta^*|$ is plotted in Figure 5.7.

After the applied cuts, the expected number of events (again for an integrated luminosity of 30 fb^{-1}) as a function of the $|\cos\theta^*|$ is plotted in the left histogram of Figure 5.8 for all the signal and the background samples. After the background subtraction, this distribution is expected to be as on the right histogram of Figure 5.8. The suppression at high values of $\cos\theta^*$ is due to the applied P_T cuts, since by requiring high values of P_T, we bias towards high values of θ^*.

In order to see our potential to assign an observed distribution to a scalar or to vector particle, we use a Toy Monte Carlo method, as explained in the previous section.

The next step is to check how often a given hypothesis H_o will be rejected at a given confidence level (CL). The hypothesis is checked using the the χ^2 test [64], where the χ^2 variable is constructed as follows:

$$\chi^2 = \sum_i \left[\frac{E_i - O_i}{\sigma_{E_i}}\right]^2 \tag{5.8}$$

For the above equation, E_i and σ_{E_i} are both taken from the right distribution of Figure 5.8 and O_i is taken from the Toy Monte Carlo. The χ^2 variable will follow a χ^2 distribution with N_{DoF} degrees of freedom and if $\chi^2 > \chi^2(\alpha\,; N_{DoF})$, then H_o is rejected at α% CL.

This method has been applied using the hypothesis H_o that the observed distribution comes from a resonance of type R. The outcome of the χ^2 test with $N_{DoF} = 10$ is given on Table 5.5 using the scalar expected values as input to our Toy Monte Carlo and on Table 5.6 using the expected values from the vector resonance.

For example, if an observed distribution is due to a scalar particle, then, at 95% CL, there is only ~ 4% chance to reject the hypothesis that it is a scalar and ~ 72% of the times we will reject the hypothesis that it comes from a vector. On the other hand, if the observed resonance is a vector particle, then, with the same CL, we will reject the hypothesis that it is vector with almost 5% probability and we will reject the wrong hypothesis of a scalar only ~ 58% of the time. In this sense, we will be more confident that the decision that will be made is the correct one, if the particle is scalar.

To approach the problem in a more realistic way, instead of using the case in which we know there is one single resonance for the whole WW mass spectrum, we look at the angular distribution when the WW mass is within a certain window. For this, we use the scalar+vector sample, where there are two peaks: the low mass peak due to a scalar particle and the high mass peak due to a vector particle, as it is given by Table 3.1. The distributions we get by looking at events with $M_{WW} < 1.1$ TeV and with $1.1 \text{ TeV} < M_{WW} < 1.6$ TeV are presented in Figure 5.9. By doing so, it can be seen that we manage to isolate the two components of the scalar+vector angular distribution: on the left histogram, the purple distribution falls at high values of $|\cos\theta^*|$, with the same behavior as with a scalar, whereas on the right histogram, it rises before it falls, which is a feature of a vector particle.

Hypothesis	68% CL	95% CL	99% CL
H_o =Scalar	12.83 ± 0.03	3.86 ± 0.02	2.49 ± 0.02
H_o =Vector	92.57 ± 0.03	72.29 ± 0.04	55.11 ± 0.05

Table 5.5: Frequencies (expressed in %) of rejection the hypothesis H_o at three different confidence levels using the χ^2 test. The true distribution came from a scalar.

Hypothesis	68% CL	95% CL	99% CL
H_o =Scalar	87.03 ± 0.03	57.80 ± 0.05	41.77 ± 0.05
H_o =Vector	10.78 ± 0.03	4.75 ± 0.02	4.09 ± 0.02

Table 5.6: Frequencies (expressed in %) of rejection the hypothesis H_o at three different confidence levels using the χ^2 test. The true distribution came from a vector.

5.5 Measuring the WW scattering cross-section

The measurement of the cross-section for the WW scattering will be a key analysis with the LHC data. Since this cross-section is predicted by the Standard Model with the existence of a scalar Higgs particle, this measurement will be a first check for the validity of the

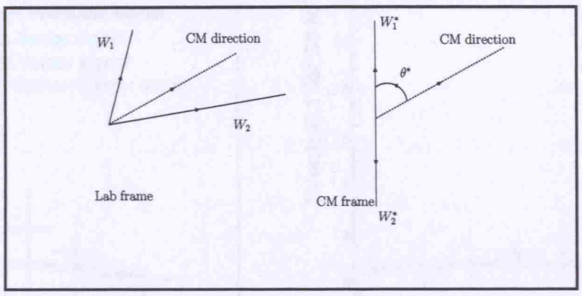

Figure 5.6: Definition of the angle θ^*.

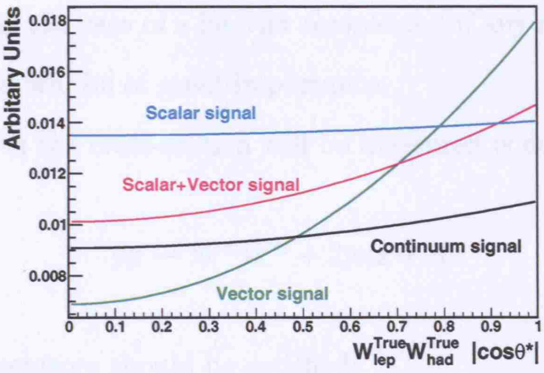

Figure 5.7: True distribution of the quantity $|\cos\theta^*|$ for different signal scenarios.

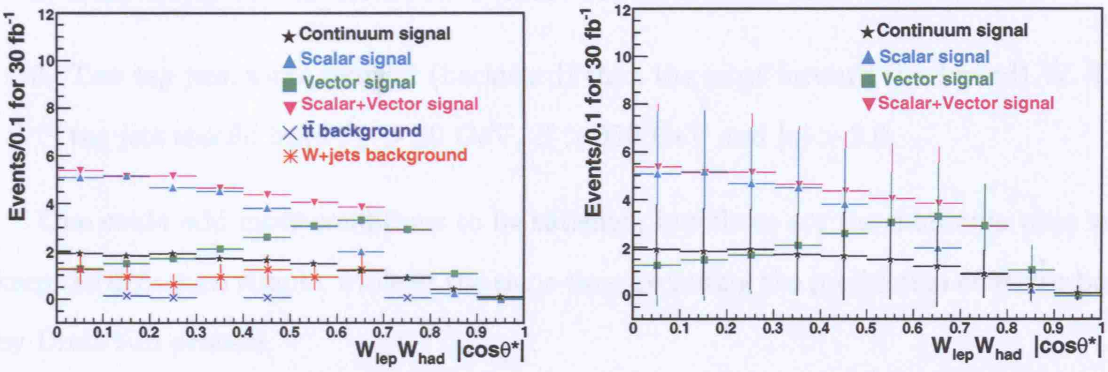

Figure 5.8: Expected number of events as a function of $|\cos\theta^*|$ for the signal and background samples (left) and for the signal samples after the background subtraction (right).

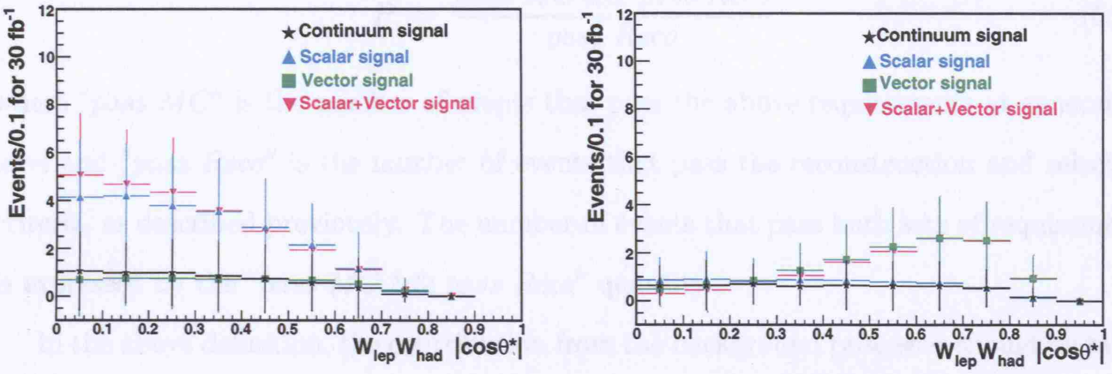

Figure 5.9: Expected number of events (after background subtraction) as a function of $|\cos\theta^*|$ for the signal scenarios when $M_{WW} < 1.1$ TeV (left) and 1.1 TeV $< M_{WW} < 1.6$ TeV (right).

Standard Model. Also in the case of a heavier resonance (of any model), the measurement of the WW cross-section will be of great importance.

The process for which the cross-section will be measured is defined as:

$$pp \to W^{\pm}W^{\pm} + 2\text{jets} + X \tag{5.9}$$

and the following requirements should be satisfied:

1. One of the vector bosons decays into a lepton (electron or muon) and a neutrino, where the other vector boson decays into hadrons.
2. Both vector bosons should have transverse momentum more than 320 GeV.
3. Two tag jets, more forward (backward) than the most forward (backward) W. These tag jets should have $P_T > 20$ GeV, $E > 300$ GeV and $|\eta| > 2.0$.

One could add more conditions to be satisfied, but those are the minimum ones which keep the definition simple, while at the same time excluding the production of vector bosons by Drell-Yan process.

The efficiency E and the purity P are defined as follows:

$$E = \frac{pass\ MC\ \&\&\ pass\ Reco}{pass\ MC} \tag{5.10}$$

$$P = \frac{pass\ MC\ \&\&\ pass\ Reco}{pass\ Reco} \quad (5.11)$$

where "*pass MC*" is the number of events that pass the above requirements at generation level and "*pass Reco*" is the number of events that pass the reconstruction and selection criteria, as described previously. The number of events that pass both sets of requirements is expressed by the "*pass MC && pass Reco*" quantity.

In the above definition, the contribution from the background processes should be taken into account. More specifically, the number of $t\bar{t}$ events should be included in both the efficiency and purity calculations, but the number of $W + jets$ events can be only included in the denominator of the purity, since there is only one W produced. It is important that the number of signal and background events are expressed for the same integrated luminosity.

Table 5.7 gives the overall efficiency and purity for the four scenarios, computed for 30 fb^{-1} integrated luminosity. Both the efficiency and the purity are rather low, not because of the contribution of the background sample (which is negligible after the reconstruction cuts), but due to the fact that the reconstruction of a signal event does not always agree with the generated one.

Scenario	Overall efficiency (%)	Overall purity (%)	Ratio P/E
Scalar Resonance (A)	16.56 ± 5.04	24.19 ± 7.02	1.46
Vector Resonance (B)	12.51 ± 5.16	18.92 ± 7.51	1.51
Scalar+Vector Resonance (C)	15.31 ± 4.47	22.38 ± 6.26	1.46
Continuum (D)	12.00 ± 5.83	18.39 ± 8.60	1.53

Table 5.7: Overall efficiency and purity as defined by Equations 5.10 and 5.11. The statistical errors are calculated for $L = 30\ fb^{-1}$.

For a given integrated luminosity L and assuming N_{obs} observed number of events of the process 5.9, the cross section is calculated by the formula:

$$\sigma = \frac{N_{obs} \times P}{E \times L} \quad (5.12)$$

To be able to calculate the required luminosity for a significant measurement of the above cross-section ($\sigma > 5\Delta\sigma$), we use the last equation to express the expected error on the cross-section as a function of the errors on the quantities involved. Assuming Gaussian errors, the uncertainties are propagated and it results that:

$$\frac{\Delta^2\sigma}{\sigma^2} = \frac{P}{E \times L \times \sigma} + \frac{\Delta^2(P/E)}{(P/E)^2} + \frac{\Delta^2 L}{L^2} \tag{5.13}$$

where $\Delta(P/E)$, ΔL are the estimated errors on the ratio of the overall efficiency versus purity and on integrated luminosity.

The issue of how well we know the efficiency and the purity will be addressed by comparing the LHC data to our control MC samples, since those variables are strongly associated with how well we can reconstruct the jets and identify the vector bosons. For low luminosities, the statistical uncertainties will dominate the error on the measured cross-section, but as more data is collected, it is necessary to set an error on the efficiency and purity values. In order to estimate this error we notice, using Table 5.7, that the ratio P/E, which is used in Equation 5.13, has a value almost constant for all the scenarios and the relative difference between its maximum and minimum values is almost 5%. For the rest of this section, to account for the errors on the ratio P/E, a convervative value of 10% will be used.

The error on the luminosity is expected to be around 5% of its value [39, 65].

For each scenario of the parameter space, the required luminosity for 5σ measurement of the WW cross-section is calculated by solving Equation 5.13 for L and the results are presented in Figure 5.10. In the case of the existence of a resonance, a significant measurement can be achieved with around 60-70 fb^{-1} of data, whereas in the most pessimistic case of a continuum spectrum, approximately 80 fb^{-1} of integrated luminosity will be required.

Finally, the efficiency and purity can be calculated as a function of the WW mass. This has been done only for the signal samples and in the range of 600 GeV up to 2.4 TeV in steps of 200 GeV (9 bins in total) and counting the number *"pass MC"* and *"pass Reco"* for each bin of the generated (or reconstructed) WW mass. Only events in which both the generated and reconstructed WW mass belong to the same bin are counted for the "*pass MC && pass Reco*" number. The final result is presented in Figure 5.11.

We first notice that the efficiencies and purities are mostly independant of the underlying scenario. The low value of the efficiency and purity for the first bin is due to the P_T cut on the reconstructed W bosons as can be seen in Figure 5.12 which shows the change in the efficiency after each cut, compared to its previous, as a function of the WW mass. The graduate decrease in the efficiency at high WW masses is mainly due to two reasons: (i) the cut on the mass of the $\mathrm{W^{had}}$. Figure 5.13 demonstrates that only for masses of the WW system up to ~1.4 TeV, the mass of the $\mathrm{W^{had}}$ is reconstructed close to the nominal value. Therefore, with the constant window cut on the $\mathrm{W^{had}}$mass, the efficiency is expected to fall for higher WW masses. (ii) the resolution of the WW mass. As will be discussed in the next section, the fractional resolution of the WW mass is constant, approximately 4%. The absolute resolution is ~36 GeV for WW masses in the range of 600-800 GeV and it rises up to 72 GeV for masses 1.8-2.4 TeV. Consequently, a bin size of 200 GeV used for the efficiency and purity graphs is not enough to take into account the resolution at higher masses.

5.6 Resolutions

It is important to check the resolution that is achieved on major kinematic variables, since this will give an estimate on how well the cuts are tuned for the specific analysis. Once again, it should be stressed that the tuning will be effectively done with the LHC data and it may well be the case that they are different than those chosen here. However, it is still important to know the accuracy of the reconstruction in order to support the validity of the physics results.

It is interesting to see the achieved resolution and any systematic shifts as a fraction of the quantity of interest. Therefore, for the following, the resolution will be defined as:

$$\text{Resolution} = \frac{\text{True Quantity} - \text{Reconstructed Quantity}}{\text{Reconstructed Quantity}} \tag{5.14}$$

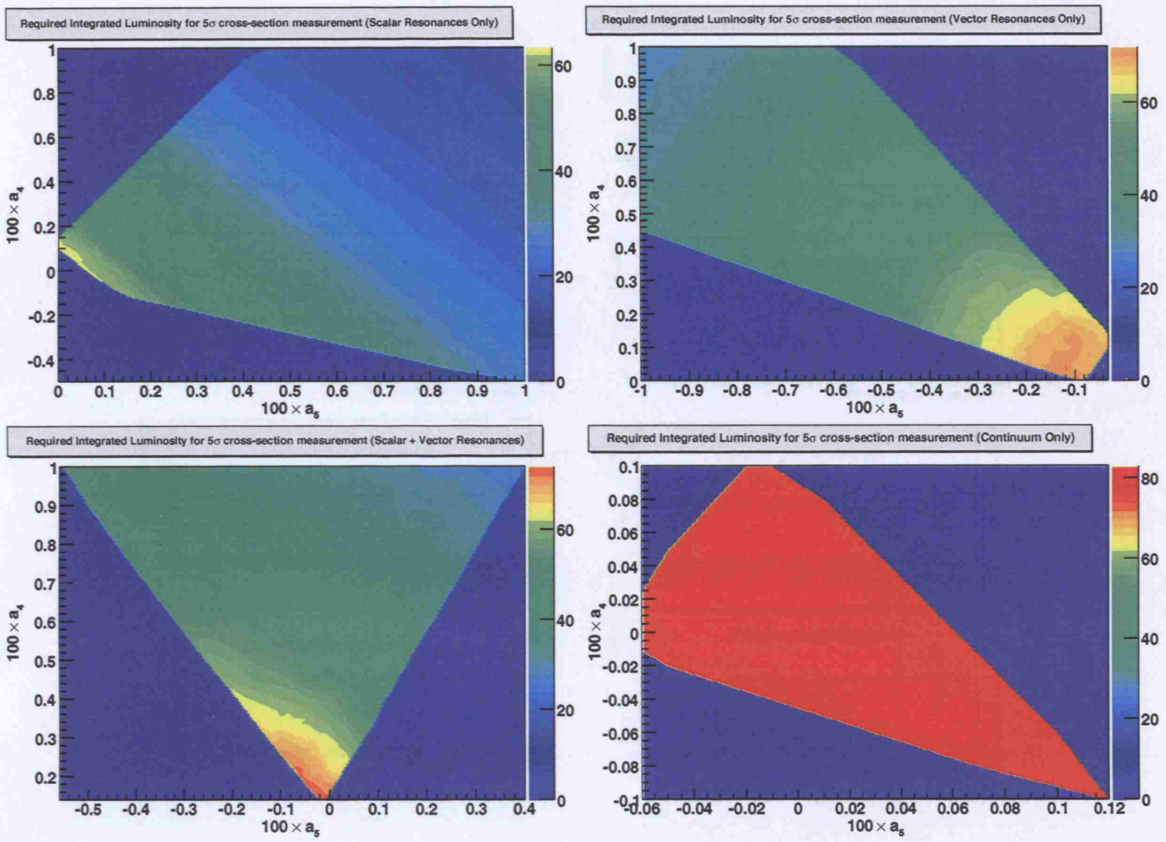

Figure 5.10: Required integrated luminosity for 5σ measurement of the cross-section for the process 5.9 and for the Scalar, Vector, Scalar+Vector and Continuum scenarios.

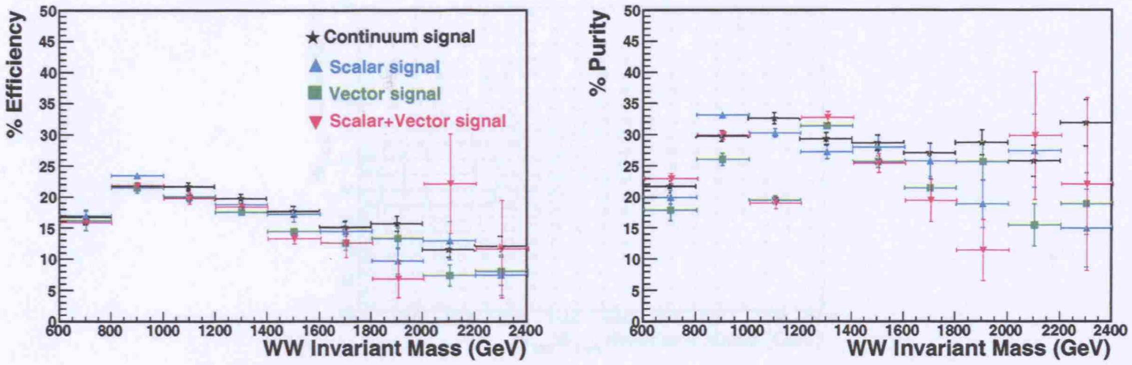

Figure 5.11: Efficiency and Purity as defined by Equations 5.10 and 5.11 as a function of the WW mass for all the signal scenarios.

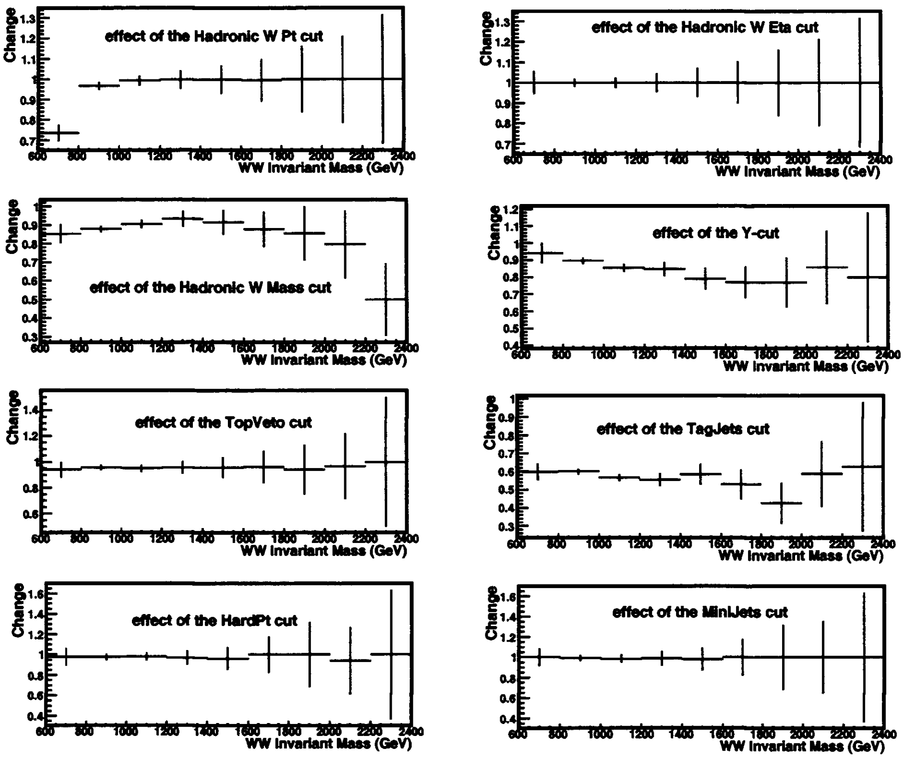

Figure 5.12: Change of the efficiency after each cut compared to its previous, as a function of the WW mass, using the Scalar scenario.

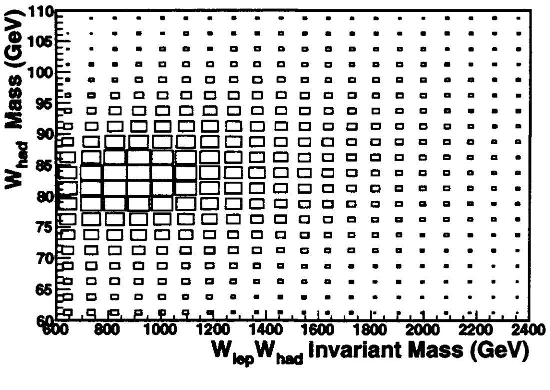

Figure 5.13: The mass of the reconstructed hadronic W versus the WW invariant mass.

The only exception is for the η and ϕ distributions, where the resolution is defined only as the deviation of the reconstructed quantity from the true one (thus it is not dimensionless). The final distributions are fit with a gaussian function within a reasonable range.

In Figure 5.14, some representative distributions are shown, whereas Table 5.8 summarizes the resolutions for all the important kinematic variables [1]. In all cases, the mean value is consistent with zero, which means that there are no significant systematic shifts. The only exception is for the hadronic W mass, where the 4% shift of the mean value indicates a potential jet miscalibration. The 1% shift of the energy of the leptonic W reflects the systematic error that is introduced by selecting the wrong neutrino solution. As far as the gaussian sigma is concerned, this is around 4% of the P_T of the bosons and the mass of the WW system. However, since the gaussian fit was applied for a specific, rather small range, the actual shape of the distributions should be looked at more carefully. For instance, the resolution distribution of the P_T of the tag jets has long, uniformly distributed tails on both sides, which indicates that the reconstruction of the tag jets could be almost 50% away from the true ones. Finally, it is also important to notice the asymmetry in the distribution for the WW mass resolution: reconstruction tends to underestimate the true WW mass.

5.7 Comparison between the Full and ATLFAST simulation

In order to check the reliabilty of the ATLFAST simulation, a sample of ten thousand Continuum events were simulated with the GEANT4 toolkit [66]. The material and the geometry of the ATLAS detector have been taken into account in order to simulate accurately the passage of all the generated particles through the detector. The digitization of the produced hits, where the expected output from electronics is simulated, has been performed using the ATLAS-DC3-02 detector description, without including mininum bias

---

[1] The forward and backward jets demonstrate the same behavior.

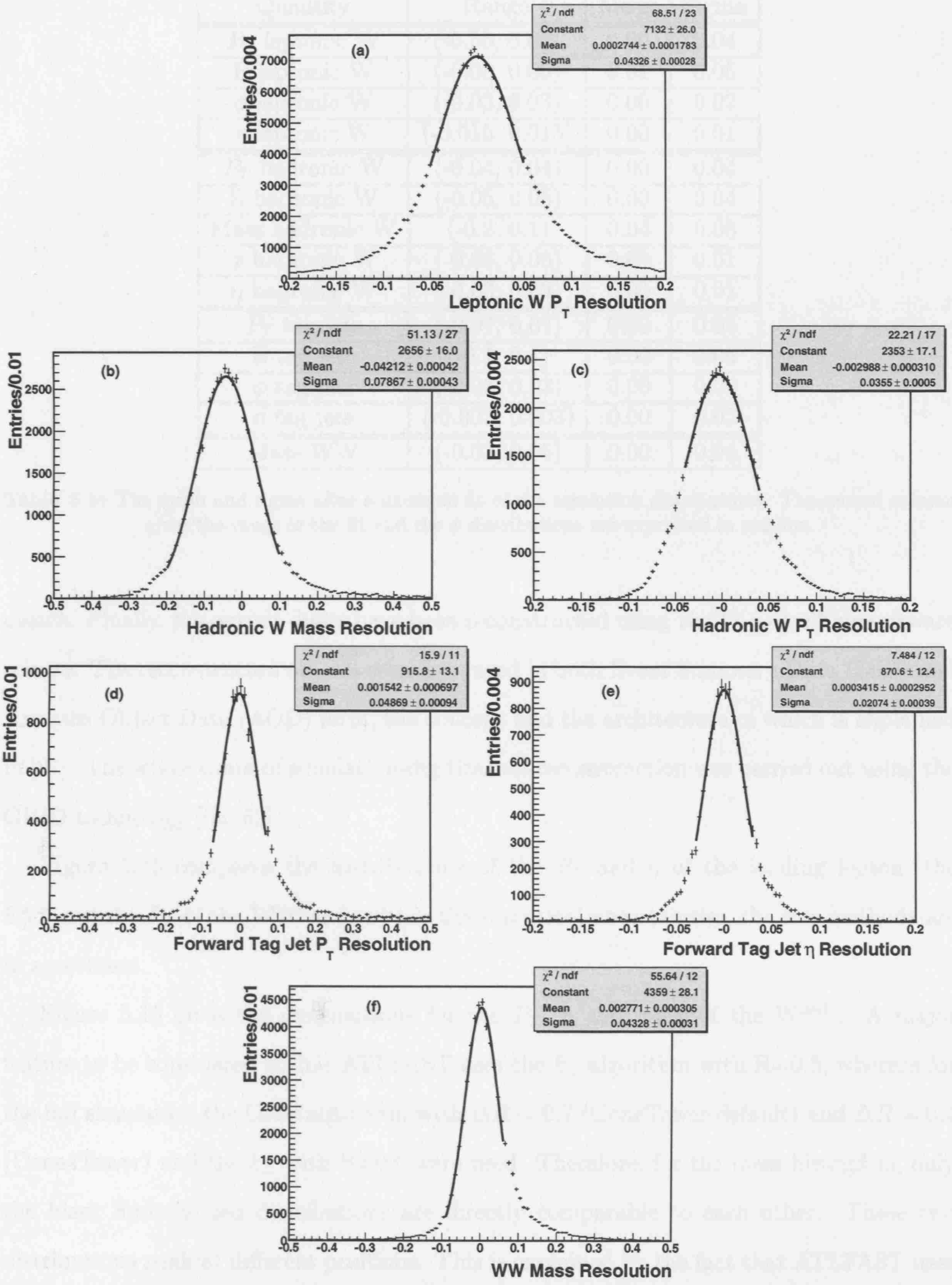

Figure 5.14: Resolution distributions (as defined by Equation 5.14) for representative kinematic quantities.

Quantity	Range	Mean	Sigma
P_T leptonic W	(-0.05, 0.05)	0.00	0.04
E leptonic W	(-0.05, 0.05)	0.01	0.05
ϕ leptonic W	(-0.03, 0.03)	0.00	0.02
η leptonic W	(-0.015, 0.015)	0.00	0.01
P_T hadronic W	(-0.04, 0.04)	0.00	0.04
E hadronic W	(-0.05, 0.05)	0.00	0.04
Mass hadronic W	(-0.2, 0.1)	0.04	0.08
ϕ hadronic W	(-0.06, 0.06)	0.00	0.01
η hadronic W	(-0.03, 0.03)	0.00	0.01
P_T tag jets	(-0.07, 0.07)	0.00	0.05
E tag jets	(-0.1, 0.1)	0.00	0.06
ϕ tag jets	(-0.03, 0.03)	0.00	0.02
η tag jets	(-0.003, 0.003)	0.00	0.02
Mass WW	(-0.03, 0.06)	0.00	0.04

Table 5.8: The mean and sigma after a gaussian fit of the resolution distributions. The second column gives the range of the fit and the ϕ distributions are expressed in radians.

events. Finally, the output digits have been reconstructed using the 11.0.41 offline software release. The reconstructed objects were produced in both Event Summary Data (ESD) and Analysis Object Data (AOD) form, the concept and the architecture of which is explained in [67]. The whole chain of simulation-digitization-reconstruction was carried out using the GRID technology [68, 69].

Figure 5.15 compares the distributions of the P_T and η of the leading lepton, the $\mathrm{E_T^{miss}}$ and the P_T of the $\mathrm{W^{lept}}$ and, within the statistical uncertainties, the two methods are in agreement.

Figure 5.16 gives the distributions for the P_T, η and mass of the $\mathrm{W^{had}}$. A major feature to be considered is that ATLFAST uses the $k_\perp$ algorithm with R=0.5, whereas for the full simulation the Cone algorithm with $\Delta R = 0.7$ (ConeTower-default) and $\Delta R = 0.4$ (Cone4Tower) and the $k_\perp$ with R=0.5 were used. Therefore, for the mass histogram, only the black and the red distributions are directly comparable to each other. These two distributions peak at different positions. This is explained by the fact that ATLFAST uses jet calibration constants which obtained with a Cone algorithm of $\Delta R = 0.4$, whereas for the full reconstruction, the calibration constants were obtained using the Cone algorithm with $\Delta R = 0.7$.

To compare the performance of the two methods regarding the jet reconstruction, one should compare the GEANT4-simulated jets reconstructed using Cone with $\Delta R = 0.7$ with the jets which were reconstructed using the same algorithm with the generator final state stable particles (so called particle jets). That step can be repeated by comparing the ATLFAST jets made with Cone $\Delta R = 0.4$ with the particle jets made by the same way. Figure 5.17 shows the mean value of the distribution P_T^{Rec}/P_T^{True} as a function of the P_T^{True} [2] for both the Full and ATLFAST simulation. With the Full simulation, the energy of the jets is overestimated, where with ATLFAST is underestimated but there is a slight tendency for both approaching the true value at high P_T. The Full simulation appears to have a more stable behaviour over the P_T range with no more than 2% deviation from the true value and with relatively small RMS. In constrast, ATLFAST gives significant fluctuations of the mean value (almost 5%) together with high RMS. The RMS values become comparable again at high P_T.

The task of comparing the Full and ATLFAST simulation requires definitely a more sophisticated approach (for instance, a detailed comparison is reported in [60]). Moreover, the jet calibration is a big issue itself, which will not be addressed here. As far as the present analysis is concerned, a significant impact must be expected on the $\mathrm{W^{had}}$ mass and on the Y-scale distributions[3]. Therefore, the applied cuts should be reconsidered and tuned. It is important to stress that the proper jet calibration will be carried out with the available LHC data, using well-controlled physics channels.

5.8 Effect of the Underlying Event Model

The underlying event (UE) is defined as the particles and the energy flow which come from a single proton-proton collision, except the process of interest. Such interactions are characterised by low P_T transfer and therefore the pertubative QCD calculations cannot

---

[2] The distributions were made for values of the P_T^{True} in the bins: [200,300), [300,400), [400,500), [500,600), [600,900) and ≥900 GeV.

[3] The comparison of the Y-scale was not feasible for technical reasons.

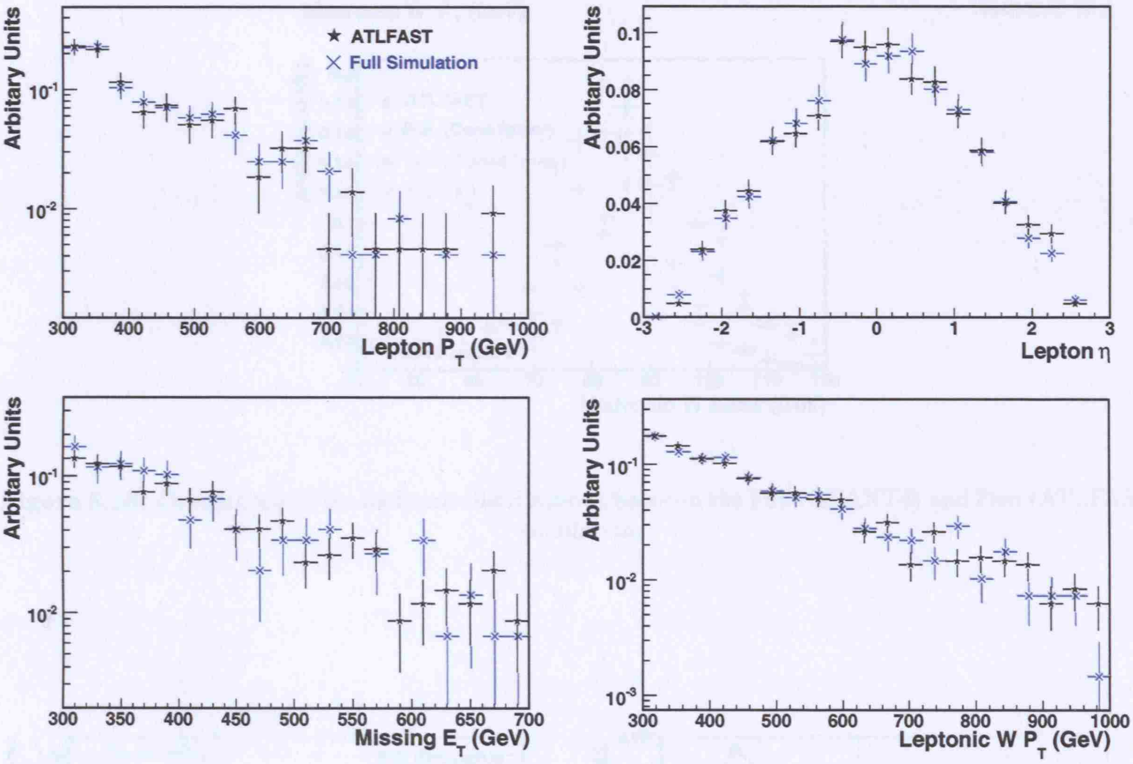

Figure 5.15: Comparison of the leptonic distributions between the Full (GEANT4) and Fast (ATLFAST) simulation.

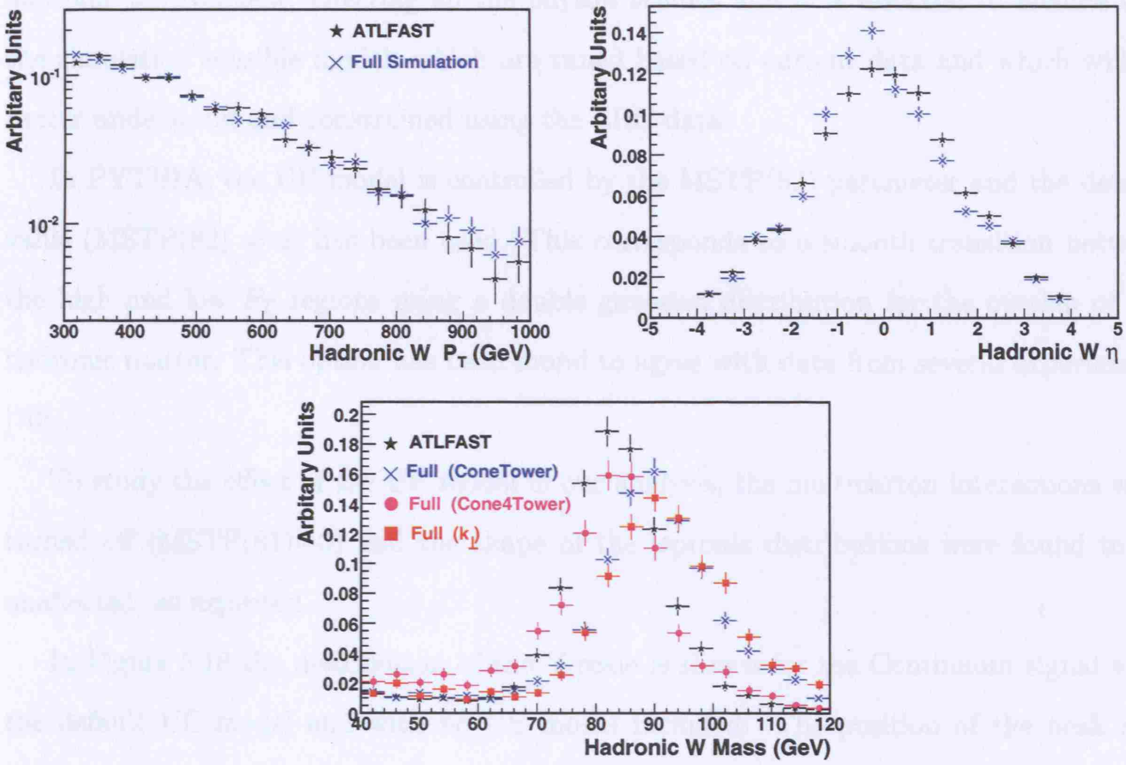

Figure 5.16: Comparison of the hadronic distributions between the Full (GEANT4) and Fast (ATLFAST) simulation.

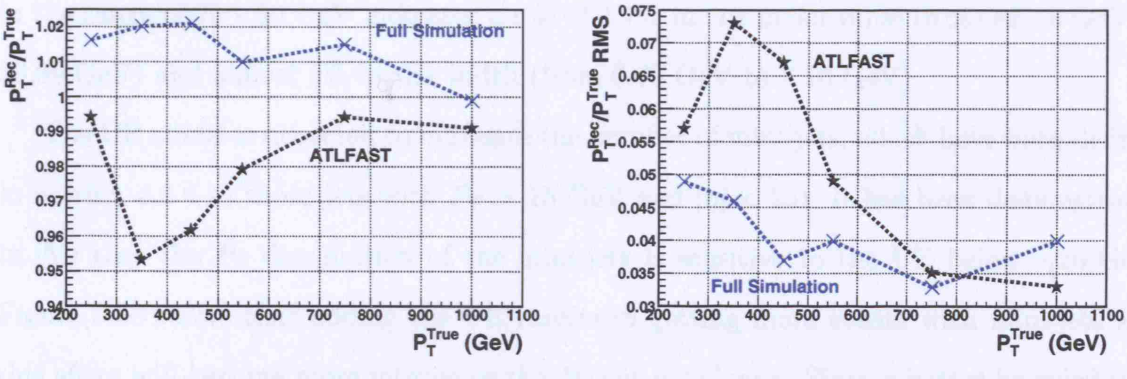

Figure 5.17: Mean (left) and RMS (right) values of the jets P_T^{Rec}/P_T^{True} distribution as a function of the P_T^{True} for the Full (GEANT4) and Fast (ATLFAST) simulation.

be applied. The UE is one of the most important but also most uncertain aspects of the hadronic environment, affecting all the physics studies and it is essential to include into the simulation sensible models which are tuned based on current data and which will be better understood and constrained using the LHC data.

In PYTHIA, the UE model is controlled by the MSTP(82) parameter and the default value (MSTP(82) = 4) has been used. This corresponds to a smooth transition between the high and low P_T regions using a double gaussian distribution for the overlap of the hadronic matter. This option has been found to agree with data from several experiments [70].

To study the effect of the UE model in our analysis, the multiparton interactions were turned off (MSTP(81)=0) and the shape of the leptonic distributions were found to be unaffected, as expected.

In Figure 5.18 the distribution of the Y-scale is shown for the Continuum signal with the default UE model and with no UE model included. The position of the peak and the shape of the distribution are not significantly affected, implying that the cut on this variable should be robust against such uncertainties.

The effect of the UE model on the reconstruction of the W^{had} is demonstrated in Figure 5.19. The P_T and the η distributions are not affected, but there is a significant shift of the mass distribution towards higher values when the UE model is added. A gaussian fit in the range of 70 - 90 GeV indicates a rise of 1.7% in the mean value (from 82.58 GeV to 83.99 GeV) and almost 6% in the width (from 6.76 GeV to 7.16 GeV).

The UE model is expected to influence the number of mini-jets, which have been defined in Section 4.3.4 as those jets with $P_T > 15$ GeV and $|\eta| < 2.0$. It has been demonstrated in [53] that the P_T distribution of the mini-jets is sensitive to the UE below ~20 GeV. Figure 5.20 shows that adding the UE results in getting more events with mini-jets and this effect will become more intense as the P_T cut gets lower. Since a better knowledge of the UE is required, the cut of the mini-jets contributes large systematic uncertainties to our analysis, especially for the background estimation.

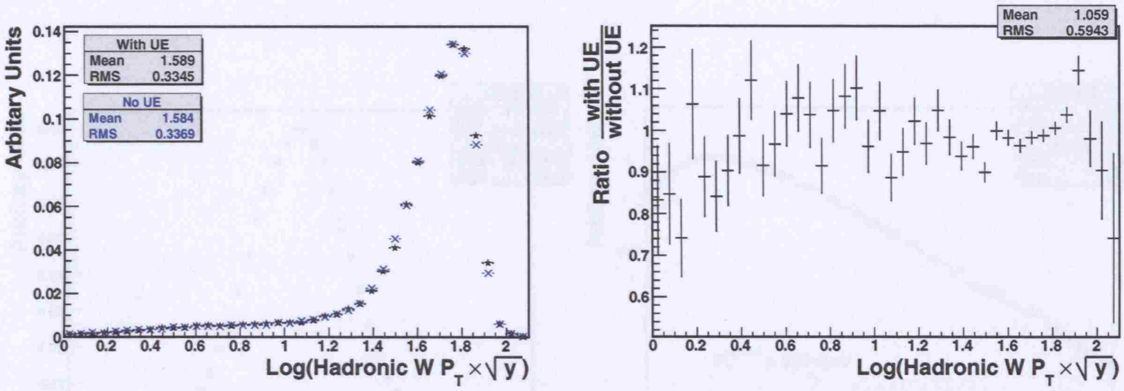

Figure 5.18: Effect of the underlying event model on the Y-scale variable.

	default ATLAS UE	Without UE
Cuts		
P_T Leptonic W	7.502 ± 0.024	7.587± 0.024
P_T Hadronic W	78.135 ± 0.138	78.089 ± 0.137
Mass Hadronic W	79.010 ± 0.154	79.871 ± 0.150
Y Scale	85.142 ± 0.151	84.671 ± 0.151
Top Veto	91.351± 0.129	93.927 ± 0.109
P_T, E, η Tag Jets	28.315 ± 0.217	27.470 ± 0.210
P_T hard scatter	97.835 ± 0.132	97.687 ± 0.135
Number of Mini-jets	98.906 ± 0.095	99.786 ± 0.042
Final Efficiency	**0.987±0.009**	**1.008±0.009**

Table 5.9: The effect of the UE on each of the applied cuts for the Continuum signal. The figures show the % drop after each cut compared to its previous and the last row gives the final efficiency after the applied cuts.

Finally, Table 5.9 summarizes the effect of the UE on the efficiencies after each individual cut for the Continuum signal. When the default ATLAS UE is added, the final efficiency drops by 2% relative to the case without UE. Since the background samples were generated using only the UE model, it is not possible to estimate the effect on the significance.

5.9 Effect of the Pile-up

The term 'pile-up' is used to describe all the interactions in a bunch crossing, apart from the interesting hard process between two partons. At high luminosity, it is expected to

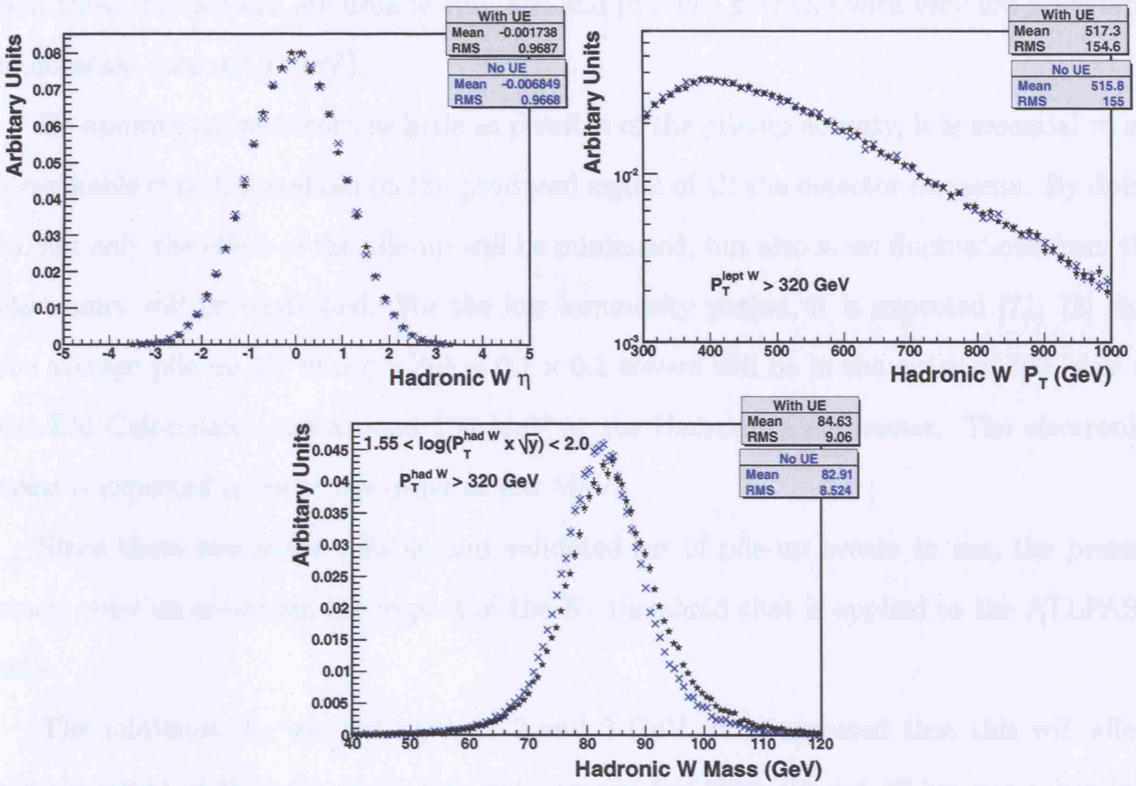

Figure 5.19: Effect of the underlying event model on the W^{had} .

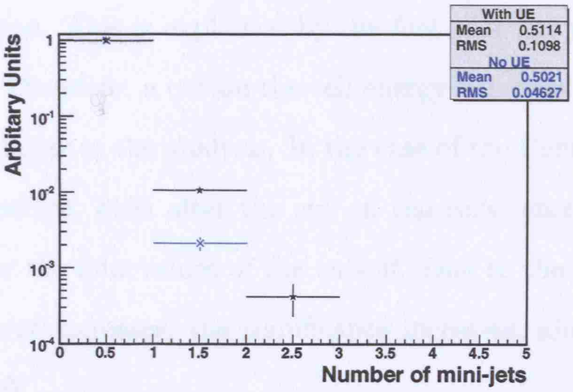

Figure 5.20: Effect of the underlying event model on the number of mini-jets.

have 20-25 proton-proton collisions for each bunch crossing. The main feature is the fact that those interactions are usually very soft and produce particles with very low transverse momentum (around 1 GeV).

To ensure that we record as little as possible of the pile-up activity, it is essential to set a resonable cut-off threshold on the produced signal of all the detector elements. By doing so, not only the effect of the pile-up will be minimised, but also noise fluctuations from the electronics will be controlled. For the low luminosity period, it is expected [71, 72] that the average pile-up E_T in $\Delta\eta \times \Delta\phi = 0.1 \times 0.1$ towers will be in the order of 300 MeV at the EM Calorimeter and around 100 MeV at the Hadronic Calorimeter. The electronics noise is expected to be at the order of few MeV.

Since there was not a reliable and validated set of pile-up events to use, the present study relies on observing the impact of the E_T threshold that is applied to the ATLFAST cells.

The minimum E_T was set at 0, 1, 2 and 3 GeV. It is expected that this will affect the clustering of the cells, since cells with energy less than the cut-off are not taken into account (unassociated cells). Figure 5.21 shows the final cross-section for the Continuum signal and the two background processes as a function of the E_T threshold. For the signal, the effect becomes significant after the 1 GeV and it drops by 16% at 3 GeV cut-off. For the background, the $t\bar{t}$ sample is almost unaffected, but the effect is severe for the W+jets with more than 60% drop. This is explained by the fact that the jets for this sample are mainly soft QCD jets. Therefore, a cut on the cell energy will result in jets with softer P_T spectrum which will fail cuts in the analysis. In the case of the Continuum and $t\bar{t}$ samples, the jets have harder spectra, even after the cut on the cells' energy. Figure 5.22 shows the final significance for the four values of the cut-off. Due to the sharp drop of the final W+jets events as the cut increases, the significance increases, almost by 23% when the threshold is set to 3 GeV.

The decision upon the energy threshold on the calorimeter cells (and the thresholds of the rest of the detector elements in general) will be made and the values will be tuned once

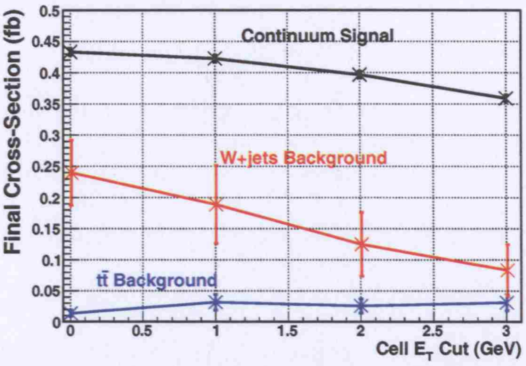

Figure 5.21: Final cross-sections for the signal and background samples for different cell thresholds.

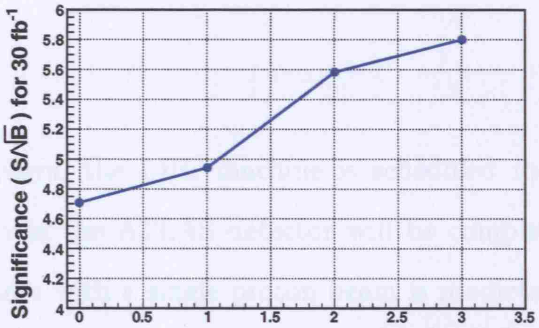

Figure 5.22: Final significance for $30fb^{-1}$ for different cell thresholds.

the LHC data is available. These thresholds will be strongly dependent on the luminosity of the beams. The estimation that we get using the ATLFAST cells demonstrate that the appropriate cut on the energy of the cells will have bigger effect on the the background processes and less on the signal, thus increasing the final signal-to-background ratio.

CHAPTER 6

Conclusions

Without significant delays, the LHC machine is scheduled to start in September 2007 and by that time most of the ATLAS detector will be completed. After commissioning with cosmic rays, a phase with a single proton beam is predicted and, in November 2007, LHC will collide proton beams at 900 GeV centre-of-mass energy and with a luminosity of approximately $10^{29}\ cm^{-2}sec^{-1}$. The full centre-of-mass energy at 14 TeV with a significant increase of the luminosity is planned for spring 2008.

The ATLAS detector will identify, in the harsh hadronic environment, the interesting physics events and record them in a period of time less than 2 sec. The Trigger system and particularly the Level-2 has been the subject of the first part of this Thesis. The concept of the Region of Interest has been introduced and its mechanism has been presented. It has been demonstrated that its size can be optimized using the available information from the 1st and 2nd samplings of the Electromagnetic Calorimeter in order to have an estimation of the vertex of the primary proton interaction. The method has been tested using single electron events of $P_T = 20$ GeV with low luminosity pile-up and of $P_T = 30$ GeV with high luminosity pile-up. In order to evaluate the results, we have focused on the performance of the IDSCAN package both in terms of execution time and of efficiency in reconstructing the correct primary vertex from the Inner Detector. The study has concluded that the mean execution time can be reduced by 28% at low luminosity and by 58% at high luminosity, where at the same time, the overall efficiency can be increased by 1% at low luminosity and by 6% at high luminosity. Further improvements, together with integration of the methodology in the official software, can be done for a broader P_T spectrum and using other parts of the detector, such as the information at Level-2 from the Muon Spectrometer.

In the second part of the Thesis, the physics of WW scattering has been studied in the case that no light, weakly-interacting Higgs is found to explain the Electroweak Symmetry Breaking. The motivation and theoretical formalism of the Electroweak Chiral Lagrangian has been presented which, under a specific unitarisation protocol, leads to resonances according to the values of two effective couplings, α_4 and α_5. For certain values of those parameters, a WW spectrum with no resonance is also predicted.

The event reconstruction has been done with the fast simulation package for the ATLAS detector. Using the k_T jet algorithm, the W-candidate jet was decomposed into sub-jets and the splitting scale was used to identify the cases where the jet comes from a decaying W, thus suppressing the W($\rightarrow \ell\nu$)+jets background. This proposed technique can be used in a wide range of physics channels which include highly boosted objects.

For the whole allowed space of the α_4, α_5 parameters, it has been demonstrated that ATLAS will be able to see, with more than 5σ significance, signal WW events above the expected background with 30 fb^{-1} of integrated luminosity, even in the most pessimistic scenarios. With the observed WW scattering events, A Toy Monte Carlo technique has been used to estimate the potential of identifying the existence of a resonance among the observed WW scattering events and to derive the type of the resonance, by exploiting the angular distribution of the decaying products.

As more data is collected, a significant measurement of the WW cross-section will be feasible. It has been demonstrated that the ATLAS detector will be able to measure the WW scattering cross-section in the kinematic region of 600 GeV up to 2.4 TeV of the WW mass with 80 fb^{-1} in the case that no resonance is present, whereas with an observed resonance, integrated luminosity of 60-70 fb^{-1} will be enough for a significant measurement.

The high energy mass region that was studied ensures the very energetic objects in our events, therefore there are no triggering issues involved. Finally, the current study has not taken into account any theoretical or other experimental uncertainties, currently contributing to the systematics errors and, by that sense, further improvements could be envisaged and will be certainly guided by the early LHC data. However, for the first years of the LHC operation, the results will be statistically limited, therefore the conclusions from this study will provide a good measure of what ATLAS will be able to achieve.

APPENDIX A

Parametrisation equations for the 1st and 2nd EM Samplings

Barrel

Maximum position of the 1st barrel sampling

$$R_1(mm) = \begin{cases} 1586 & \text{, if } |\eta| \leq 0.27 \\ 1599.6 - 46.8|\eta| & \text{, if } 0.27 < |\eta| \leq 0.6 \\ 1570.7 & \text{, if } 0.6 < |\eta| \leq 0.8 \\ 1545.3 & \text{, if } 0.8 < |\eta| \leq 1.0 \\ 1548.2 & \text{, if } 1.0 < |\eta| \leq 1.15 \\ 1629.5 - 72.0|\eta| & \text{, if } 1.15 < |\eta| \leq 1.35 \\ 1532.3 & \text{, if } |\eta| > 1.35 \end{cases} \tag{A.1}$$

Maximum position of the 2nd barrel sampling

$$R_2(mm) = \begin{cases} 1927.2 & ,\text{if } |\eta| \leq 0.5 \\ 2031.8 - 238.4|\eta| & ,\text{if } 0.5 < |\eta| \leq 0.8 \\ 1759.2 & ,\text{if } 0.8 < |\eta| \leq 1.0 \\ 2164.1 - 295.1|\eta| & ,\text{if } 1.0 < |\eta| \leq 1.5 \\ 1719.6 & ,\text{if } |\eta| > 1.5 \end{cases} \tag{A.2}$$

Endcap

Maximum position of the 1st endcap sampling

$$Z_1(mm) = \begin{cases} 3782.0 & ,\text{if } |\eta| \leq 1.7 \\ 3778.4 + 2.3|\eta| & ,\text{if } 1.7 < |\eta| \leq 2.1 \\ 3776.3 + 3.4|\eta| & ,\text{if } 2.1 < |\eta| \leq 2.27 \\ 3833.3 - 30.9|\eta| & ,\text{if } |\eta| > 2.27 \end{cases} \tag{A.3}$$

Maximum position of the 2nd endcap sampling

$$Z_2(mm) = \begin{cases} 4289.3 - 100.4|\eta| & ,\text{if } |\eta| \leq 2.2 \\ 4448.1 - 179.2|\eta| & ,\text{if } |\eta| > 2.2 \end{cases} \tag{A.4}$$

APPENDIX B

Calculation of the neutrino P_z for the decay $W \rightarrow \ell\nu$

Using Natural Units, the relativistic equation for the W mass is:

$$M_W^2 = E_W^2 - \vec{P}_W^2 = (E_\ell + E_\nu)^2 - (\vec{P}_\ell + \vec{P}_\nu)^2 \tag{B.1}$$

where $(E_\ell,\ \vec{P}_\ell)$ and $(E_\nu,\ \vec{P}_\nu)$ are the 4-vectors for the lepton and the neutrino respectively. For energies much greater than the mass of the lepton, the masses of the lepton and of the neutrino can be safely ignored. The two terms on the right-hand side of Equation B.1 can be written:

$$\begin{aligned}(E_\ell + E_\nu)^2 &= E_\ell^2 + E_\nu^2 + 2E_\ell E_\nu \simeq P_\ell^2 + P_\nu^2 + 2P_\ell P_\nu \\ &= P_\ell^2 + P_{z,\nu}^2 + P_{T,\nu}^2 + 2P_\ell\sqrt{P_{z,\nu}^2 + P_{T,\nu}^2}\end{aligned} \tag{B.2}$$

where $\vec{P}_{T,\nu} = (P_{x,\nu},\ P_{y,\nu})$ and $P_{z,\nu}$ are the transverse and z component of the neutrino's momentum.

$$\begin{aligned}(\vec{P}_\ell + \vec{P}_\nu)^2 &= P_\ell^2 + P_\nu^2 + 2\vec{P}_\ell \vec{P}_\nu \\ &= P_\ell^2 + P_{T,\nu}^2 + P_{z,\nu}^2 + 2\vec{P}_{T,\ell}\vec{P}_{T,\nu} + 2P_{z,\ell}P_{z,\nu} \qquad \text{(B.3)}\end{aligned}$$

Replacing Equation B.1 using Equations B.2 and B.3, we get:

$$\begin{aligned}M_W^2 &= 2P_\ell\sqrt{P_{z,\nu}^2 + P_{T,\nu}^2} - 2\vec{P}_{T,\ell}\vec{P}_{T,\nu} - 2P_{z,\ell}P_{z,\nu} \Rightarrow \\ M_W^2 + 2\vec{P}_{T,\ell}\vec{P}_{T,\nu} + 2P_{z,\ell}P_{z,\nu} &= 2P_\ell\sqrt{P_{z,\nu}^2 + P_{T,\nu}^2} \qquad \text{(B.4)}\end{aligned}$$

We now let:

$$\begin{aligned}\kappa &= M_W^2 + 2\vec{P}_{T,\ell}\vec{P}_{T,\nu} \\ \lambda &= 2P_{z,\ell} \qquad \text{(B.5)}\end{aligned}$$

By setting the mass of the W and using the reconstructed kinematical variables for the lepton and the neutrino ($\mathrm{E_T^{miss}}$), the quantities κ and λ are easily calculated. Using κ and λ, Equation B.4 gets the form:

$$\begin{aligned}\kappa + \lambda P_{z,\nu} &= 2P_\ell\sqrt{P_{z,\nu}^2 + P_{T,\nu}^2} \Rightarrow \\ \kappa^2 + \lambda^2 P_{z,\nu}^2 + 2\kappa\lambda P_{z,\nu} &= 4P_\ell^2(P_{z,\nu}^2 + P_{T,\nu}^2) \qquad \text{(B.6)}\end{aligned}$$

By re-arranging, the last equation becomes:

$$[4P_\ell - \lambda^2]P_{z,\nu}^2 - 2\kappa\lambda P_{z,\nu} + [4P_\ell P_{T,\nu}^2 - \kappa^2] = 0 \qquad \text{(B.7)}$$

If we finally set:

$$\begin{aligned}a &= 4P_\ell - \lambda^2 \\ b &= -2\kappa\lambda\end{aligned}$$

$$c = 4P_\ell P_{T,\nu}^2 - \kappa^2 \tag{B.8}$$

the Equation B.7 gets the familiar quadratic form:

$$aP_{z,\nu}^2 + bP_{z,\nu} + c = 0 \tag{B.9}$$

with solution:

$$P_{z,\nu} = \frac{b \pm \sqrt{b^2 - 4ac}}{2a} \tag{B.10}$$

when $b^2 - 4ac \geq 0$

Appendix C

Resolution functions used by ATLFAST

For the following RN will indicate a random number taken from a gaussian distribution centered at zero and with a unit variance. It should be assumed that it has different value each time it appears.

C.1 Electron smearer

Sampling Term (ST):

$$ST = RN \times \frac{0.12}{\sqrt{E}} \tag{C.1}$$

Noise Term (NT):

$$PT = RN \times \begin{cases} \frac{0.245}{P_T} & \text{, if } |\eta| < 1.4 \\ \frac{0.306[(2.4-|\eta|)+0.228]}{E} & \text{, if } |\eta| \geq 1.4 \end{cases} \tag{C.2}$$

Constant Term (CT):

$$CT = RN \times 0.07 \tag{C.3}$$

The Smearing Factor (SF) is:

$$SF = ST + NT + CT \tag{C.4}$$

Each of the four-components is smeared by the same (positive) amount of $1 + SF$.

In the case of High Luminosity, a Pile-up Term (PT) is added to the SF:

$$PT = \frac{RN}{P_T} \times \begin{cases} 0.32 & \text{, if } |\eta| < 0.6 \\ 0.295 & \text{, if } 0.6 \leq |\eta| < 1.4 \\ 0.27 & \text{, if } |\eta| \geq 1.4 \end{cases} \tag{C.5}$$

C.2 Photon smearer

For the photons, the angle θ is first smeared by a factor F:

$$F = \frac{RN}{\sqrt{E}} \times \begin{cases} 0.065 & \text{, if } |\eta| < 0.8 \\ 0.050 & \text{, if } 0.8 \leq |\eta| < 1.4 \\ 0.040 & \text{, if } 1.4 \leq |\eta| < 2.5 \\ 0.000 & \text{, if } |\eta| \geq 2.5 \end{cases} \tag{C.6}$$

This affects the P_z component of the momentum and the pseudo-rapidity, which are re-calculated. The rest of the smearing and pile-up factors are the same with those from the Electron Smearer, apart from the ST, which has the form:

$$ST = RN \times \frac{0.10}{\sqrt{E}} \tag{C.7}$$

C.3 Muon smearer

For the smearing of the muon's four-vector, the expected resolution from both the Inner Detector and the Muon Spectrometer have been considered.

For the Inner Detector, the two smearing quantities are:

$$ID_1 = 0.0005 \times RN \times \left(1 + \frac{|\eta|^{10}}{7000}\right) \times P_T + 0.012 \times RN \tag{C.8}$$

$$ID_2 = \sqrt{\left[0.0005 \times P_T \times \left(1 + \frac{|\eta|^{10}}{7000}\right)\right]^2 + (0.012)^2} \tag{C.9}$$

For the Muon Spectrometer, the two smearing quantities are:

$$MS_1 = 0.01 \times RS \tag{C.10}$$

$$MS_2 = RN \times 0.01 \times RS \tag{C.11}$$

where RS is the stand-alone muon spectrometer resolution for a muon of given momentum, pseudo-rapidity and phi. This is calculated by a FORTRAN interpolation between tables at $P_T = 100$ and 1000 GeV.

Based on the previous quantities, the weights for each part of the detector are:

$$W_{ms} = \frac{1}{MS_1^2} \tag{C.12}$$

$$W_{id} = \frac{1}{ID_1^2} \tag{C.13}$$

And the total weight is:

$$W_{tot} = W_{ms} + W_{id} \tag{C.14}$$

The Correction Factor (CF) is:

$$CF = \frac{W_{ms}(1 + MS_2) + W_{id}(1 + ID_1)}{W_{tot}} \tag{C.15}$$

Each of the four-components is smeared by the same (positive) amount of $1/CF$.

C.4 Jet smearer

For Low Luminosity, the SF is:

$$SF = \begin{cases} RN \times \frac{0.5}{\sqrt{E}} + RN \times 0.03 & ,\text{if } |\eta| < 3.2 \\ RN \times \frac{1.0}{\sqrt{E}} + RN \times 0.07 & ,\text{if } |\eta| \geq 3.2 \end{cases} \tag{C.16}$$

For High Luminosity, an extra pile-up term of the form

$$RN \times \frac{7.5}{P_T} \tag{C.17}$$

is added to the above SF.

Each of the four-components is smeared by the same (positive) amount of $1 + SF$.

APPENDIX D

The clustering procedure of the $k_\perp$ algorithm

Pre-clustering procedure

During the pre-clustering procedure the final hadrons are separated into 'beam jets' and 'hard final state jets' (exclusive mode of running). For each final state hadron h_k and for each combination of hadrons h_k, h_l, the algorithm starts by computing the resolution variables d_{kB} and d_{kl}, which are defined as:

$$\begin{aligned} d_{kB} &= 2E_k^2(1-\cos\theta_{kB}) \\ d_{kl} &= 2min(E_k^2, E_l^2)(1-\cos\theta_{kl}) \end{aligned} \tag{D.1}$$

where E_k, E_l are the energies of the hadrons h_k and h_l respectively, θ_{kB} is the angle of the hadron h_k momentum with respect to the beam direction and θ_{kl} is the angle between the momenta of the two hadrons.

In the small-angle limit, where $\theta_{kB} \to 0$ and $\theta_{kl} \to 0$, expanding the trigonometric function, we get:

$$\begin{aligned} d_{kB} &\simeq E_k^2 \theta_{kB}^2 \\ d_{kl} &\simeq min(E_k^2, E_l^2)\theta_{kl}^2 \end{aligned} \tag{D.2}$$

The transverse momentum $k_\perp$, in the small angle limit and for high relativistic hadrons, can be written as:

$$k_\perp = k \sin\theta \simeq E \sin\theta \sim E\theta \tag{D.3}$$

Therefore, the resolutions variables d_{kB} and d_{kl} can be reduced to the transverse momentum of the hadron with the respect to the beam and to the minimal relative transverse momentum of one hadron with respect to the other:

$$\begin{aligned} d_{kB} &\simeq k_{\perp\, kB}^2 \\ d_{kB} &\simeq k_{\perp\, kl}^2 \end{aligned} \tag{D.4}$$

The variable d_{kB} is finally scaled by the dimensionless parameter R^2, which is externally defined. Then, the minimum between the resolution variables is found. If d_{kl} is the smallest, then the hadrons h_k and h_l are combined together into a single object according to a specified recombination scheme, whereas if d_{kB} is the smallest, the hadron h_k has to be included in the beam jets.

The algorithm is repeated until all particles and objects have d_{kl}, d_{kB} larger that some stopping parameter d_{cut}. This stopping parameter can be either fixed to a value for all the events, or it can be defined on an event-by-event basis by the minimum value of d_{kl}, d_{kB} when the event contains a fixed number of hard final state jets.

Resolving into sub-jets

This procedure can be applied for the whole event using the final state jets and/or for a single jet with the following steps:

1. The resolution parameter y_{cut} is defined as:

$$y_{cut} = \frac{Q_o^2}{d_{cut}} \tag{D.5}$$

   where the parameter Q_o^2 fixes the fragmentation scale of the jets.

2. For each pair of hadrons (or objects more general), the variable d_{kl} as defined before is rescaled:

$$y_{kl} = \frac{d_{kl}}{d_{cut}} \tag{D.6}$$

3. From all the y_{kl} values, the smallest, y_{ij}, is defined. If $y_{ij} < y_{cut}$, then the objects i,j are combined into a single cluster according to a specific recombination scheme.

4. The procedure is repeated till all pairs of objects have $y_{kl} > y_{cut}$. The remaining objects are called sub-jets.

Again, as for the d_{cut} variable in the pre-clustering procedure, the y_{cut} can be defined when a desired number of sub-jets have been constructed.

APPENDIX E

Examples of BW+Landau fits to Toy MC distributions

The following distributions are examples of a Toy Monte Carlo for the Vector (top row) and the Continuum (bottom row) scenarios for 30, 100 and 1000 fb^{-1} integrated luminosity. Each distribution has been fitted with the sum of a Breit-Wigner and a Landau function (black line), as described in Chapter 5. The Breit-Wigner component is drawn in blue and the Landau component is drawn in red.

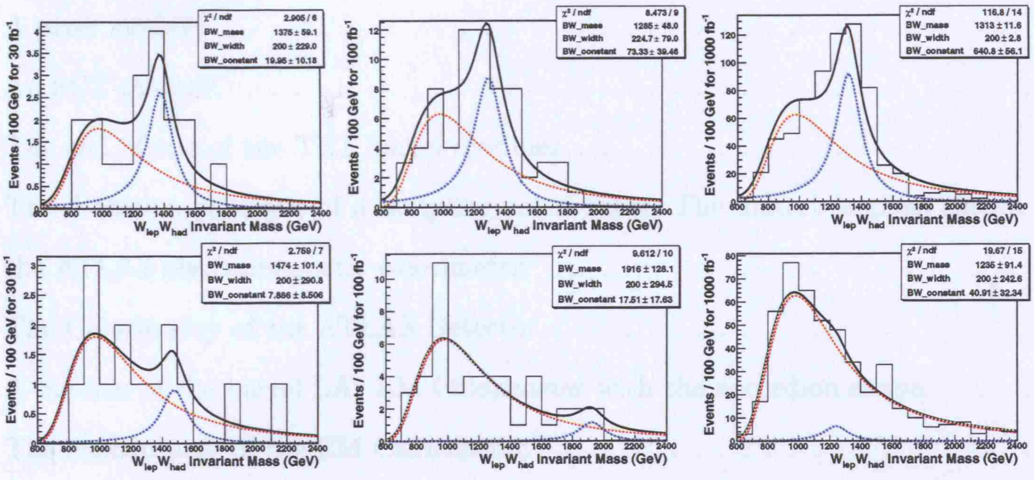

List of Figures

List of Tables

References

[1] The LEP Electroweak Working Group. *http://lepewwg.web.cern.ch/LEPEWWG* CERN-EP-200-016, March 2006.

[2] Grunewald M.W. Altarelli G. *Precision electroweak tests of the standard model.* Phys. Rept. **403-404**, 189–201 (2004).

[3] The Tevatron Electroweak Working Group. *http://tevewwg.fnal.gov* October 2005.

[4] R. Barate et al. *Search for the standard model Higgs boson at LEP.* Phys. Lett. **B565**, 61–75 (2003).

[5] ALEPH, DELPHI, L3, OPAL and SLD Collaborations. *Precision electroweak measurements on the Z resonance.* Phys. Rept. **427**, 257 (2006).

[6] Altarelli G. *The standard electroweak theory and beyond.* hep-ph/0011078 (2000).

[7] Bailin D. Love A. *Sypersymmetric gauge field theory and string theory.* Institute of Physics Publishing 1994.

[8] *LHC Design Report (Vol I and II)* CERN-2004-003.

[9] *ATLAS Inner Detector Technical Design Report (Vol I and II)* CERN/LHCC/97-16.

[10] *ATLAS Central Solenoid Technical Design Report* CERN/LHCC/97-21.

[11] *ATLAS Liquid Argon Calorimeter Technical Design Report* CERN/LHCC/96-41.

[12] *ATLAS Tile Calorimeter Technical Design Report* CERN/LHCC/96-42.

[13] *ATLAS MUON Spectrometer Technical Design Report* CERN/LHCC/97-22.

[14] *ATLAS Barrel Toroid Technical Design Report* CERN/LHCC/97-19.

[15] *ATLAS End-Cap Toroid Technical Design Report* CERN/LHCC/97-20.

[16] The European Physical Journal C. *Review of Particle Physics* chapter 35, 1986.

[17] Kleinknecht K. *Detectors for particle radiation.* Cambridge Universtity Press 1986.

[18] The RD3 Collaboration. *Test beam results of a stereo preshower integrated in the the liquid argon accordion calorimeter.* CERN-PE/97-133, 1997.

[19] *The ATLANTIS Event Display: http://www.hep.ucl.ac.uk/atlas/atlantis/.*

[20] C. W. Fabjan. *Calorimetry in High Energy Physics.* NATO Adv. Study Inst. Ser. B Phys. **128**, 281 (1985).

[21] Fanti M. *The ATLAS liquid argon calorimeters : construction, commissioning, and selected beam results (107-11, Vol. 1)* IEEE Nuclear Science Symposium and Medical Imaging Conference NSS-MIC, 2004.

[22] Henriques A. *ATLAS Detector Status.* XII International WorkShop on High Energy Physics and Quantum Field Theory (1997).

[23] *ATLAS Trigger Performance* CERN/LHCC/98-15.

[24] *ATLAS LVL1 Trigger Technical Design Report* ATLAS TDR-12.

[25] *ATLAS High-Level Trigger, Data Acquisition and Controls Technical Design Report* ATLAS TDR-016.

[26] Baines J et al. *ATLAS Trigger Menus* ATL-DAQ-98-121.

[27] *ATLAS Level-1 Technical Design Report.* CERN/LHCC/1998-14.

[28] N. P. Konstantinidis et al. *Architecture of the ATLAS high level trigger event selection software.* ATL-DAQ-2003-046.

[29] Konstantinidis N. Stefanidis S. Sutton M.R. *Optimisation of the size of the EmTau Region of Interest for the ATLAS Level-2 Trigger using the Electromagnetic Calorimeter* ATL-DAQ-PUB-2005-002.

[30] Monika Grothe et al. *Architecture of the ATLAS High Level Trigger Event Selection Software.* ECONF **C0303241**, WEPT004 (2003).

[31] *ATLAS High-Level Trigger Data Acquisition and Controls.* CERN/LHCC/2003-22.

[32] T.Shears M.P.Casao, S.González. *TrigT2Calo package:* http://atlas-sw.cern.ch/cgi-bin/cvsweb.cgi/offline/Trigger/TrigAlgorithms/TrigT2Calo/.

[33] M. Wielers S. González, T. Hansl-Kozanecka. *Selection of high-p_T electromagnetic clusters by the Second Level Trigger of ATLAS.* ATL-DAQ-2000-002.

[34] T. Shears S. González, B. González Pineiro. *First Implementation of Calorimeter FEX Algorithms in the LVL2 Reference Software.* ATL-DAQ-2000-020.

[35] T. Shears S. González. *Further Studies and Optimization of the Level-2 trigger electron/photon FEX algorithm.* ATL-DAQ-2000-042.

[36] N. Konstantinidis H. Drevermann. *Determination of the z position of primary interactions in ATLAS.* ATLAS-SOFT-2002-007.

[37] H. Drevermann N. Konstantinidis. *Algorithms to select space points of tracks from single primary interactions in ATLAS.* ATLAS-COM-DAQ-003-040.

[38] J. Baines *et al. Fast tracking for the ATLAS LVL2 Trigger.* ATL-DAQ-CONF-2005-001.

[39] *ATLAS Detector and Physics Performance (Vol I and II)* CERN/LHCC/99-14.

[40] Francis Halzen and Alan Martin. *Quarks and Leptons: Introductory Course in Modern Particle Physics.* John Wiley and Sons 1984.

[41] Michael S. Chanowitz and Mary K. Gaillard. *The TeV physics of strongly interacting W's and Z's.* Nucl. Phys. **B261**, 379 (1985).

[42] Benjamin W. Lee, C. Quigg and H. B. Thacker. *Weak interactions at very high-energies: the role of the Higgsboson mass.* Phys. Rev. **D16**, 1519 (1977).

[43] John M. Cornwall, David N. Levin and George Tiktopoulos. *Derivation of gauge invariance from high-energy unitarity bounds on the S-matrix.* Phys. Rev. **D10**, 1145 (1974).

[44] Steve King. *Introduction to Electroweak Symmetry Breaking.* CERN Tutorial (8th October 2002).

[45] Steven Weinberg. *Phenomenological Lagrangians.* Physica **A96**, 327 (1979).

[46] J. Gasser and H. Leutwyler. *Chiral perturbation theory to one loop.* Ann. Phys. **158**, 142 (1984).

[47] A. Dobado and Maria J. Herrero. *Phenomenological Lagrangian approach to the Symmetry Breaking Sector of the Standard Model.* Phys. Lett. **B228**, 495 (1989).

[48] A. Dobado, M. J. Herrero, J. R. Pelaez and E. Ruiz Morales. *LHC sensitivity to the resonance spectrum of a minimal strongly interacting electroweak symmetry breaking sector.* Phys. Rev. **D62**, 055011 (2000).

[49] A. S. Belyaev et al. *Strongly interacting vector bosons at the LHC: Quartic anomalous couplings.* Phys. Rev. **D59**, 015022 (1999).

[50] M. Golden, Tao Han and G. Valencia. *Strongly-interacting electroweak sector: Model independent approaches.* (1995).

[51] Tran N. Truong. *Chiral Perturbation theory and Final State Theorem.* Phys. Rev. Lett. **61**, 2526 (1988).

[52] Geoffrey F. Chew and Stanley Mandelstam. *Theory of low-energy pion pion interactions.* Phys. Rev. **119**, 467–477 (1960).

[53] J. M. Butterworth, B. E. Cox and Jeffrey R. Forshaw. *W W scattering at the LHC.* Phys. Rev. **D65**, 096014 (2002).

[54] J. R. Pelaez. *Resonance spectrum of the strongly interacting symmetry breaking sector.* Phys. Rev. **D55**, 4193–4202 (1997).

[55] Torbjorn Sjostrand, Leif Lonnblad and Stephen Mrenna. *PYTHIA 6.2: Physics and manual.* (2001).

[56] S. Eidelman et al. *Review of particle physics.* Phys. Lett. **B592**, 1 (2004).

[57] Robert V. Harlander and William B. Kilgore. *Next-to-next-to-leading order Higgs production at hadron colliders.* Phys. Rev. Lett. **88**, 201801 (2002).

[58] *https://twiki.cern.ch/twiki/bin/view/Atlas/RomeEvgenWiki.*

[59] Elzbieta Richter-Was, Daniel Froidevaux and Luc Poggioli. *ATLFAST 2.0 a fast simulation package for ATLAS.* ATL-PHYS-98-131.

[60] The ATLFAST Validation Task Force. *Performance of the ATLAS fast simulation ATLFAST.* ATLAS Communication note, 15 July 2006.

[61] Sarah Allwood. *High Mass WW Scattering at the LHC.* PhD Thesis, University of Manchester, 2006.

[62] S. Catani, Yuri L. Dokshitzer, M. H. Seymour and B. R. Webber. *Longitudinally invariant K(t) clustering algorithms for hadron hadron collisions.* Nucl. Phys. **B406**, 187–224 (1993).

[63] J. M. Butterworth, J. P. Couchman, B. E. Cox and B. M. Waugh. *KtJet: A C++ implementation of the K(T) clustering algorithm.* Comput. Phys. Commun. **153**, 85–96 (2003).

[64] Barlow R. *Statistics: A Guide to the Use of Statistical Methods in the Physical Sciences.* John Wiley and Sons Ltd 1989.

[65] M Boonekamp. *Luminosity Measurement in ATLAS.* Proceedings of the DIS2004 Conference, Štrbské Pleso, Sl~~ova~~kia (2004).

[66] S. Agostinelli et al. *GEANT4: A simulation toolkit.* Nucl. Instrum. Meth. **A506**, 250–303 (2003).

[67] K. Assamagan et al. *Final report of the ATLAS AOD/ESD Definition Task Force.* ATLAS-SOFT-2004-006 (2004).

[68] *LHC Computing Grid Technical Design Report* CERN-LHCC-2005-24.

[69] A. Delgrado Peris et al. *LCG-2 User Guide.* CERN-LCG-GDEIS-454439 (2005).

[70] A. M. Moraes, I. Dawson and C. M. Buttar. *Comparison of predictions for minimum bias event generators and consequences for ATLAS radiation background.* ATL-PHYS-2003-020.

[71] E. Albertson and J. Collot. *A Study of Pileup and Electronic Noise in the ATLAS Liquid Argon Presampler Detector.* ATL-LARG-95-023, 1995.

[72] R.A Davis and P. Savard. *A Study of Pileup Noise in the Barrel and EndCap Calorimetetry.* ATL-CAL-96-084, 1996.